University of Pisa

Master of Science in Aerospace Engineering

Space Curriculum

Mission Analysis and preliminary assessment of the Attitude Determination and Control Subsystem for the D3SAT mission

Harshraj Raiji

Academic year 2014-2015

CENTROSPAZIO

University of Pisa

Master of Science in Aerospace Engineering

Space Curriculum

Mission Analysis and preliminary assessment of the Attitude Determination and Control Subsystem for the D3SAT mission

Supervisors:

Prof. Ing. S. Marcuccio

Ing. S. Gregucci

Candidate:

Harshraj Raiji

Academic year 2014-2015

"It seems to me what is called for is an exquisite balance between two conflicting needs: the most skeptical scrutiny of all hypotheses that are served up to us and at the same time a great openness to new ideas...."

–Carl Sagan(*The Burden of Skepticism* ,1987)

"The joy of life comes from our encounters with new experiences, and hence there is no greater joy than to have an endlessly changing horizon, for each day to have a new and different sun."

–Christopher McCandless

Abstract

Recognizing the ever increasing importance of small satellites in the space sector, the need to qualify low power, low mass electric propulsion systems is crucial.SITAEL's HT-100D Hall Effect thruster is an ideal candidate owing to the low volume and low power requirements. The D3SAT (Drag make-up and Deorbiting Demonstration Satellite) technology demonstration mission aims to carry out comprehensive performance characterization of the low-power HT-100D thruster in-orbit, by mounting it on a microsatellite which has a mass less than 40 kilograms. This thesis deals with the analysis of orbital operations required for performance evaluation, namely drag compensation and end-of-life deorbiting. The requirements with respect to firing time and propellant mass are found for a range of mission profiles, keeping in mind the constraints imposed by the minimum guaranteed performance of the HT-100D, and some reference cases are analysed in detail. Since the orbit in which the D3SAT will be released in is dependent on the launch vehicle, the extra propellant required and the extra time added to the mission to perform an orbit lowering maneveur is also calculated, in the case that the D3SAT is released in a higher orbit (750 km). The HT-100D is found to efficiently satisfy the mission requirements with very low power requirements and low propellant consumption, thereby proving to be an ideal candidate to enhance the capabilities of small satellites.

In the second part of this thesis, the operating phases of the Attitude Determination and Control Subsystem (ADCS) based on the mission are described, and the requirements for each phase are derived. Preliminary design and specification of the ADCS to meet these requirements is then carried out. The attitude estimation hardware is selected based on these requirements using commercial-off-the-shelf components. The attitude control hardware is sized considering a worst-case disturbance environment. Interaction of the ADCS with other subsystems is analysed, and the contribution of the ADCS to the conceptual design of the D3SAT is specified, using commercial-off-the-shelf components. The ADCS is found to be compliant with the stringent volume and power requirements on-board small satellites.

Acknowledgments

I would like to express my sincere appreciation to my advisor and mentor Prof. Salvo Marcuccio for giving me the opportuntiy to do my thesis at Sitael. His constant guidance and valuable insight over the course of this thesis, have really helped to enhance my learning technique.

I am also deeply indebted to Stefan Gregucci for always being ready to assist, and for building my self-confidence in applying theoretical concepts to real-world problems.

This experience at Sitael has been a life-changing experience, and I would like to thank each and everyone I have interacted with here for their pleasant company.

Thank you to the beautiful country of Italy, for welcoming me and for teaching me invaluable lessons about life, and for giving me lifelong friends.

To the academic staff at the University of , for instilling in me the habit to approach every problem from first principles.

To all my colleagues with whom I have participated in this course of study, for giving me a chance to learn from them.

To all my friends from school and undergraduate study in Mumbai, for supporting me and making me the person I am today.

To my cousins, and each and every family member, for always encouraging me.

To Klara and the Šterk family, for giving me a home away from home.

To my sister Chef Devanshi, who has been a constant source of support.

To my mother Priti Raiji, for teaching me the value of being positive and feeling strong.

To my father Deval Raiji, for teaching me the value of hard work and for keeping his sense of humour when I had lost mine.

Contents

Contents ii

List of Figures v

List of Tables x

1 Introduction 1

1.1 Small Satellite SoA . . . 5
1.2 Thesis motivation . . . 7
1.3 D3SAT . . . 8
1.4 Work Structure . . . 9
1.5 SATSLab . . . 11

2 HT-100D characterization 12

2.1 HT-100D characterization . . . 12
2.1.1 Drag compensation . . . 12
2.1.2 EOL deorbiting . . . 13
2.2 Classical Orbital Elements . . . 15
2.3 Launcher and Orbital parameters . . . 16
2.4 HT-100D operating characteristics . . . 18

3 Attitude:Fundamentals 23

3.1 Reference frames . . . 23
3.2 Attitude representations . . . 25
3.2.1 Direction Cosine Matrix . . . 25
3.2.2 Euler angles . . . 26
3.2.3 Quaternions . . . 27

4 Mission Analysis **30**
4.1 Edelbaum's Method . . . 30
4.2 Drag Compensation . . . 32
4.2.1 Perturbations contributing to orbit decay . . . 32
4.2.2 Orbit decay . . . 36
4.2.2.1 Effect of atmospheric model on orbit decay . . . 37
4.2.3 Drag Compensation strategies . . . 40
4.2.4 Reference case 1:Altitude tolerance of 150 meters . . . 49
4.2.5 Reference case 2:Altitude tolerance of 450 meters . . . 51
4.3 Deorbiting . . . 52
4.3.1 Controlled vs Uncontrolled deorbiting . . . 53
4.3.2 Deorbiting strategy . . . 55
4.4 Starting altitude consideration . . . 59
4.5 Summary . . . 61

5 ADCS Modes and Requirements **63**
5.1 ADCS modes . . . 63
5.2 Requirements derivation . . . 64
5.2.1 Detumbling requirement . . . 64
5.2.2 IAA requirement . . . 64
5.2.3 Normal requirement . . . 65
5.2.4 HT-firing requirement . . . 72
5.2.4.1 Drag compensation . . . 72
5.2.4.2 Deorbiting . . . 72
5.2.5 Slew requirement . . . 72
5.3 Summary . . . 74

6 Attitude Estimation **75**
6.1 Common Attitude Sensors . . . 75
6.2 Sensor selection . . . 77
6.2.1 Magnetometer . . . 77
6.2.2 GPS . . . 82
6.2.3 Inertial Measurement Unit . . . 85
6.2.4 Sun Sensor . . . 87
6.3 Attitude Determination Algorithm . . . 92
6.4 Summary . . . 94

7 Attitude Control **96**
7.1 Torque Budget . . . 96
7.1.1 Aerodynamic Drag Torque . . . 96
7.1.2 Magnetic Field Torque . . . 100
7.1.3 Solar radiation pressure torque . . . 104
7.1.4 Gravity Gradient Torque . . . 107
7.2 Selection of ACS technique . . . 110
7.3 Selection of ACS hardware . . . 112
7.4 ACS hardware sizing . . . 115
7.4.1 Reaction wheel sizing . . . 115
7.4.2 Magnetorquer sizing . . . 123
7.5 Summary . . . 125

8 Attitude Kinematics and introduction to control theory **127**
8.1 Effect of external disturbance torques on attitude motion . . . 127
8.2 Control theory . . . 133
8.2.1 Modified Euler equations . . . 133
8.2.2 Attitude error . . . 134
8.3 Momentum dumping . . . 135

9 Mode details **137**
9.1 Detumbling . . . 137
9.2 Initial Attitude Acquisition . . . 141
9.3 Normal . . . 143
9.4 HT-firing . . . 143
9.5 Slew . . . 145
9.6 Mode transition scheme . . . 147

10 Conclusions and Future Work **150**

Bibliography **154**

List of Figures

1 Small satellite classification 2
2 Microsatellite applications(Source:[1]) 4
3 Nano/Microsatellite Launch Projection(Source:[1]) 5
4 D3SAT subsystems inter-relation 9
5 Work structure 10
6 Space debris classification (Source:[2]) 13
7 Deorbiting complexity 14
8 Classical Orbital Elements 15
9 Study of orbital parameters of microsatellites(Source:[3]) 16
10 Launch vehicles for microsatellites(Source:[4]) 17
11 Working principle of Hall Effect Thruster 18
12 HT-100D 19
13 HT-100D performance (Source:[5]) 20
14 HT-100D operating temperature(Source:[6]) 22
15 ECI Frame 24
16 RTN Frame 24
17 BF Frame 25
18 Yaw,Pitch and Roll axes of the D3SAT 26
19 Euler's theorem 27
20 Definition of D3SAT faces 29

21 Effect of J2 on orbit decay 34
22 Orbit decay during solar minimum activity 39
23 Orbit decay during solar mean activity 39
24 Orbit decay during solar maximum activity 40
25 Drag compensation strategies:daily profile 41
26 Daily thrust and SMA profile for altitude tolerance of 10 m 42
27 Daily thrust and SMA profile for altitude tolerance of 50 m 43
28 Daily thrust and SMA profile for altitude tolerance of 150 m 44
29 Daily thrust and SMA profile for altitude tolerance of 250 m 45
30 Daily thrust and SMA profile for altitude tolerance of 350 m 46
31 Daily thrust and SMA profile for altitude tolerance of 450 m 47
32 Number of ignitions required for various drag compensation strategies 48
33 Reference case 1:1 month propellant consumption 49
34 Reference case 1: 6 months propellant consumption 50
35 Reference case 2: 1 month propellant consumption 51
36 Reference case 1: 2 months propellant consumption 52
37 Satellite lifetime 53
38 Demise altitude of D3SAT materials(Source:[7]) 55
39 Deorbiting strategies 57
40 End-of life deorbiting profile 58
41 Passive decay orbit after uncontrolled deorbiting 59
42 High starting altitude consideration 60
43 Orbit lowering from high starting altitude of 750 km to 350 km . . . 61
44 Gaussian VOPs expressed in non-singular elements 66
45 Effect of thrust vector misalignment 68
46 Thrust beam misalignment results:$\theta, \psi = 0 \pm 180°$ 70
47 Thrust beam misalignment results:$\theta, \psi = \pm 5°$ 70

48 Variation of semi-major axis over firing period due to thrust beam misalignment . . . 71
49 Ground Station visibility arc . . . 73
50 Earth magnetic field description . . . 78
51 IGRF model:12th generation(Source:[8]) . . . 81
52 Magnetometer,SSTL specifications . . . 82
53 GPS Space Segment . . . 83
54 GPS receiver operating principle . . . 83
55 SGR-05P Space GPS receiver,SSTL specifications . . . 85
56 STIM300,Sensonor specifications . . . 86
57 3DM-GX1,LORD MicroStrain specifications . . . 87
58 Flat sun sensor . . . 89
59 Single axis pyramidal sun sensor . . . 90
60 Bi-axis pyramidal sun sensor . . . 90
61 Sun sensor placement . . . 91
62 BASS 17,EADS Astrium specifications . . . 92
63 Kalmann filter schematic . . . 93
64 Attitude Estimation Subsystem schematic . . . 95
65 Definition of incidence angle α_i . . . 97
66 Effect of shape of the D3SAT on τ_a . . . 98
67 Worst-case drag impacted area . . . 99
68 Choice of C_D(Source:[9]) . . . 100
69 Earth magnetic field lines . . . 102
70 Variation of Earth magnetic field from 2016-2020 . . . 103
71 Sunlit area A_S . . . 105
72 τ_S variation with incidence angle φ . . . 106
73 Effect of sunlit area $A_S$on τ_S . . . 107
74 Proposed solar array configuration during drag compensation . . . 107

75 Definition of θ for τ_{gg} . . . 108
76 Effect of θ deviation on τ_{gg} . . . 108
77 Disturbance torques as a function of altitude . . . 109
78 Torque/power vs. momentum comparison of CMG's and RW's([10]) 113
79 Mass and volume comparison of CMG's and RW's(Source:[10]) . . 114
80 Magnetorquer working principle . . . 115
81 Required torque level of reaction wheels with altitude . . . 116
82 Atmospheric drag torque profile . . . 118
83 Magnetic field torque profile . . . 119
84 Gravity gradient torque profile . . . 121
85 Reaction wheel requirements with altitude . . . 122
86 RW 35 ,AFAG specifications . . . 123
87 Required magnetorquer dipole vs altitude . . . 123
88 Magnetorquer mass-power characteristics from ZARM Technik . . 124
89 MT1-1, ZARM Technik specifications . . . 124
90 Attitude Control Subsystem schematic . . . 126

91 Effect of τ_{ext} on angular acceleration . . . 129
92 Effect of τ_{ext}on angular rate . . . 130
93 Effect of τ_{ext} on Euler angles . . . 131
94 Effect of τ_{ext}on quaternions . . . 132

95 Detumbling time as a function of dipole moment . . . 140
96 MT5-2 ,ZARM Technik specifications . . . 141
97 Detumbling using bang-bang control . . . 141
98 BASS 17,EADS Astrium . . . 142
99 IAA algorithm . . . 142
100 IAA algorithm diagram . . . 143
101 Yaw maneuver time for deorbiting . . . 144

102 Pointing rate as a function of altitude 146
103 Transmitted data limit based on angular momentum capacity of RW's 146
104 Mode transition scheme 148
105 Daily mode transition scheme for drag compensation 149

List of Tables

1 Small satellite classification: 2

2 DNEPR performance (source:[11]) 17

3 HT-100D operating range 21

4 HT-100D:chosen operating point 21

5 HT-100D constraint based requirements 22

6 Perturbations recommended treatment 36

7 Effect of atmospheric model on orbit decay 38

8 Drag compensation strategies 41

9 Drag compensation:reference case 1 49

10 Requirements for reference case 1 50

11 Drag compensation:reference case 2 51

12 Requirements for reference case 2 52

13 D3SAT material thermal properties 54

14 Mission analysis summary 62

15 Thrust beam misalignment results:$\theta, \psi = 0 \pm 180°$ 69

16 Thrust beam misalignment results:$\theta, \psi = \pm 5°$ 70

17 ADCS requirements 74

18 Comparision of optical sensors 88

19 Attitude Estimation Subsystem budget 94

20 Residual dipole moment 101
21 Variation of solar constant Φ 104
22 Torque budget 109
23 Attitude Control Subsystem budget 125
24 Final ADCS mass and power budget 152

Chapter 1

Introduction

The Space Age started when the Sputnik launched in October 1957 .Since then, satellites rapidly grew increasingly large and expensive.This was due to the fact that in order to be a part of the "space race", the super-powers of the world strove to out-do each other and gain access to space, irrespective of budget.This led to escalated costs and lengthened timescales,with satellites taking years to reach useful orbital operation from the concept phase.These factors limited access to space to all but a few nations or international agencies.As the years have progressed, budgetary restrictions have increased the pressure on space agencies to produce cheaper and smaller satellites. These budgetary restrictions , combined with rapid development of miniaturization technologies have enabled a new breed of small satellites which are smaller and cheaper, have shorter lead times and can perform the same functions as their their large counterparts. At the beginning of small satellite development, it was believed that the smaller the size , the smaller the functionality. However, advances in both miniaturization and integration technologies have diminished the scope of that trade-off. It is important to first understand what exactly is meant by "small" when we talk about satellites. Generally, satellites weighting below 1000 kg or up to 500 kg are considered as small satellites[1]. This trend towards smaller satellites has been happening over time, with much of the innovation taking place in developing countries and University environments, where affordability has been the key driver. While some small satellites are integrated and designed with the same rigor as their large counterparts, other small satellites can be completely designed and built in a laboratory environment. This has enabled universities all over the world to be active in the design and development of small satellites, which have a history of

bottom-up development. Initially, most missions of student small satellite missions were quite elementary, such as taking a picture using a basic mobile phone camera and deploying a panel using a motor. However, as time has progressed, the performance of small satellites has steadily improved, with more and more satellites being capable of conducting difficult missions for a practical use. Small satellites have evolved into a new practical business tool that non-commercial and private enterprises can afford. Within the mass range for small satellites, referring to [12, 1], the following classification has become widely adopted:

Class	Weight
'Standard'	>1000 kg
Mini	100-1000 kg
Micro	10-100 kg
Nano	1-10 kg
Pico	100 g-1 kg
Femto	<100 g

Table 1: Small satellite classification:

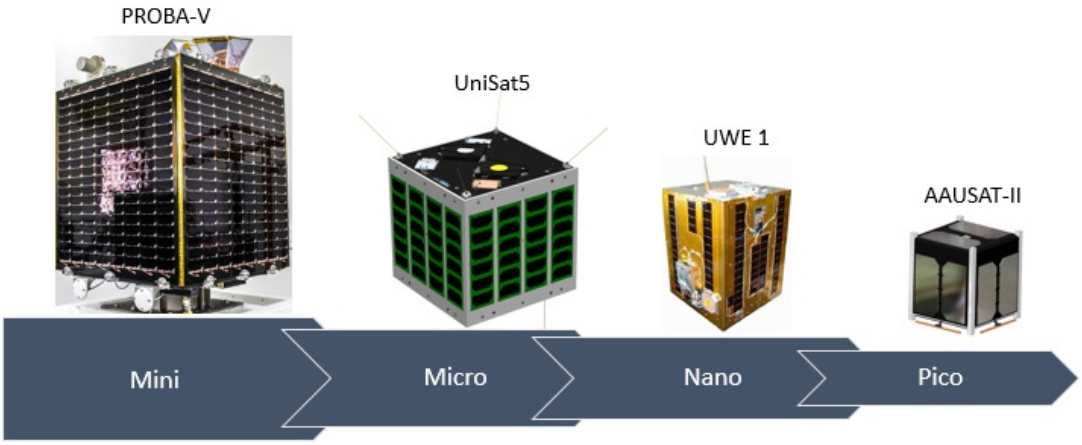

Figure 1: Small satellite classification

Applications of microsatellites:

1)Earth observation

Small satellites are usually placed in low altitude orbits, thus enabling higher resolution missions. Small satellite images can be used in a wide range of fields including agriculture, forestry, fishery, resource exploration, map-making, security, and so on. In addition, a constellation of low-cost micro-satellites in orbit can enable to achieve frequent earth monitoring, which is difficult to realize only with a single large satellite.

2)Specialized communication and research

Satellite communication has been in use for decades. There are two types of satellite communication, one is to use geosynchronous orbit satellites which needs a large antenna due to to the high altitude of the satellites. The other is to use low-earth orbit (LEO) satellites, in which smaller antennas are enough to communicate, and mobile telecommunication is one of the important applications. Such smaller satellites also hold out the promise of less expensive ground terminals and regional frequency reuse. Due to the low cost and small lead time, microsatellites can also be used to study communication problems such as varying communication paths and links, high Doppler shifts and hand-over from satellite to satellite[13].

3)Space Science

Space is a special place where the environment is completely different from that on the ground. Satellites are orbiting several hundred kilometers away from the ground, and air density there is nearly zero. Exploiting this advantage, satellites have observed many targets including the sun, the earth's atmosphere, celestial bodies out of the solar system. There are also space probes having explored the moon, planets, and asteroids. They have greatly contributed to our current knowledge of the earth, the solar system, and the whole universe. Now we can find many micro-satellites in orbit with science missions in various fields where researchers can achieve study results at low cost and in a short period of time. Students can research, propose and build instruments to retrieve orbital data for analysis and in the process, make new discoveries in a much smaller time, owing to fast production time of microsatellites.

4)In-orbit technology verification

Perhaps the predominant application of small satellites is for educational projects and scientific experimentation. Microsatellites offer a low cost-mean of demon-

strating, verifying and evaluating new technologies rapidly, thus allowing innovative devices or methods to be tested prior to commitment to a full-scale mission. This is especially useful for university students, who can completely design a mission within the short period of graduate study. This is precisely why a microsatellite is used in this thesis, as will be explained later.

4)Education and training.

As space utilization expands, developing countries and universities are becoming increasingly capable to develop low-cost microsatellite missions. University students can get hands-on experience during the relatively short-period of their course of study and collaborations can be made to share satellite resources and to share small satellite research ideas and developments.

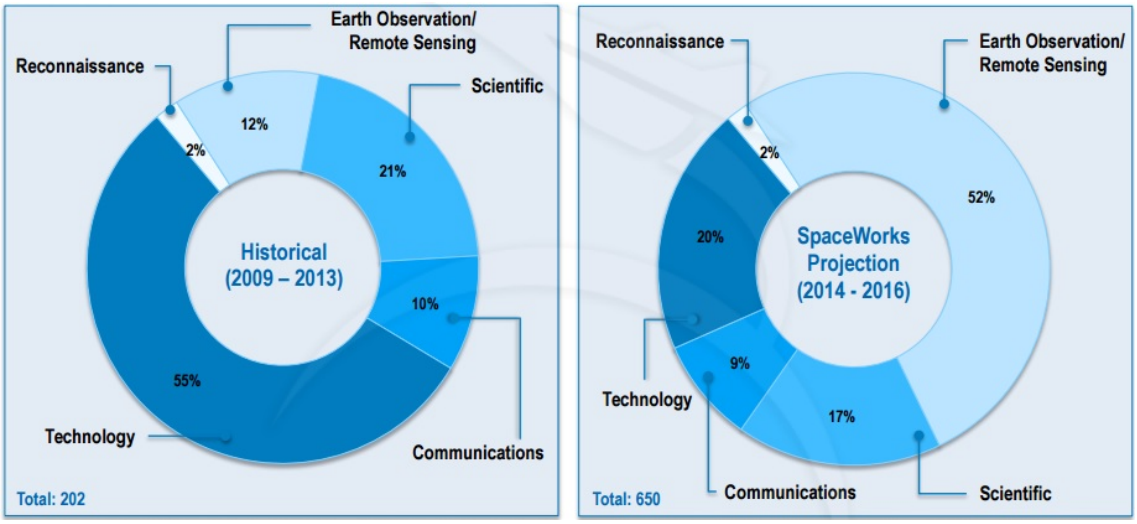

Figure 2: Microsatellite applications(Source:[1])

Hence, due to the wide range of applications for microsatellites, we can recognize their ever increasing importance in the space sector. Also, as we can see in the figure below, there are projected to be about 2,000-2,750 small satellites in the range of 1 kg-50 kg requiring launch from the year 2014 to 2020. This shows the increasing importance of small satellites, and this further justifies the use of a microsatellite for the D3SAT mission.

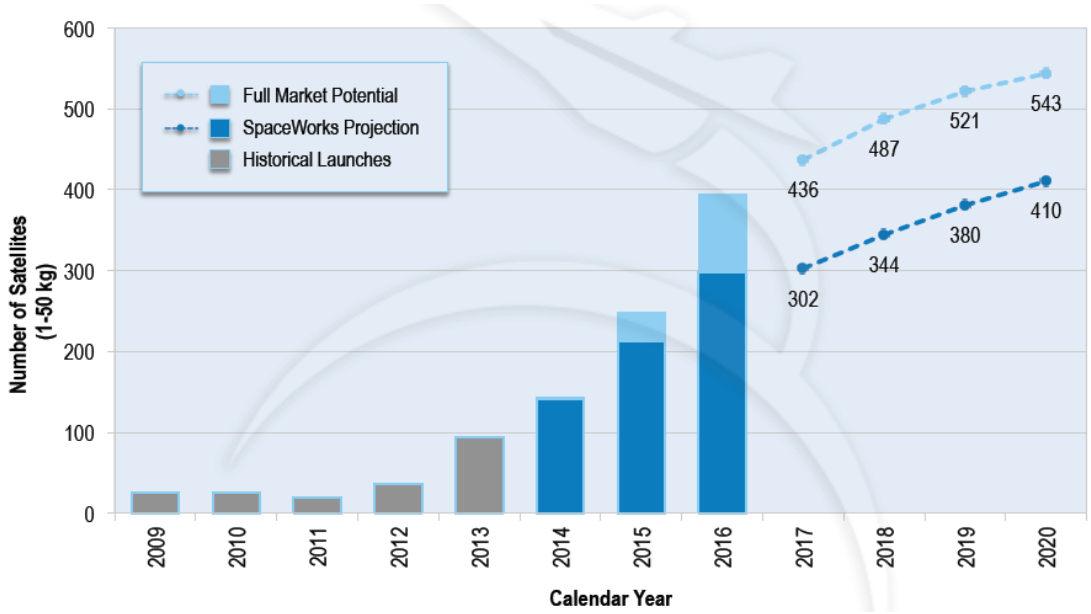

Figure 3: Nano/Microsatellite Launch Projection(Source:[1])

Hence, due to the numerous applications of microsatellites, and due to their rapidly increasing yearly production, we recognize the ever increasing importance of small satellites in the space sector.

1.1 Small Satellite SoA

Power

Nowadays, more efficient power generation, storage and distribution hardware and software are available within the commercial space market. Thus, generally speaking, recent microsatellites are more capable compared to their predecessors.The available power level of most microsatellite missions in the past has been as low as 50-70 watts or less. However, as indicated in[14], these power levels are being enhanced by a factor of 2-3. These increasing power levels are supported by advances in power generation and storage technology, with highly efficient triple-junction lightweight solar cells and high specific energy lithium ion batteries being developed. Power generation and storage subsystems for microsatellites have progressed based on stringent mass and volume requirements. Power distribution systems are reliable and robust and flexible solar cells are under development, allowing new concepts for solar panel deployment. Another technology on the horizon is the CubeSat-scale Radioisotope Thermal Generator (RTG)[12].

Propulsion

Historically, microsatellites have not been equipped with propulsion systems. Although there have been experiences of carrying propulsion systems on-board

microsatellites, these have been mainly for technology demonstration missions. Small spacecraft propulsion is an immature technology domain, and that is why it has become important to advance this field by qualifying low cost, low mass and high performance propulsion systems. The state of art in this field consists of cold gas thrusters (Isp=70 sec) and pulsed plasma thrusters (Isp =830 sec). Green mono-propellant systems (Isp = 300 sec) are on track to be demonstrated[12].

Attitude Determination and Control

The state of art of Attitude Determination & Control (ADCS) for small spacecraft relies on miniaturizing technology without significant performance degradation. Miniaturization's are achieved with advanced technologies such as new imaging devices, materials, peripheral circuits, and algorithms. Overall attitude pointing accuracy of typical mini and microsatellite Earth observation missions is better than 1° now, as opposed to $\leq 10^\circ$in the past[12, 14]. Systematically decreasing the development cost of ADCS software will contribute to the low cost and rapid development benefits of using small spacecraft.

Structure

In-house built structures are becoming rarer as time progresses,owing to increased cost and increased overall lead time. Most small satellite developers look to buy the structures off-the-shelf.This demand is met by many commercial companies such as Pumpkin, ISIS and SSTL ,which fabricate structures for a large variety of small satellite missions. Most structures built in-house pertain to mini or microsatellites. Due to their reliability and strength, aluminum alloys (with an average density of $2.8 g/cm^3$) are the materials most used for small satellite structures[12]. Composites have been used more frequently in the last few years, but their high cost is still a disadvantage.

Thermal control

Generally speaking, passive or semi-active thermal control methods have been seen to be more than adequate for microsatellites. Active thermal methods have not been able to be efficiently miniaturized[12].

Command and Data Handling

Today, Command and Data Handling (CDH) systems have greater processing capability with lower mass, power and volume requirements owing to better understanding of space environment and maturation of software programs[14]. This general trend is enabling small spacecrafts to tackle a broader range of missions.

Communications

Current satellite communication transmission strategies use VHF, UHF, microwave, and infrared/visible frequency spectra. Selecting a frequency spectrum depends on a number of factors including expected data throughput, available power and mass, and licensing issues. Due to these reasons, technology development is still underway on all of these frequency spectra. However , in general, due to increasing power capabilities, the data rates are expected to rise to up to 10 Mbit/sec from 1 Mbit/sec in the past.[14]

1.2 Thesis motivation

The capabilities of small satellites have been limited, because propulsion systems have proved difficult to shrink. Conventional thrusters tend to lose efficiency and power at small sizes, and they can double the size of a small satellite, making it too expensive to launch into space[15]. The most common and convenient way to design subsystems for the small size of microsatellites is direct scaling of components successfully used in larger platforms. However, when it comes to traditional propulsion systems, they do not scale linearly. Considering a traditional chemical mono-propellant thruster, if the propulsive performance is to be maintained (same specific impulse) then the adiabatic flame temperature should remain constant, which at lower sizes means higher heat fluxes and the need of better structures to disspipate the heat. Therefore as we can see, attempts to scale propulsion systems acts in a direction opposite to that of scaling. In addition to this limitation, chemical thrusters require a number of auxillary components that are difficult to miniaturize, including high pressure valves, reservoir tanks and catalytic chambers. Finally, the Isp of such systems is limited to about 200-250 sec[16], meaning that high Δv maneuvers require a very high propellant mass fraction with respect to the initial spacecraft mass, as is evident from Tsiolkovsky's equation:

$$\frac{m_p}{m_0} = 1 - e^{-\Delta v / g_0 I sp}$$

For chemical rockets, this represents about 20 % for $\Delta v = 500 m/s$. Electric propulsion offers very high specific impulse, thus reducing propellant mass and enabling higher small satellite payload. Chemical engines can eject massive amounts of propellant, whereas electric thrusters work with very small flows, so the low thrust levels mean higher time to complete the required maneuver. When high acceleration is critical ,electrical propulsion cannot be used, at least in its current

forms. However, it is becoming increasingly important, when it comes to small satellites, to increase the payload capability and allow significant extensions of the satellite lifetimes.

Electric propulsion for spacecraft provides thrust by emitting electrically-charged particles extremely high speeds. Such thrusters do not burn fuel, they eject it. The propellant is ejected up to twenty times faster than from classical thrusters and therefore the same propelling force is obtained with twenty times less propellant. However, the real challenge is to cope with the limited power availability on-board small satellites.Therefore, the need arises to test and qualify low power,low cost electric propulsion systems which can easily be installed on small satellite platforms and which can readily respond to the demands of both commercial and non-commercial organizations. Designing and testing electric thrusters with fair performance and lifetime is the key to open a new market niche for electric propulsion and enter the sector of small satellites which could, in turn, get a tremendous benefit from the mass savings offered by electric thrusters.

The HT-100D low power thruster produced by Sitael is an ideal candidate to be flight qualified, owing to low power consumption and low mass. The structure of the HT-100D assembly (which consists of Power Processing Unit,feed-lines and a suitable propellant tank) architecture is partly modular, which ensures flexibility, thus enabling a degree of adaptability to varying mission requirements. An in-orbit demonstration of this thruster can open the doors to new classes of missions which are feasible only by means of electric propulsion, and enhance the capabilities of small satellites. Therefore it becomes important to carry out a technology demonstration mission.

"The objective of this thesis is to develop a technology demonstration mission to carry out comprehensive performance characterization of the HT-100D in-orbit and to compare the in-flight performance measurements with the measurements acquired in the laboratory environment ."

1.3 D3SAT

The D3SAT (Drag make-up and Deorbiting Demonstration Satellite) has been designed keeping in mind that the overall launch mass must not exceed 40 kg. The dimensions should be $40 \times 40 \times 40\, cm^3$. These weight and dimension restrictions are self-imposed keeping in mind the typical dimensions of a microsatellite and the weight restrictions demanded by the launch vehicle (refer to section 2.3).

The subsystems of the D3SAT are shown in the figure below , in the block 'conceptual design'. This design will be specified based on requirements from the main mission , and the restrictions imposed by the launch vehicle, as discussed in the following chapter.

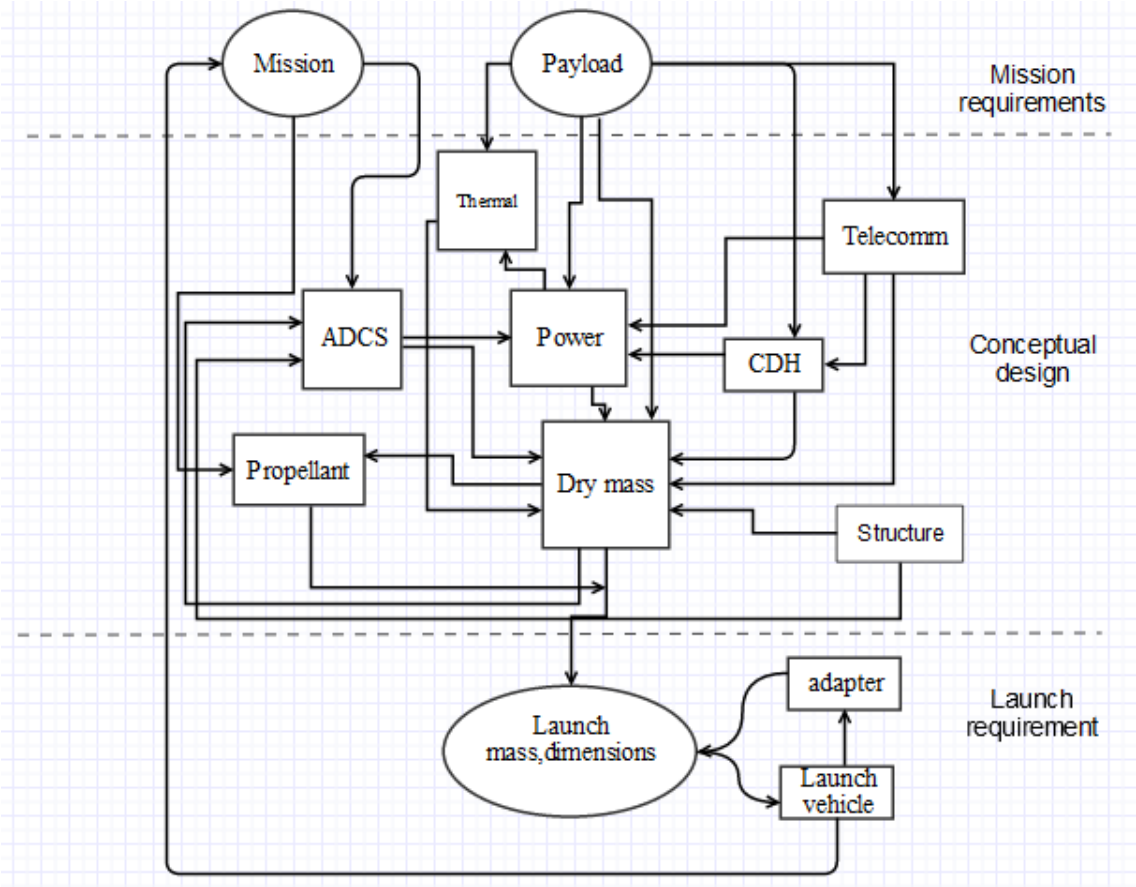

Figure 4: D3SAT subsystems inter-relation

1.4 Work Structure

This contribution of this thesis will be the analysis of the mission required to evaluate the performance of the HT-100D in-orbit, after which the preliminary design and specification of the Attitude Determination and Control Subsystem (ADCS) is carried out. This will contribute to the conceptual design of the D3SAT. The work structure is shown in the figure below.

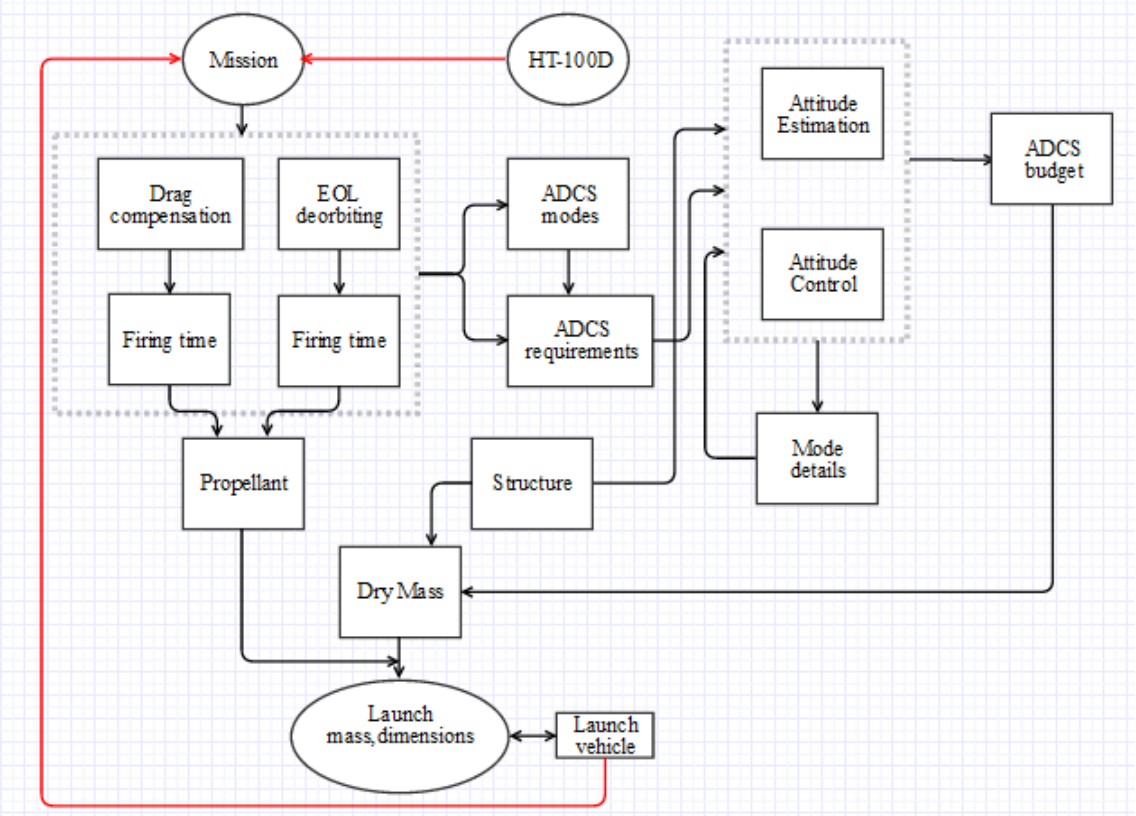

Figure 5: Work structure

In chapter 2, the constraints imposed by the HT-100D and the launch vehicle on the main mission will be discussed. The main mission itself will be based on what maneuvers are necessary and important to characterize the the performance of the HT-100D.

In chapter 3, the main mission will be decided and analyzed based on the constraints obtained in chapter 2. Various mission profiles are presented and some reference cases are studied.

An introduction to attitude , and attitude representation is presented in chapter 4, along with the reference frames that are used in this thesis.

In chapter 5, the functioning of the ADCS is divided into operating phases, or modes, and the requirements for each of these modes based on the main mission are derived. These requirements will be the basis for the conceptual design of the ADCS.

Chapter 6 deals in whole with attitude estimation techniques, and comparisons are made between different types of attitude sensors, and the best options are selected from the market.

In chapter 7, the various techniques of attitude control are discussed, and the technique most suitable to the D3SAT mission is selected. Sizing and selection of the attitude control hardware is carried out, based on the mission requirements and on the external disturbances which warrant the need for attitude control.

Chapter 8 deals with understanding how the external disturbance environment has on attitude motion. Also, a brief introduction to control systems is given, which explains how to introduce attitude control using the attitude control hardware.

In chapter 9, each mode of the ADCS is analyzed to evaluate the performance of the selected ADCS hardware, and interaction with other subsystems is studied. Previous choices of ADCS hardware are revisited, and reiterations are made if necessary.

1.5 SATSLab

Computation of low-thrust trajectories is a difficult task due complications arising from Earth-shadow eclipse and high input power to the thruster. The low-thrust maneuvers investigated in this paper are computed by the software suite SATSLab (Spacecraft Attitude, Trajectory and Subsystems Laboratory), a low-thrust space mission simulator developed as a collaboration between Alta (now SITAEL) and the University of Pisa[17]. SATSLab is a fundamental tool for mission analysis and spacecraft subsystem sizing for missions where the usage of electric propulsion systems is envisaged. SATSLab allows for an accurate assessment of orbital trajectory and spacecraft subsystems energy status, fundamental aspects to take into account in the design of missions with small satellites and limited on-board resources. SATSLab simulator computational modules are written in MATLAB and the Graphical User Interface (GUI) in Java , so the simulator is completely platform-independent, providing the same functionality and user experience regardless of the operating system of the computer platform[18].

Chapter 2

HT-100D characterization

In this chapter, the operations for which the HT-100D can be proved useful are explored. These operations will make up the technology demonstration mission. Then, before proceeding to analyze the mission based on these shortlisted operations, certain constraints which dictate the main mission are taken into consideration.

2.1 HT-100D characterization

For the characterization of the HT-100D, the operations executed by it must be important for typical operations of small satellites which have low mass and low volume. Keeping this in mind, maneuvers considered important are drag compensation and de-orbiting [19].The justification of why these two orbital operations are important are discussed below.

2.1.1 Drag compensation

The capability of electric propulsion for providing continuous thrust over a long period , together with the reduced propellant mass consumption, allows for accurate LEO station-keeping operations over sufficiently long duration missions.LEO missions provide a unique means of gathering information about many of Earth's aspects such as climate, atmosphere, and gravitational field. In LEO, it becomes very challenging to design, predict and maintain the orbit of a spacecraft, due to the perturbative forces acting on it, which are mainly atmospheric drag and J2 and higher order gravitational components. While the effect J2 and higher order gravitational components are easy to predict, the drag is another issue. The continuously varying atmospheric drag requires increased spacecraft tracking in

order to accurately predict spacecraft location. Continuously and autonomously counteracting the effects of drag would eliminate the uncertainty of LEO spacecraft orbit prediction. Thus it becomes important to evaluate the performance of the HT-100D for drag compensation. A secondary advantage of orbit maintenance is that the time history of the positions of the satellite is known in advance, therefore the intended position of each satellite at all future times is known. Consequently, we know in advance when they will pass over any given ground station, target, or communications location. The basic geometric conditions such as Sun angle, ground station angle, or inter-satellite angles(in case of a satellite constellation) are all fully known in advance, such that activities can be planned at the convenience of the ground station. This also makes the job of spacecraft requirement specification much easier.

2.1.2 EOL deorbiting

In more than half a century of space activities more than 4800 launches have placed some 5000 satellites into orbit, of which only a minor fraction are still operational today. Besides this large amount of intact space hardware, with a total mass of about 6000 tonnes, several additional objects are known to orbit the Earth. Only 6% of the cataloged orbit population are operational spacecraft, while 28% can be attributed to decommissioned satellites, spent upper stages, and mission related objects[2].

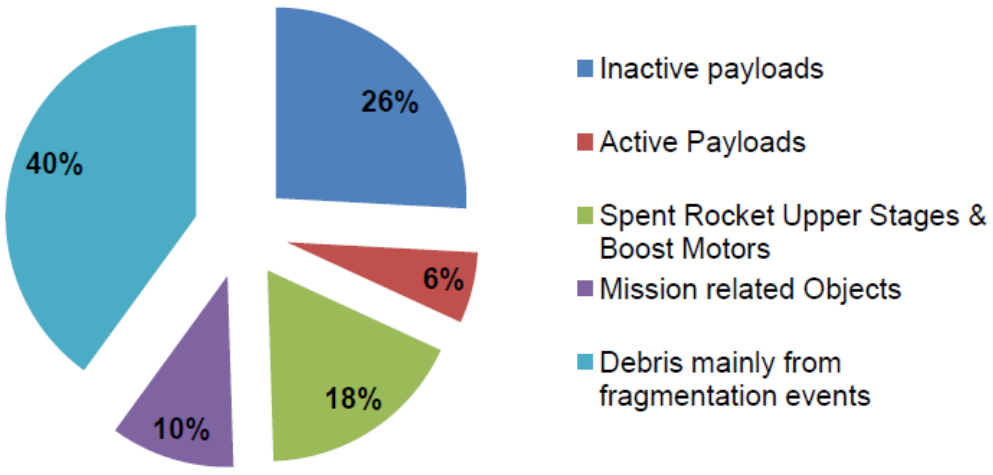

Figure 6: Space debris classification (Source:[2])

We can see from the figure above that defunct payloads make up most of the debris population. If not removed from orbit after operation, these inactive payloads could break up into smaller fragments due to collisions, therefore leading the space debris environment into a chain reaction and rendering some orbital regions with an unacceptable risk for operations

To capture and de-orbit a large piece of defunct space hardware is no small challenge, both technically, legally and financially. Therefore it becomes important that the means of deorbiting a defunct satellite does not rely on specific interfaces on the target satellite. Even before capturing the target, it needs to be tracked from the ground, and a rendezvous and target characterization phase needs to be carried out. This requires complex propulsion systems and complicated guidance and navigation techniques and expensive sensors, which are not usually capable of being handled by small LEO satellites. This can be very difficult and complex,not to mention costly, as seen in the figure below, taken from[20]:

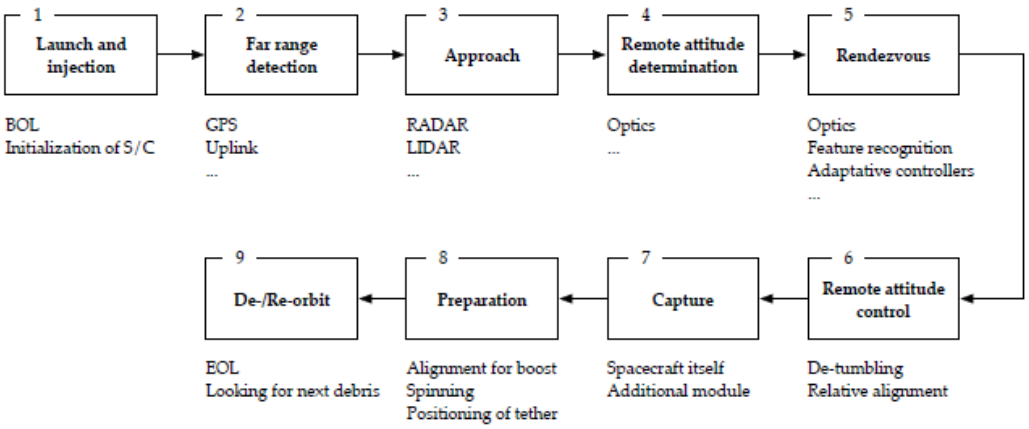

Figure 7: Deorbiting complexity

Another way is to install deorbiting mechanisms on-board for activation at the EOL. Examples include drag parachutes,inflatable balloons and solidifying foams. The above methods will add to increase mass and cost to a satellite. For a big satellite these options can be considered, however, for microsatellites we want to reduce complexity and avoid addition of mass to the platform.Keeping this in mind, we recognize that the most efficient method of end-of-life disposal is to use the thrusters which are already available on-board. This will involve adding extra propellant to perform a deorbit burn at the end of the useful mission. Inactive payloads and spent rocket stages, that already amount to 44% of LEO cataloged objects population, are the two categories of objects whose abandonment in space

can be avoided in future missions, once deorbit systems are finally implemented on-board new LEO satellites before launching them[21]. Therefore, it becomes important to evaluate the performance of the HT-100D for end-of-life deorbiting. In addition, the D3SAT will already have the HT-100D for drag compensation, and therefore the most effective method of disposal is adding enough propellant to perform a deorbit burn at the end of the useful mission.

2.2 Classical Orbital Elements

Before understanding the effect of constraints imposed by the launch vehicle on the main mission, it is important to recall the classical orbital parameters which completely describe the shape and orientation of an orbit.

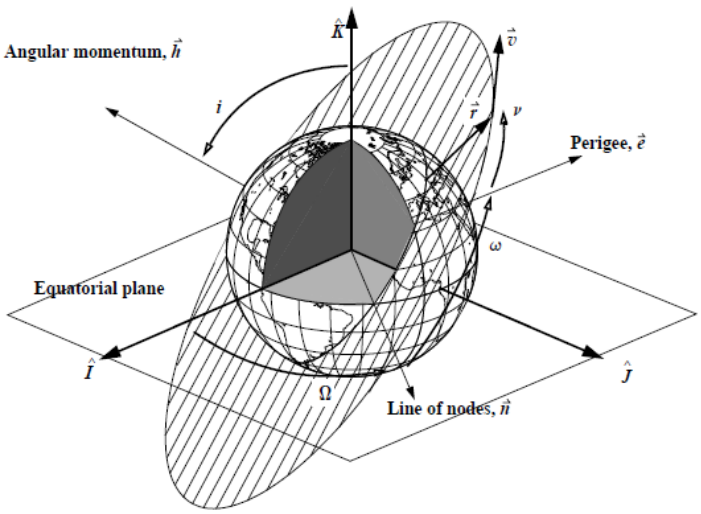

Figure 8: Classical Orbital Elements

The classical orbital elements as shown above are[22]:

1)semi-major axis a

2)eccentricity e

3)inclination i

4)right ascension of ascending node Ω

5)argument of perigee ω

6)true anomaly ν

2.3 Launcher and Orbital parameters

Information about the orbit we are expecting is detrimental to analyzing the mission and analyzing platform sizing, power requirements and ADCS requirements. Dedicated launch options currently do not exist for satellites up to 50 kg. Instead, satellite payloads in this mass range are manifested as secondary or piggyback payloads to the large primary payload. Sometimes, a cluster of microsatellites and/or nanosatellites are multi-manifested as piggyback payloads to be launched together. Depending on the choice of our launcher and the launcher's launch schedule, our microsatellite will be a piggyback payload to the primary payload or will be a part of a cluster of payloads. Since microsatellites ride as secondary payloads, they are generally not able to select their orbit and hence the orbital destination will depend on the main launch vehicle.

For microsatellites up to 50 kg, a study done in [3] shows the popular orbital parameters, namely apogee and inclination.

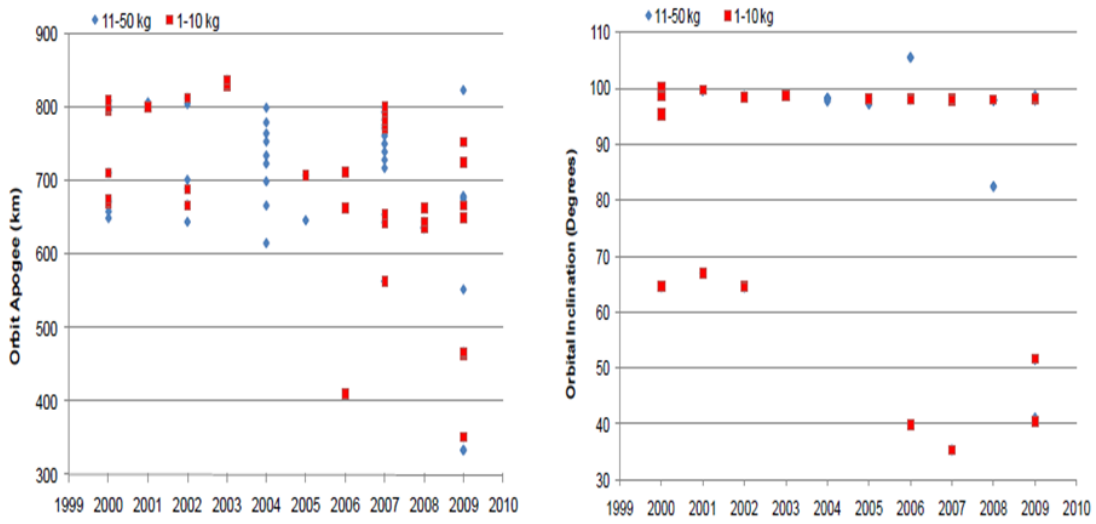

Figure 9: Study of orbital parameters of microsatellites(Source:[3])

Nano and microsatellites (less than 50kg) predominantly launch to polar or sun-synchronous orbit, but recently have also launched to lower altitudes and inclinations.From the above figure we see average orbital apogee is 750 km and average inclination is 90°.

Historically the Ukrainian Dnepr-1 and Indian PSLV have been the most popular launch vehicles for satellites up to 50 kg. The popularity of these vehicles is primarily due to their acceptance of small piggyback payloads and their relatively inexpensive price. We see in the figure below launch vehicles used for the 11-50 kg satellite class from 2000-2012 as percentage of global satellites launched.

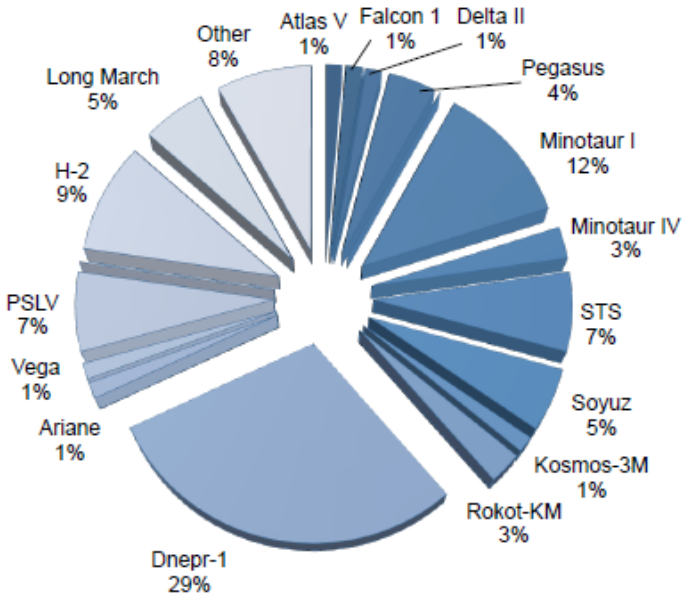

Figure 10: Launch vehicles for microsatellites(Source:[4])

The most economical launch vehicle is found to Ukraine's Dnepr-1[23], and in addition, it has a very high level of success. It is ideal for launching a cluster of microsatellites. In fact, the most recent Dnepr-ASNARO mission,in November 2014, launched the 500 kg satellite ASNARO along with four piggyback microsatellites Hodoyoshi-1(60 kg), ChubuSat-1 (50 kg). TSUBAME (49kg) and Qsat-EOS (49 kg)[24]. Our microsatellite will be an ideal candidate to be part of such a cluster launch, and our confidence in the choice of the Dnepr Launch Vehicle is only strengthened by previous microsatellite missions. Referring to[11], we see that the available orbital inclinations are $50.5°, 64.5°, 87.3°, 98°$. Also we see the performance of the Dnepr launch vehicle for spacecraft injection accuracy in the figure below:

Orbital Parameter	Typical circular orbits		
	H=300 km, i=98°	H=600 km, i=98°	H=900 km, i=65°
Altitude, km	±4.0	±5.5	±10.0
Period of revolution, sec.	±3.0	±4.0	±6.5
Inclination, deg.	±0.040	±0.045	±0.050
Right ascension of the ascending node, deg.	±0.050	±0.060	±0.070

Table 2: DNEPR performance (source:[11])

Although the uncertainty of the launch vehicle to be used, and therefore the final orbit parameters of the microsatellite, are high, we can select an inclination of 98°and an altitude of 350 km as a reference case, in order to analyze the mission. As we will see in this thesis, this altitude will impose the most stringent requirements on the ADCS and therefore we will be designing the ADCS based on the

worst case. For the design and specification of the ADCS, the most extreme requirements will be at the low altitude of 350 km. Therefore we can be assured that this subsystem will perform sufficiently well for other cases, thus confirming adaptability of the ADCS to different orbital parameters.In addition, if the D3SAT is released at the extreme case of 750 km, the extra time added to the mission as well as extra propellant required is calculated.

2.4 HT-100D operating characteristics

This thesis is carried out in collaboration with SITAEL(formerly Alta). The HT-100 is a small, low-power Hall Effect Thruster (HET) designed to perform orbit control tasks on micro-spacecraft and attitude control tasks on mini-satellites. It is the smallest and lowest power HET developed in Europe, whose performance and characteristics represent the state-of-the-art of this technology. The HT-100 thruster unit is fully based on Italian know-how and technology, as are all of the key sub-system components. In Hall Effect Thrusters, the propellant gas, usually xenon, is ionized and then accelerated electrostatically. Electrons emitted from the cathode are trapped in a region of strong magnetic field, causing the electric potential to drop locally. This axial electric field associated with this potential drop accelerates the ions towards the thruster exhaust section[25]. Specific impulses up to 3000 s can be obtained, together with efficiency over 60% and thrust levels ranging from mN (mini-Hall) to a few N (High Power HETs).

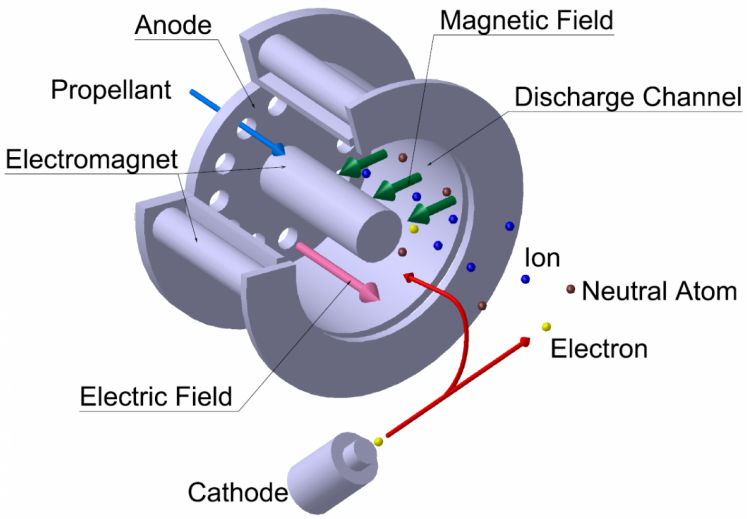

Figure 11: Working principle of Hall Effect Thruster

The most relevant design feature of the HT-100 is the use of permanent magnets instead of electromagnets for the generation of the required magnetic field[26]. The latest version of the thruster, (HT-100D) has a larger chamber diameter with respect to the original one and it is capable of attaining thrust levels up to 20 mN. In spite of the slight widening of the discharge channel, the new version of the thruster is extremely lightweight, the mass being merely 436 grams (excluding the cathode).

Figure 12: HT-100D

A mini endurance test of 200 hours has been also carried out in order to study the erosion effects and in 2013,the HT-100D has been coupled with a new cathode developed by ALTA(now SITAEL)-ALPHcA, Alta Low-Power Hollow Cathode[6]. This cathode can sustain the main discharge with a mass flow rate of 0.1-0.2 mg/s, providing a total thrust efficiency higher than 30% and a total specific impulse ranging from 1000 s to 1200 s.

The HT-100D will have different operating characteristics depending on the power supplied. For the scope of this thesis, we select one operating point and use it for all analyses. First we analyze the performance of the HT-100D from the figures below:

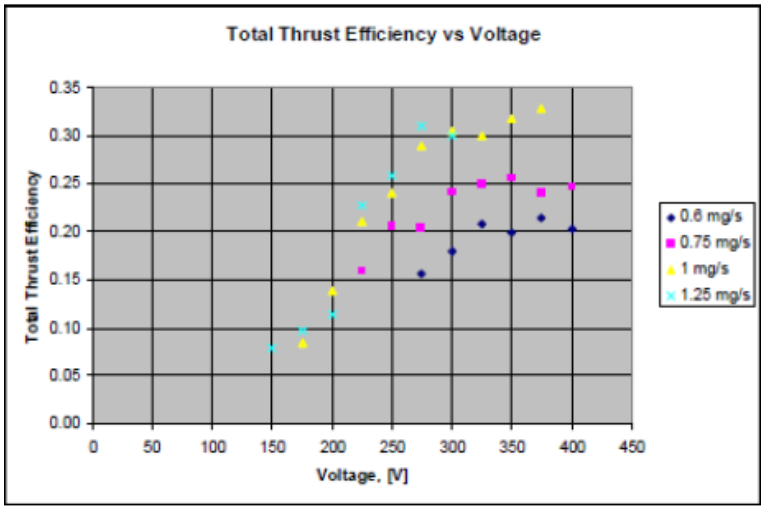

(a) Thrust efficiency vs. voltage

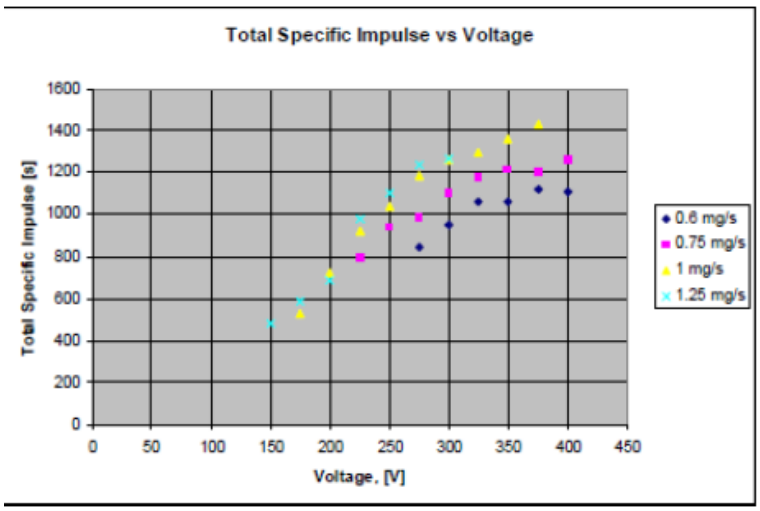

(b) Total Isp vs. voltage

Figure 13: HT-100D performance (Source:[5])

Thus we can see that the HT-100 is guaranteed to perform within the following operating characteristics range:

Parameter	Value
Thrust [mN]	6-18
Power [W]	120-400
Isp [s]	1000-1600
Thrust efficiency [%]	40
Lifetime [hours]	2000

Table 3: HT-100D operating range

We select an the below operating point to carry out the mission analysis.

Thrust	Isp	Power	Efficiency	Cathode mass flow rate	Anode mass flow rate
9 mN	1250 sec	200 W	40 %	0.15 mg/s	1 mg/s

Table 4: HT-100D:chosen operating point

We use these parameters to analyze the low-thrust operations of the HT-100D.

From[26], we find guaranteed performance related to thruster restart limitation times, maximum total impulse and number of ignitions. Therefore, we impose these as limiting constraint-based requirements for this mission.

1. "The thruster shall have the capability of providing a minimum of 5000 (TBC) operating cycles."
2. "The thruster life shall be minimum total impulse of 60000 Ns (TBC)."

Another important factor to be taken into consideration is the maximum thruster-on time in one ignition, which has an effect on the thruster interface temperature as well as on the power subsystem. For this thesis only the thruster interface temperature will be considered as a limiting constraint. Referring to below figure taken from [6], if the thruster-on time exceeds one hour, the interface temperature represented by the green line T2 INTERF rises exponentially .

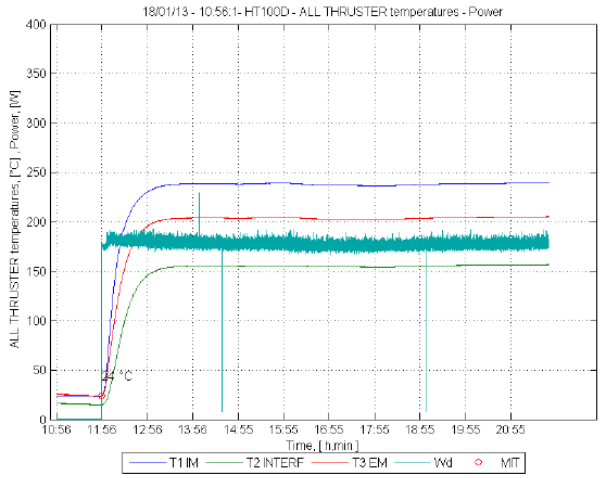

Figure 14: HT-100D operating temperature(Source:[6])

Therefore, to keep the thruster interface temperature below a reasonable value of $50°C$, we will restrict the maximum thruster-on time to up to one hour.

Based on the above discussions we define three requirements related to the constraints of the HT-100D.

REQ 1	Number of ignitions<5000
REQ 2	Total thruster-on time<1850 hours
REQ 3	Thruster-on time in one ignition<60 minutes

Table 5: HT-100D constraint based requirements

Therefore while analysis the mission and fixing possible mission scenarios, we will keep in mind the above requirements.

Chapter 3

Attitude:Fundamentals

Attitude and attitude motion of a spacecraft describes the orientation and rotational motion about its center of mass, and the computation of this orientation relative to either an inertial reference or some object of interest is referred to as attitude estimation. Attitude estimation is necessary in order to provide a reference for the attitude control system, so that it will be able to perform command engineering function, which is known as attitude control. The reference frames which will be used in this thesis are described in the section below.

3.1 Reference frames

By measuring the orientation of one frame with respect to the other, attitude measurements can be made possible. Therefore we will define the reference frames which are used in this thesis

1)Earth Centered Inertial (ECI)

The Earth Centered Inertial Frame is a non-accelerating inertial frame. The frame is located in the center of the earth and fixed towards the stars. This reference frame will be denoted as ECI. The earth rotates around the Z_I-axis. The X_I-axis points towards the vernal equinox, and the Y_I-axis completes a right hand Cartesian coordinate system, as shown in the figure below. This frame will be used when defining properties in low-earth orbit such as magnetic field and atmospheric density.

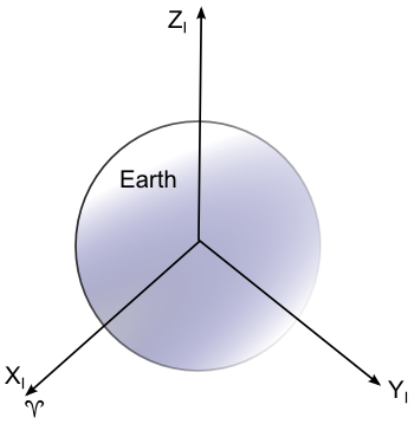

Figure 15: ECI Frame

2)Radial-Tangential-Normal (RTN)

The second coordinate frame is the Radial-Tangential-Normal orbit referenced coordinate frame. It is centered at the center of mass of the microsatellite, and therefore moves along the orbit path as the satellite does, but it maintains its orientation with respect to Earth. This frame will be denoted by RTN .The X_O always points towards the center of Earth, also called the nadir direction. The Z_O axis points in the orbit anti-normal direction where the orbit normal is defined by the right hand rule. The $Y_O$axis completes the orthogonal set. When the satellite is in a circular orbit the Y_O axis always coincides with the velocity vector of the satellite.

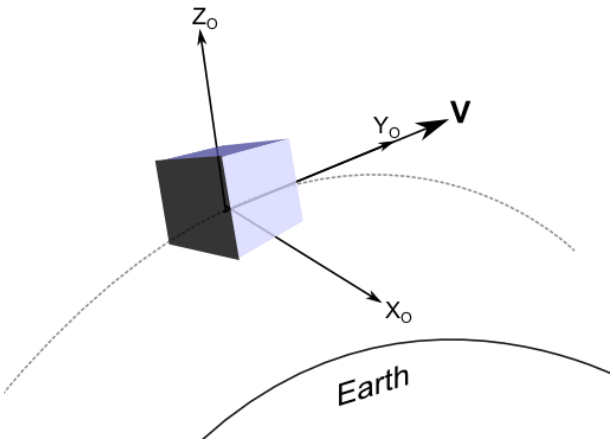

Figure 16: RTN Frame

3) Body Fixed (BF)

The body frame, denoted by BF shares it's origin with the orbit reference frame RTN. The rotation between the orbit reference frame and the body frame is used to represent the spacecraft's attitude. It's axes are locally defined in the spacecraft, and rotates with the microsatelite. The origin of this frame is in the center of gravity or the center of the volume.

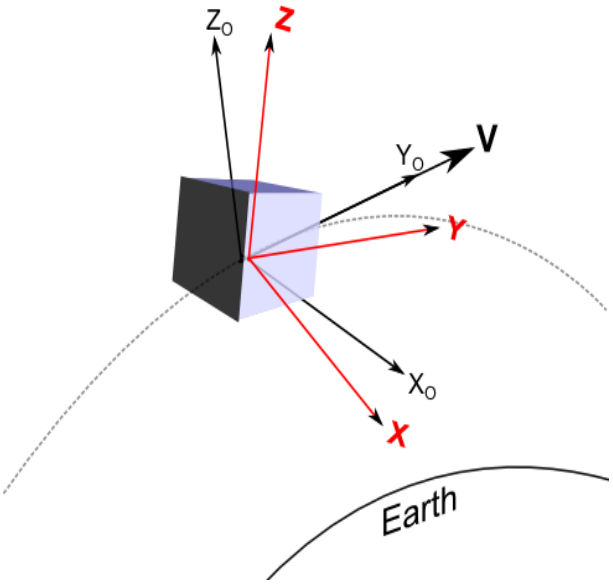

Figure 17: BF Frame

3.2 Attitude representations

The rotational relationship between the different reference frames gives the attitude description. Satellite attitude can be described by placing one frame within another frame and then following its temporal evolution.The relationship between different frames can be characterized in the following ways:

3.2.1 Direction Cosine Matrix

The Direction Cosine Matrix is a a 3x3 transformation matrix whose multiplication with a vector rotates the vector while preserving its length. The elements of the DCM correspond to the inner or dot between basis vectors (the dot product between unit vectors is the cosine of the angle between the two vectors). For example, the transformation matrix from RTN to BF (denoting the basis vectors as **b**and **r** respectively)can be given by[27]:

$$R_{RTN->BF} = \begin{bmatrix} \mathbf{b_x} \cdot \mathbf{r_x} & \mathbf{b_y} \cdot \mathbf{r_x} & \mathbf{b_z} \cdot \mathbf{r_x} \\ \mathbf{b_x} \cdot \mathbf{r_y} & \mathbf{b_y} \cdot \mathbf{r_y} & \mathbf{b_z} \cdot \mathbf{r_y} \\ \mathbf{b_x} \cdot \mathbf{r_z} & \mathbf{b_y} \cdot \mathbf{r_z} & \mathbf{b_z} \cdot \mathbf{r_z} \end{bmatrix}$$

Transformations between successive frames can be determined from a series of matrix multiplications. As an attitude representation the rotation matrix has nine parameters and hence six redundant.

3.2.2 Euler angles

The Euler angles are the rotation angles between two reference frames, and they are the base for the above DCM. The DCM can be decomposed into three rotations about three orthogonal axes. Both the sequence and the axes must be specified to clearly define the attitude (rotation) of interest. The same angle values used in a different sequence, or about different axes, results in a different attitude. For example, to rotate a particular reference frame, which is, in this case, the orbit reference frame (denoted by RTN) to the body frame(denoted by BF), we will follow a Yaw-Pitch-Roll (ψ, θ, ϕ) Euler angle sequence, which is the most commonly used Euler angle sequence for aerospace applications. As shown in the figure below, the D3SAT rolls around the X-axis, yaws around the Z-axis and pitches about the Y-axis.

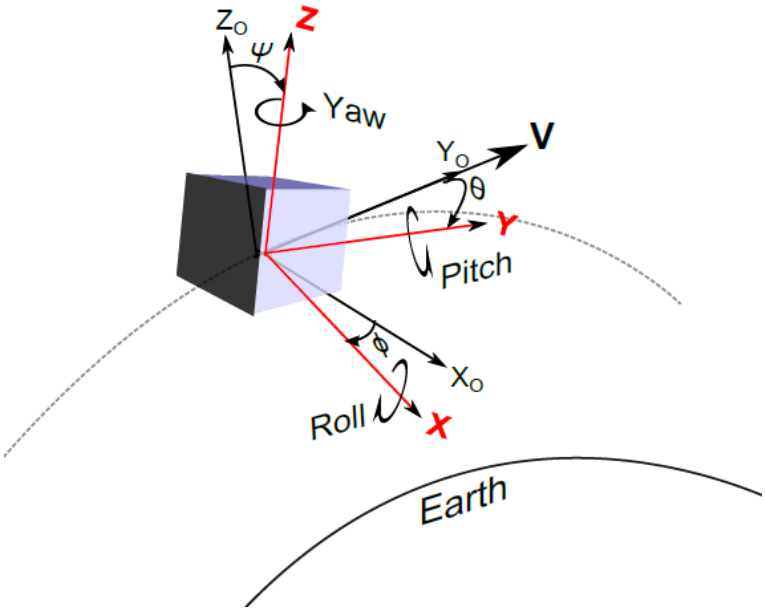

Figure 18: Yaw,Pitch and Roll axes of the D3SAT

The rotation matrix from RTN to BF is given by[28]:

$$R_{RTN-->BF}(\psi,\theta,\phi) = R_1(\phi)R_2(\theta)R_3(\psi)$$

$$R_{RTN-->BF}(\psi,\theta,\phi) =$$

$$\begin{bmatrix} cos(\theta)cos\psi & -cos(\theta)sin(\psi) & sin(\theta) \\ cos(\theta)sin(\psi)+sin(\phi)sin(\theta)cos(\psi) & cos(\phi)cos(\psi)-sin(\phi)sin(\theta)sin(\psi) & -sin(\phi)cos(\theta) \\ sin(\phi)sin(\psi)-cos(\phi)sin(\theta)cos(\psi) & sin(\phi)cos(\psi)+cos(\phi)sin(\theta)sin(\psi) & cos(\phi)cos(\theta) \end{bmatrix}$$

The Euler angles can be easily extracted from the rotation matrix as shown in [29]. It can cause singularity during numerical computations, due to the presence of trigonometric functions. When used in numerical analysis it is important to maintain orthogonality, which can be quite difficult. Euler angles are easy to visualize and interpretation of Euler angles are more intuitive and are therefore used as inputs to simulations and for illustration of simulation outputs. However, in order to execute command engineering functions, quaternions are used, which are described in the section below.

3.2.3 Quaternions

Euler's Theorem states that the rotation of a rigid body with one point fixed can be expressed by a single rotation about some fixed axis. In our application this fixed axis, also named the Euler axis, is represented by a unit vector in the BF.

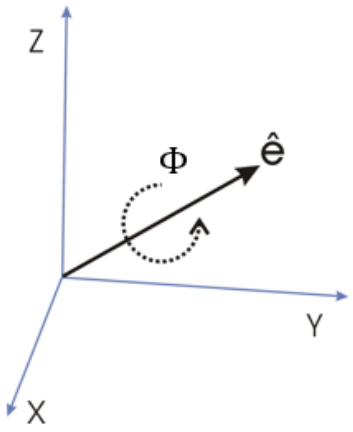

Figure 19: Euler's theorem

The quaternions are defined from by:

$$q_1 \triangleq e_1 sin(\frac{\Phi}{2})$$

$$q_2 \triangleq e_2 sin(\frac{\Phi}{2})$$

$$q_3 \triangleq e_3 sin(\frac{\Phi}{2})$$

$$q_4 \triangleq cos(\frac{\Phi}{2})$$

where $e_1, e_2$and e_3 are the X, Y and Z components of the unit Euler axis in the BF and represents the angle that the satellite is rotated about the Euler axis Φ. The quaternion elements are related to one another by the following constraint:

$$q_1^2 + q_2^2 + q_3^2 + q_4^2 = 1$$

Propagation of the orientation of an object is most efficiently done with quaternions.Quaternions are more compact than the DCM because it has only 4 elements instead of 9 in the transformation matrix.They yield no singularities and are therefore are used to represent the satellite's attitude during numerical computations. Propagation requires integration of only four kinematic equations and they are widely used because of simplicity of operations and small dimension.

Quaternions can be combined easily to produce successive rotations and DCM computation given by multiplication and addition of the quaternion elements without the use of trigonometric functions. The transformation matrix from the RTN frame to the BF frame is give by[30]:

$$R_{RTN-->BF} = \begin{bmatrix} q_1^2 - q_2^2 - q_3^2 + q_4^2 & 2(q_1q_2 + q_3q_4) & 2(q_1q_3 - q_2q_4) \\ 2(q_1q_2 - q_3q_4) & -q_1^2 + q_2^2 - q_3^2 + q_4^2 & 2(q_2q_3 + q_1q_4) \\ 2(q_1q_3 + q_2q_4) & 2(q_1q_3 - q_1q_4) & -q_1^2 - q_2^2 + q_3^2 + q_4^2 \end{bmatrix}$$

At this point it is convenient to define the terminology used to name the faces of the D3SAT, based on the BF frame, since these definitions will be used later in the thesis. From the figure below, the Y- face will contain the HT-100D. The X+ face will be the nadir-facing side. The X- face (not visible in the figure below) is the sun-facing face. The D3SAT will be fixed on the launch vehicle on the Z- face (not visible in the figure below) .

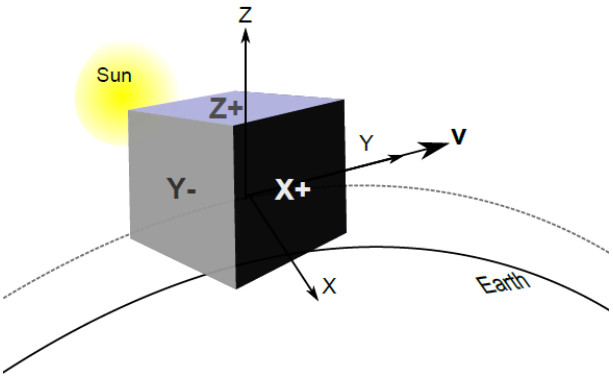

Figure 20: Definition of D3SAT faces

Chapter 4

Mission Analysis

Before analyzing the mission, we will first attempt to model the low-thrust maneuvers analytically and then compare them with the results of SATSLab. This analytical method is Edelbaum's method, and is described below.

4.1 Edelbaum's Method

The analytical method is Edelbaum's method, which is described in [31, 32]. The original Edelbaum algorithm is described in [33]. This algorithm is valid for total inclination changes$0° < i < 116°$. This numerical method assumes that the thrust acceleration magnitude is constant during the low-thrust maneuver phase. It also assumes that the magnitude of the thrust acceleration is low enough to include the assumption that the intermediate orbits of the transfer are circular. The initial thrust vector yaw angle ψ_O required for a given maneuver is:

$$tan(\psi_0) = \frac{sin(\frac{\pi}{2}\Delta i)}{\frac{v_0}{v_f} - cos(\frac{\pi}{2}\Delta i)} \tag{4.1.1}$$

Where $v_0 = \sqrt{\mu / r_o}$is the speed on the initial circular orbit and $v_f = \sqrt{\mu / r_f}$ is the speed on the final circular orbit. Since our analysis is carried out based on the assumption of zero eccentricity, $r_0 = R_E + h_0$and $r_f = R_E + h_f$, with $h_{0,}h_f$ being the initial and final orbital altitude. In the following analyses, the yaw angle $\psi_0$required for the satellite to slew along the body fixed Z-axis is calculated. The time evolution of this angle is given as:

$$\psi(t) = tan^{-1}[\frac{v_0 sin(\psi_0)}{v_0 cos(\psi_0) - f t}] \tag{4.1.2}$$

Where $f = F(t)/m(t)$,where $F(t)$ is the instantaneous thrust component and $m(t)$ is the time-varying microsatellite mass. For our analyses, we assume that $F_T = 9e-3$N (From table 4) and this remains constant. We can also neglect change in mass of the microsatellite, since it will be very small compared to the total mass of 40 kg.

The total velocity change for a low-thrust maneuver is given as:

$$\Delta v = v_0 cos(\psi_0) - \frac{v_0 sin(\psi_0)}{tan(\frac{\pi}{2}\Delta i + \psi_0)}$$

$$\therefore \Delta v = \sqrt{v_0^2 - 2v_0 v_f cos(\frac{\pi}{2}\Delta i) + v_f^2} \tag{4.1.3}$$

The total duration of the transfer is given by :

$$t = \frac{\Delta v}{f} \tag{4.1.4}$$

The temporal evolution of the velocity is given by:

$$v(t) = \sqrt{v_0^2 - 2v_0 f t cos(\psi_0) + f^2 t^2} = v_0 sin(\psi_0)\frac{\sqrt{1 + tan^2(\psi)}}{tan(\psi)} \tag{4.1.5}$$

The inclination varies with time as follows:

$$\Delta i(t) = \frac{2}{\pi}[tan^{-1}(\frac{f t - v_0 cos(\psi_0)}{v_0 sin(\psi_0)}) + \frac{\pi}{2} - \psi_0] \tag{4.1.6}$$

Neglecting all other perturbing accelerations, the acceleration due to propulsive thrust is expressed by:

$$\vec{f} = \frac{F}{m}\hat{u_f} \tag{4.1.7}$$

Where $\hat{u_f} = [u_{f_R} u_{f_T} u_{f_N}]^T$ is the unit pointing thrust vector expressed in the spacecraft-centered RTN frame. The components of the pointing thrust vector can be described with respect to the BF frame in terms of an in-plane pitch angle θ and an out-of-plane yaw angle ψas follows:

$$u_{f_R} = sin(\theta) \ ; \ u_{f_T} = cos(\theta)cos(\psi) \ ; u_{f_N} = cos(\theta)sin(\psi)$$

4.2 Drag Compensation

Since we are assuming a circular orbit, maintaining the altitude will give will prevent performance degradation with time. The microsatellite must ultimately put in the Δv which the perturbing forces take out. The frequency of these burns and the duration of each burn must be analysed in order to determine propellant consumption and the thruster-on time. Therefore, it is first important to analyze the perturbations which warrant the need for drag compensation.

4.2.1 Perturbations contributing to orbit decay

It is necessary to first analyze the forces causing orbit decay, so that we can include the necessary perturbations that contribute to orbit decay and therefore get a correct result for the requirements required to carry out drag compensation. Perturbations result in differential satellite motion which has components which are cyclic with the orbit period and, also, ones which result in continuous secular drift. Therefore in order to understand what causes orbit decay, we study the effect of major perturbations:

1)Drag

Atmospheric drag is the primary non-gravitational force acting on most satellites in LEO. Drag acts in a direction opposite to the velocity vector. This slows the satellite and removes energy from the orbit. Consequently, this reduction of energy causes the orbit altitude to lower, thereby resulting in further loss of energy. This occurs till the spacecraft reenters the Earth's atmosphere. Drag can vary by as much as an order of magnitude due to the attitude of the spacecraft and, particularly, the orientation of the solar arrays, with respect to the velocity vector. The atmospheric density at satellite altitudes varies by as much as two orders of magnitude depending upon the solar activity level, as will be seen in section 4.2.2.1. These variations result in overall difficulty for predicting satellite lifetime and required propellant consumption and thrust profile.

2)Earth oblateness

The Earth is typically modeled as a perfect sphere when it is an ellipsoid. The rotation of the Earth causes mass to be forced to the equator, thus slightly flattening the polar regions and due to this oblateness, the equatorial radii becomes greater than the polar radii. The increased mass around the equator creates an added gravitational effect on satellites, and this effect depends on latitude and longitude. The acceleration of a spacecraft can be found by taking the gradient of the gravitational potential function . One form of the geopotential function is[34, 35]:

$$\phi = (\frac{\mu}{r})(1- \sum_{i=1}^{\infty} J_n(\frac{R_{eq}}{r})^n P_n sin(L)$$

Where $R_{eq}$is the Earths equatorial radius, $P_n$are Legendre polynomials, L is the geocentric latitude ,$J_n$are the dimensionless geopotential coefficients where the first three values are:

$J_2 = 0.00108263, J_3 = -0.00000254, J_4 = -0.00000161$

The potential created by the non-spherical Earth affects all of the orbital elements causing orbit precession rates, and is termed the J2 effect. On average, the values of the semi-major axis, eccentricity, and inclination will not vary. However, the dominant effects occur in the ascending node, argument of perigee, and mean anomaly. The average rates are as follows[36]:

$$\frac{da}{dt} = 0$$

$$\frac{de}{dt} = 0$$

$$\frac{di}{dt} = 0$$

$$\frac{d\Omega}{dt} = -\frac{3}{2} J_2 n (\frac{R_{eq}}{p})^2 cosi$$

$$\frac{d\omega}{dt} = -\frac{3}{4} J_2 n (\frac{R_{eq}}{p})^2 (5cos^2 i - 1)$$

$$\frac{dM_0}{dt} = -\frac{3}{4}J_2 n(\frac{R_{eq}}{p})^2\sqrt{1-e^2}(3cos^2 i - 1)$$

Therefore, we can see that Earth's oblateness, while it does affect the orientation of the orbit, does not contribute to orbit decay. We can confirm this using STK.

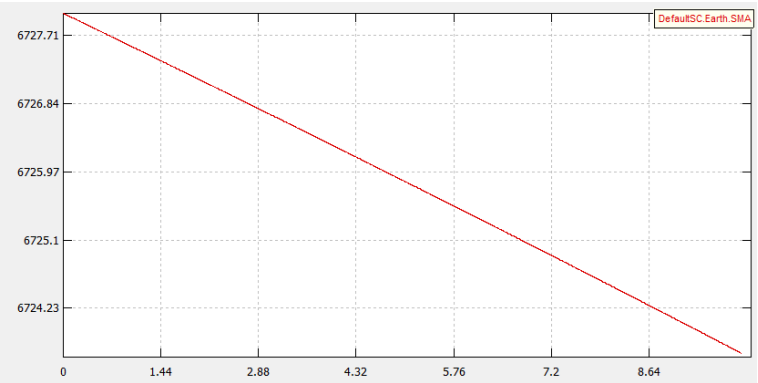

(a) Perturbation due to drag

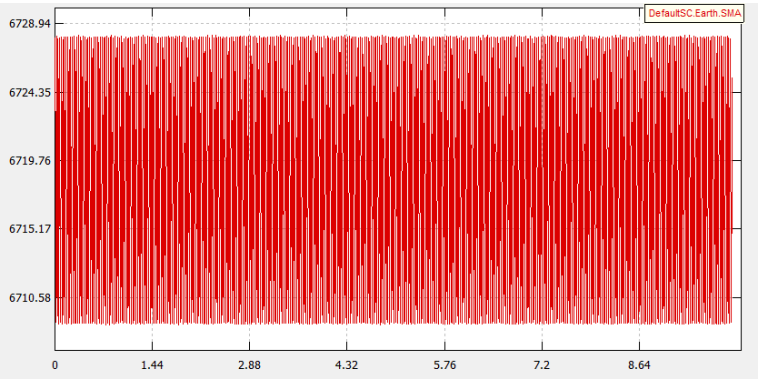

(b) Perturbation due to J2

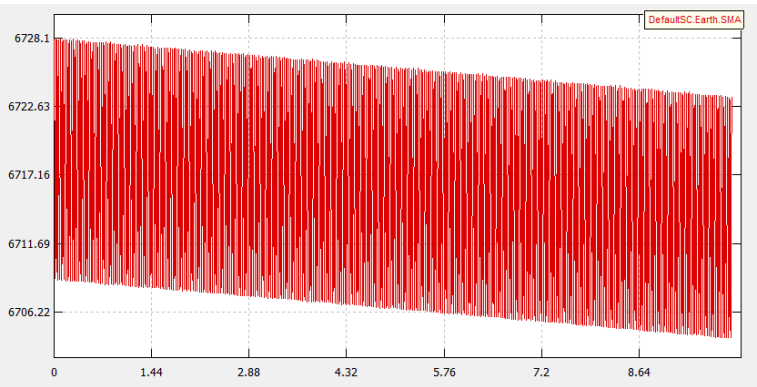

(c) Perturbation due to J2+drag

Figure 21: Effect of J2 on orbit decay

3)Third Body

The Sun and the Moon are the two gravitational forces relevant for an Earth-referenced orbit. They cause periodic variations in all the orbit elements. In comparison, the effect is similar to the J2 perturbations caused by the Earth's equatorial bulge. However, the Sun and the Moon's effects are generally noticeable in higher orbits, which are above GEO. The Sun and Moon apply external torques on orbits, causing a gyroscopic precession of the orbit about the ecliptic pole. There is little variation in the orbit elements $a, e \; and \; i$. The perturbation caused by the Sun and Moon mainly affect the right ascension of the ascending node and the argument of perigee thus requiring the need for station keeping in GEO and beyond. The right ascension of the ascending node and the argument of perigee precesses at the following rate[35]:

$$\dot{\Omega}_{\leftmoon} = -0.0038(cosi)/n \;\; \dot{\omega}_{\leftmoon} = 0.00169(4 - 5sin^2 i)/n$$

$$\dot{\Omega}_{\odot} = -0.00154(cosi)/n \qquad \dot{\omega}_{\odot} = 0.000774(4 - 5sin^2 i)/n$$

Lunar and solar (luni-solar) gravitational perturbation effects are most pronounced on high altitude or highly elliptic orbits. Since our microsatelltie is in a low altitude circular orbit, these luni-solar effects are not significant.

4)Solar radiation pressure

Solar radiation pressure (SRP) exerts a force on the spacecraft causing periodic variations in all of the orbital elements. The effect is strongest for satellites with low mass and large cross-sectional areas. The magnitude of the acceleration due to the SRP for satellites orbiting Earth is $a_{SRP} = -4.5e - 8 \times A_S/m$ Solar radiation pressure can cause changes in the orbit eccentricity resulting in a lower perigee altitude and therefore faster decay rates due to increased drag during that part of the orbit[37].Referring to [37].

We can summarise the perturbatios and their recommended treatments in the table below:-

Perturbation	Impact	Recommended treatment
Atmospheric drag	-Secular decay highly dependent on altitude	Negated by orbit maintenance
J2(Earth oblateness)	-Secular node rotation proportional to cosine of the inclination -Secular phase rotation (perigee rotation for an eccentric orbit)	Uncompensated
Luni-solar perturbations	-Small secular drift in inclination and node - Low amplitude oscillations in inclination and node	Uncompensated
Solar radiation pressure	-Small eccentricity growth	Negated by orbit maintenance

Table 6: Perturbations recommended treatment

Therefore, for our drag compensation analysis, we neglect the effect of J2 and luni-solar perturbations. As a future work, cancellation of J2 effects may be achieved with out-of-plane thrusting, in a similar way as what is done in-plane for drag compensation[38].

As a starting point, we first analyze altitude losses for the first day of the mission. We analyze how frequently the altitude drops from 50-500 meters below its nominal value , and then we calculate the thrust-on time and frequency of thruster firings in order to compensate for a range of altitude losses.We analyze the altitude decay and frequency of thruster ignitions using SATSLab and use analytical methods to calculate the firing time required to compensate for these losses.

4.2.2 Orbit decay

To get an idea of how much the semi-major axis decays per day and per orbit, we use the formula from [39]:

$$\Delta a_{rev} = -2\pi \frac{C_D A}{m} a^2 \rho_p exp(-c)[I_0(c) + 2eI_1(c)] \tag{4.2.1}$$

$$\Delta e_{rev} = -2\pi \frac{C_D A}{m} a \rho_p exp(-c)[I_1(c) + e(I_0(c) + I_1(c))/2]] \tag{4.2.2}$$

Where ρ_p= atmospheric density at perigee

$c = ae/H$ (H= atmospheric scale height)

$I_0$and $I_1$are modified Bessel functions of order 0 and 1 respectively, and with argument c.

Here, it becomes important to define the ballistic coefficient:

$$\beta = C_D{}^A/m \tag{4.2.3}$$

Drag coefficient C_D = 2.4,drag impacted area $A = 0.2\,m^2$ (refer to section 7.1.1 for justification of these values) and mass $m = 40\,kilograms$.

Our analysis will be restricted to circular or near circular orbits. Hence the above equations become more simplified and we get :

$$\Delta a_{rev} = -2\pi\beta\rho a^2 \tag{4.2.4}$$

$$\Delta T_{rev} = -6\pi^2\beta\rho a^2/v \tag{4.2.5}$$

$$\Delta v_{rev} = \pi\beta\rho a v \tag{4.2.6}$$

$$\Delta e_{rev} = 0 \tag{4.2.7}$$

4.2.2.1 Effect of atmospheric model on orbit decay

There are two fundamental operations that are involved in atmospheric drag: the determination of atmospheric density, and the interaction of the satellite surface with the atmosphere. The latter has been described in the following chapters so now, we will focus on the problem of determination of atmospheric density.The linkage with temperature is important because it causes much of the difficulty in developing an exact model for the density. The Earth's rotation exposes the atmosphere to the Sun, and the resulting solar heating affects density. Static density models are the simplest to use, whereas time-varying models are more accurate[40].Developing atmospheric models is extremely difficult and time consuming, but there are a wide range of available models. Relatively few new models have appeared in recent years with the largest advances coming in the form of corrections to existing models.The complex interaction of the solar wind and the geomagnetic effects on the atmosphere have resulted in a few parameters being

used to properly model this atmospheric density. Most atmospheric models use the $F_{10.7}$,a_p and $K_p$indices, primarily because they have been available since the 1930's. $F_{10.7}$is a measure of the influence of solar activity with location and time and a_P is a a measure of the influence of geomagnetic activity with location and time.Ultimately, the indices are a crucial step in determining the accuracy of any atmospheric model. If the variability of the parameter is greater than the effect it tries to model, the solution can become corrupted[41] . Therefore, we compare our long-term propellant consumption and thruster firing time using both solar maximum and NRLMSISE models, since the NRLMSISE-00 model is the most widely used and it will give us more realistic results, whereas the solar maximum density model can be thought of as a worst-case model.

Δa per orbit is found using equation 4.2.4,and $\rho$is taken from the solar maximum, solar minimum and solar mean densities in order to see what effect the density has on the orbit decay, and therefore, on the drag compensation requirements.To find Δa over one day, as a first approximation, one can assume linear decay. However ,for a more accurate value , equations 4.2.4 to4.2.6 are solved over one day, taking into the account the change of density as a function of the orbit number as shown in equation 4.2.8 , which is found in [42]:

$$\rho = -\Delta a \times \beta \times \frac{1}{v_{rel}^2} \times \left(\frac{n\sqrt{1-e^2}}{\sqrt{1+e^2+2ecos\nu}}\right) \tag{4.2.8}$$

Where $v_{rel} = v - \omega_{\oplus} r$ is the microsatellite velocity relative to the atmosphere of the Earth and $\omega_{\oplus} \sim 7.292115486e-5$ rad/s.

	Minimum density	**Mean density**	**Maximum density**
$\rho(^{kg}/_{m^3})$	2.35e-12	6.98e-12	1.98e-11
Δa_{orbit} (meters)	8	25	52
Δa_{day} (meters)	120	450	800

Table 7: Effect of atmospheric model on orbit decay

The above values are also confirmed using SATSLab.

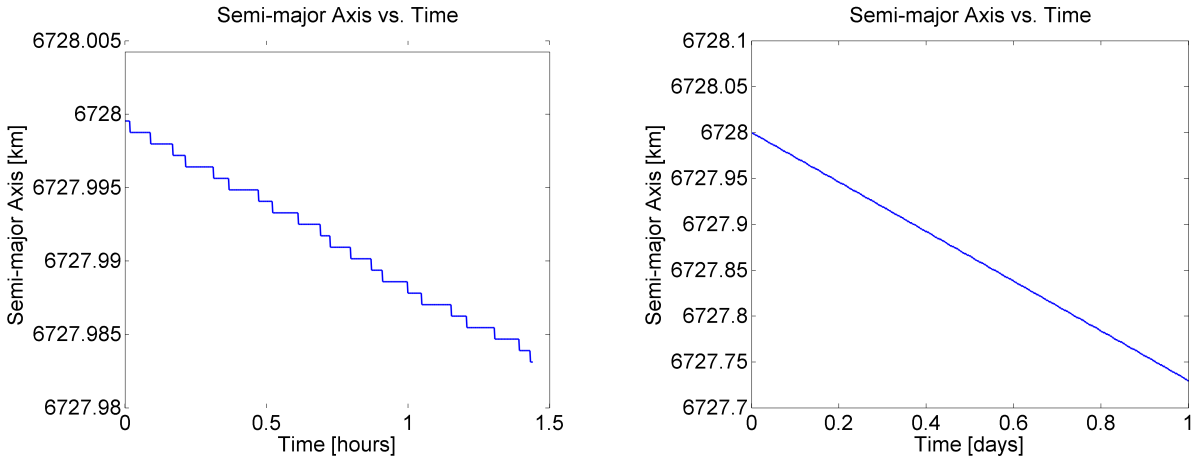

(a) 1 orbit (b) 1 day

Figure 22: Orbit decay during solar minimum activity

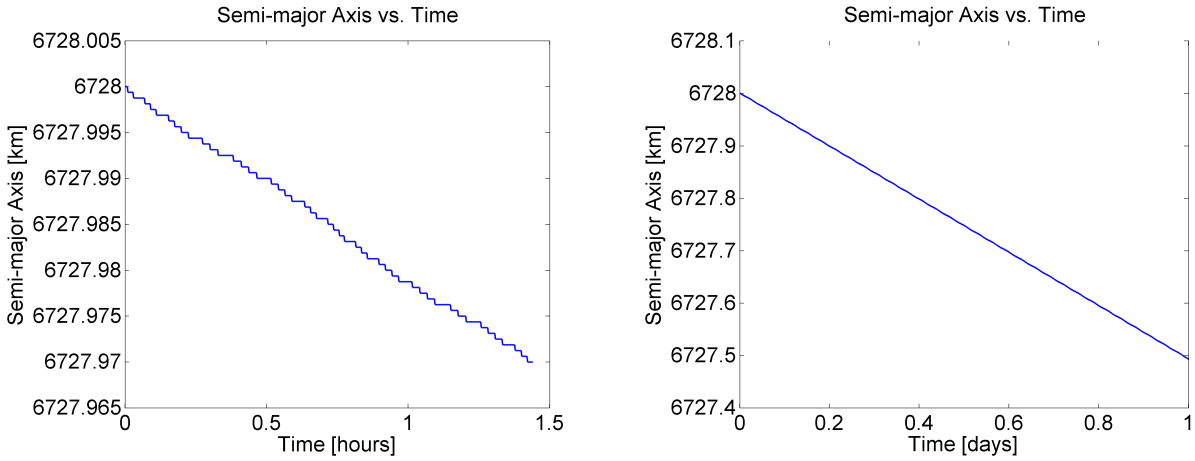

(a) 1 orbit (b) 1 day

Figure 23: Orbit decay during solar mean activity

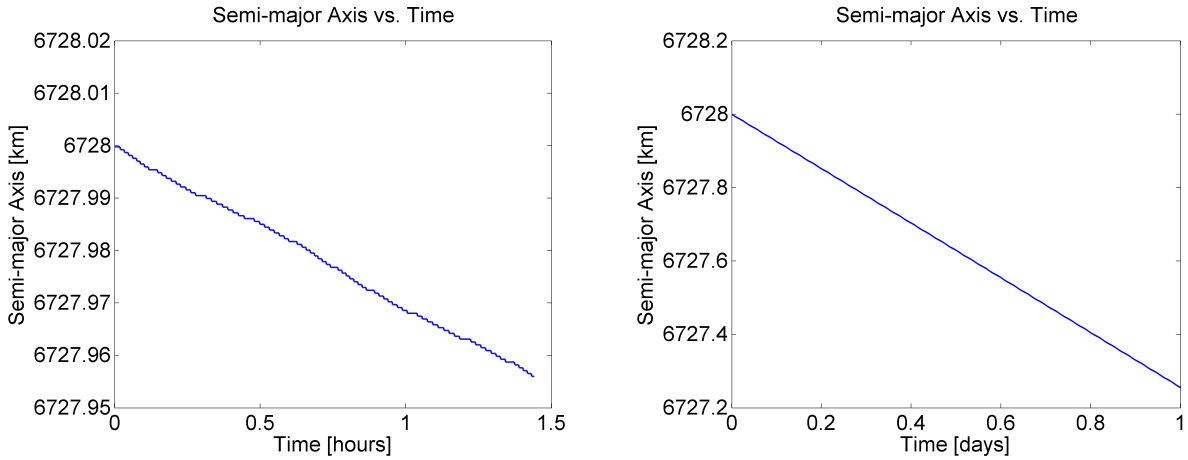

(a) 1 orbit

(b) 1 day

Figure 24: Orbit decay during solar maximum activity

4.2.3 Drag Compensation strategies

As drag slows the satellite the semi-major axis will be reduced, the period will be shorter, the satellite will move more rapidly, and will drift toward the front of the box. As the satellite moves forward, we must provide thruster firings from time-to-time to provide additional velocity to the satellite thereby raising the orbit, causing the satellite to slow down, and pushing it toward the desired nominal altitude. Thus, the basic operation is to measure how far the microsatellite has deviated from its original altitude and fire the thruster in the direction of motion as necessary to continually push the satellite toward the desired altitude as drag proceeds to move it forward. A key issue is to make thrusters firings sufficiently small that they never push the satellite beyond value of the the desired altitude. If the microsatellite drifts above its desired altitude, this will require thruster firings opposite to the direction of motion. We are considering a zero eccentricity orbit.

Since the thruster firing times and propellant consumption will be the absolute worst case during periods of maximum solar activity, we start with drag compensation using solar maximum conditions. We find the decay in the orbit based on the studies carried out in section 4.2.2.1 and use Edelbaum's algorithm described in section 4.1 to find theoretical thrust-on time values to raise the orbit to make up for the lost altitude. Two important assumptions have been made while solving equations 4.1.1 to 4.1.6 to find the thrusting time. The first assumption is that the pitch angle remains zero throughout the entire orbit raising maneuver. The second assumption is that the mass of the microsatellite remains constant . Since a constant thrust level of 9 mN is assumed , the second assumption also means

that the thrust acceleration ,given by equation 4.1.7, remains constant throughout the duration of the maneuver. From equation 4.1.3, we also find propellant consumption required. We analyze a starting altitude of 350 km, that is, semi-major axis of 6728 km and and inclination of 98°.In the table below , the term altitude tolerance means how far below the nominal value the altitude has dropped.

Altitude tolerance(m)	Thrust-on time(minutes)	Number of ignitions per day	Time between firings(minutes)	Time between firings(no. of orbits)
10	2	32	45	0.5
50	2	16	82	1
150	6	5	238	2
250	10	4	396	3
350	14	2	554	6
450	19	2	716	7

Table 8: Drag compensation strategies

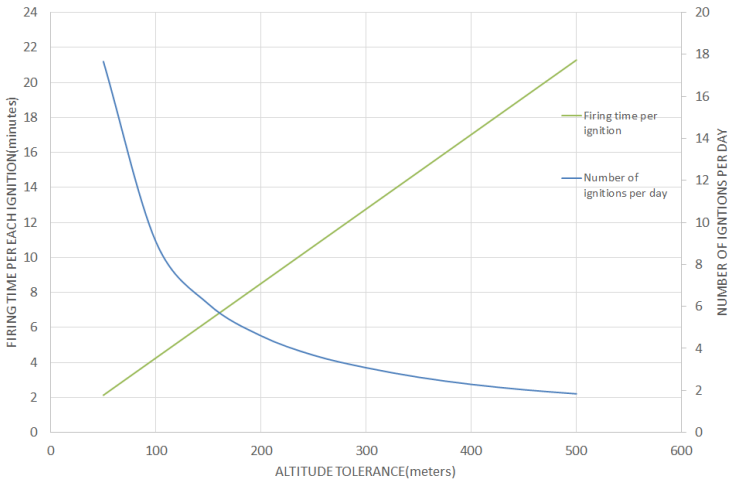

Figure 25: Drag compensation strategies:daily profile

On the following pages are given the daily thrust and semi-major axis profiles. While selecting a final drag compensation strategy, attention must be focused on selecting an altitude tolerance which is well above the stated accuracy of the position measuring device. It is also important to note that as atmospheric density decreases exponentially with altitude, continuously maintaining the satellite at the higher altitude results in lower drag and, therefore, a small but noticeable propellant savings.

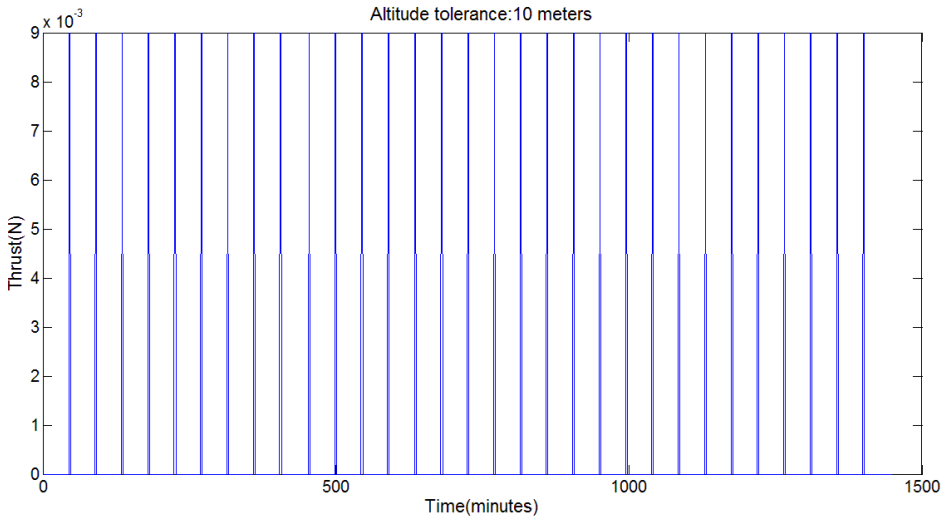

(a) Thrust

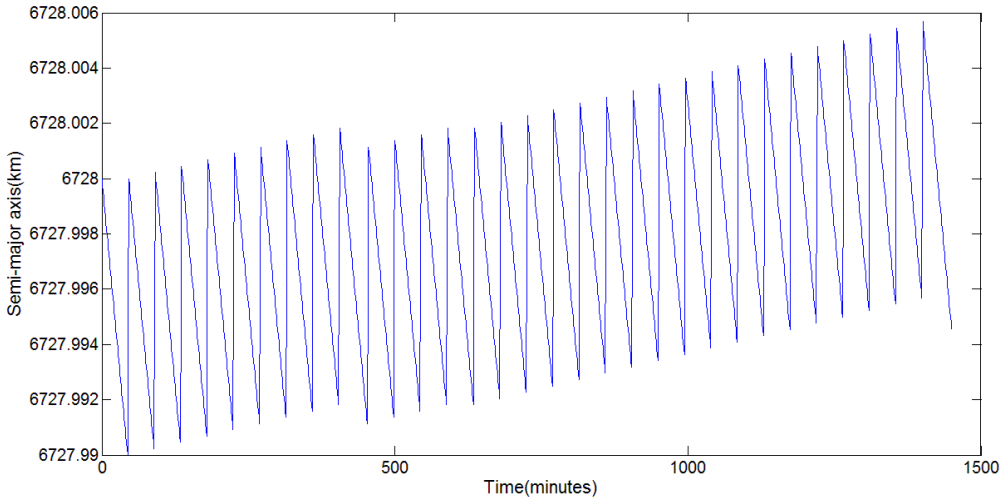

(b) SMA

Figure 26: Daily thrust and SMA profile for altitude tolerance of 10 m

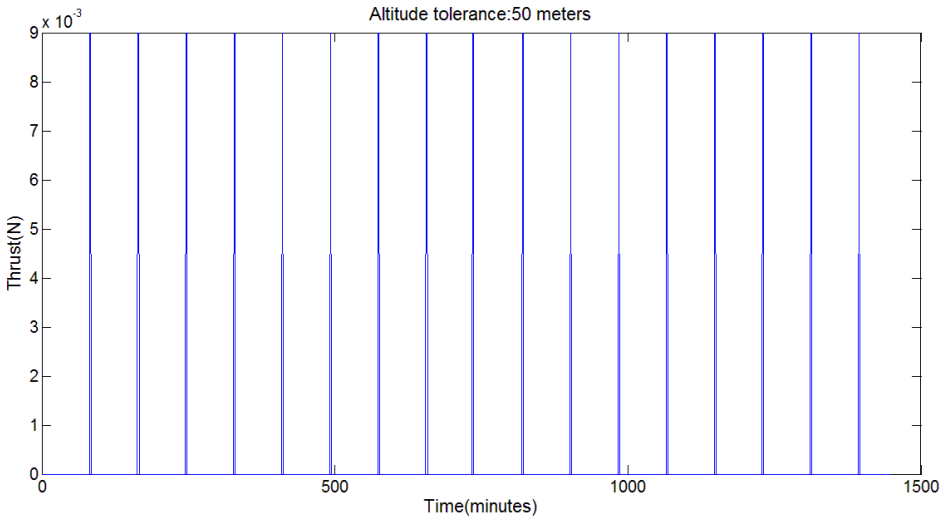

(a) Thrust

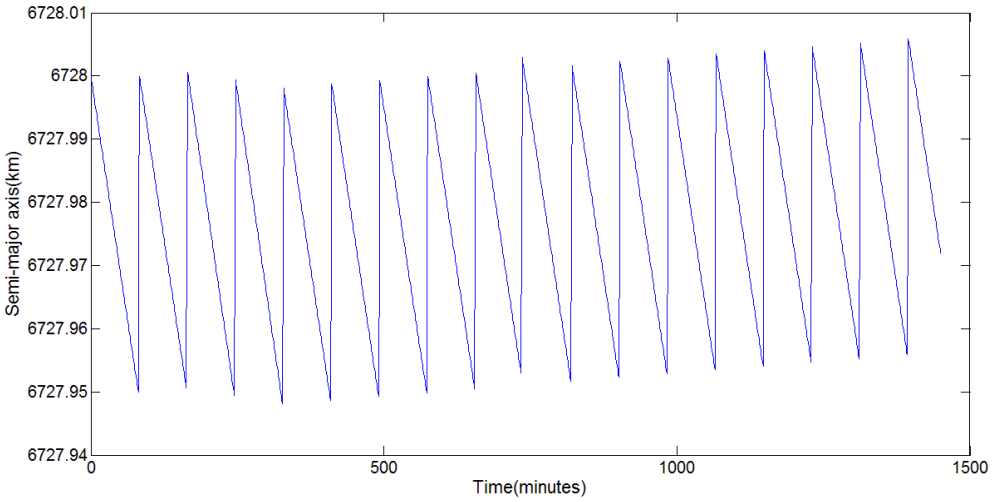

(b) SMA

Figure 27: Daily thrust and SMA profile for altitude tolerance of 50 m

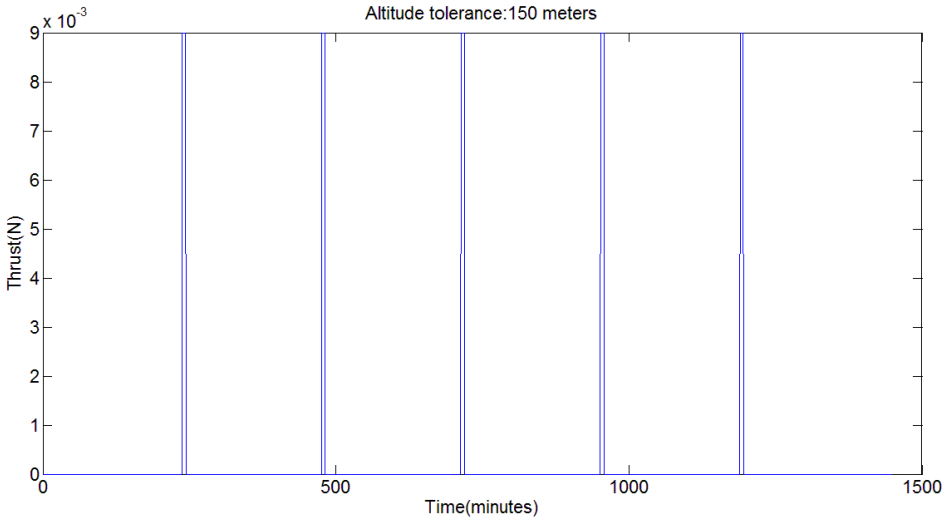

(a) Thrust

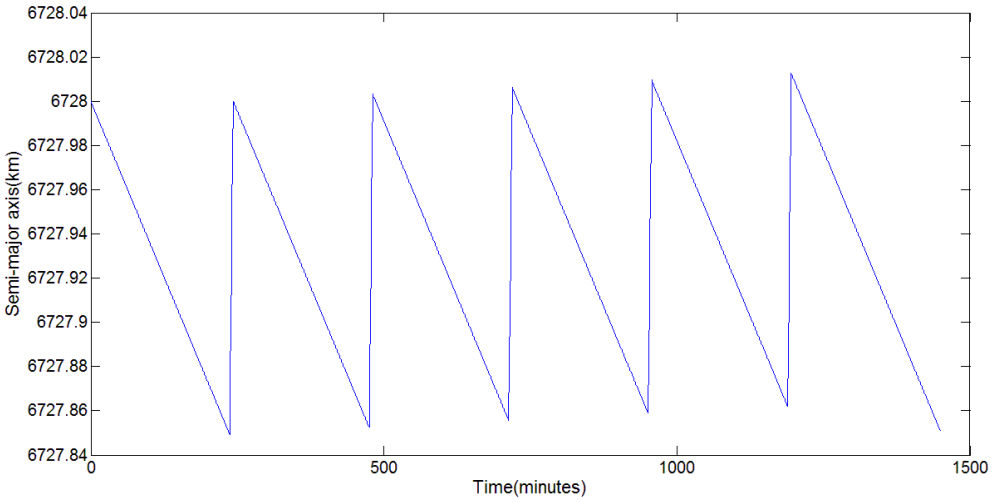

(b) SMA

Figure 28: Daily thrust and SMA profile for altitude tolerance of 150 m

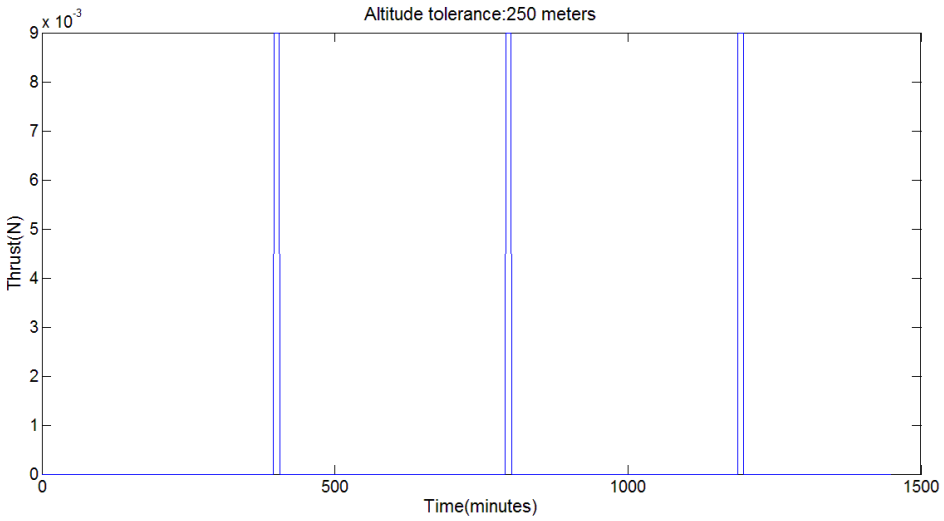

(a) Thrust

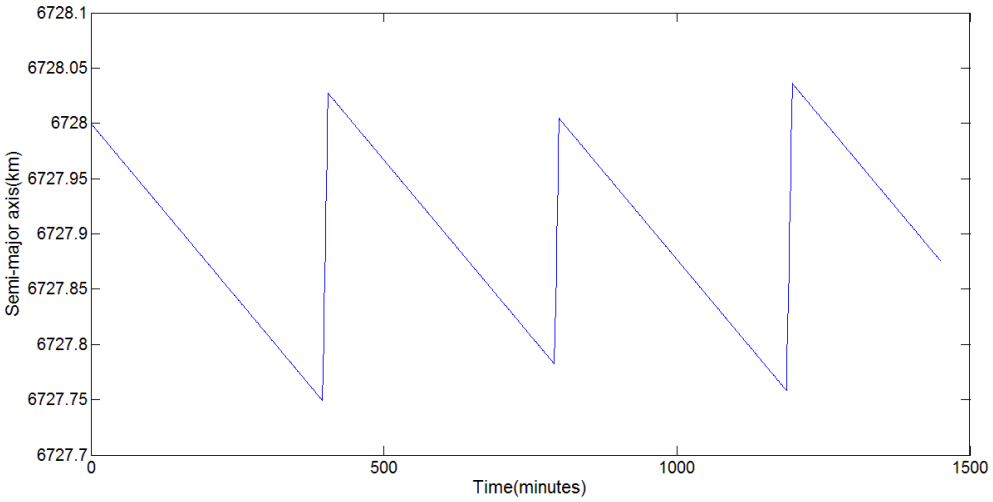

(b) SMA

Figure 29: Daily thrust and SMA profile for altitude tolerance of 250 m

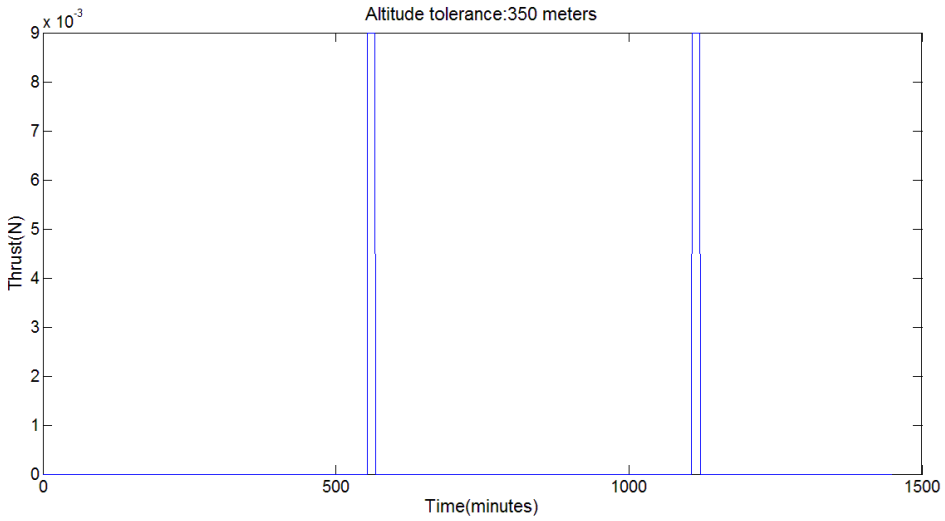

(a) Thrust

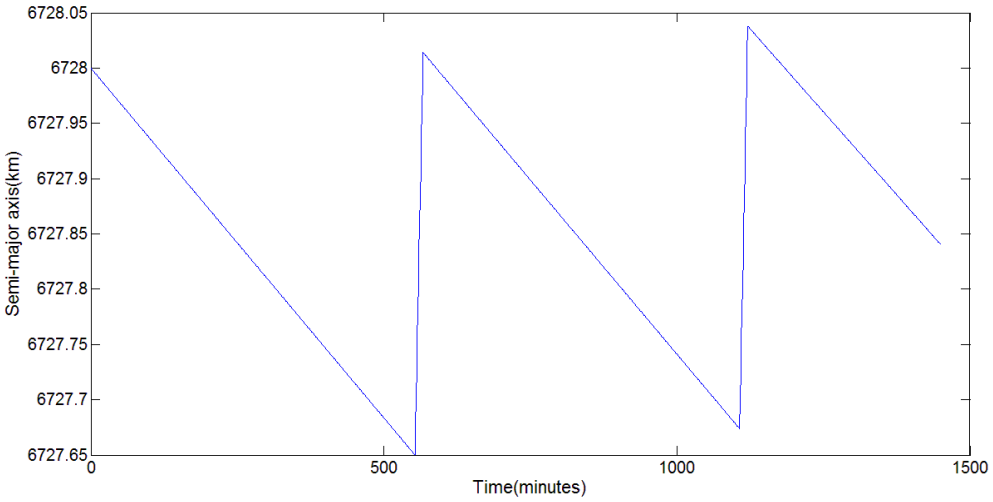

(b) SMA

Figure 30: Daily thrust and SMA profile for altitude tolerance of 350 m

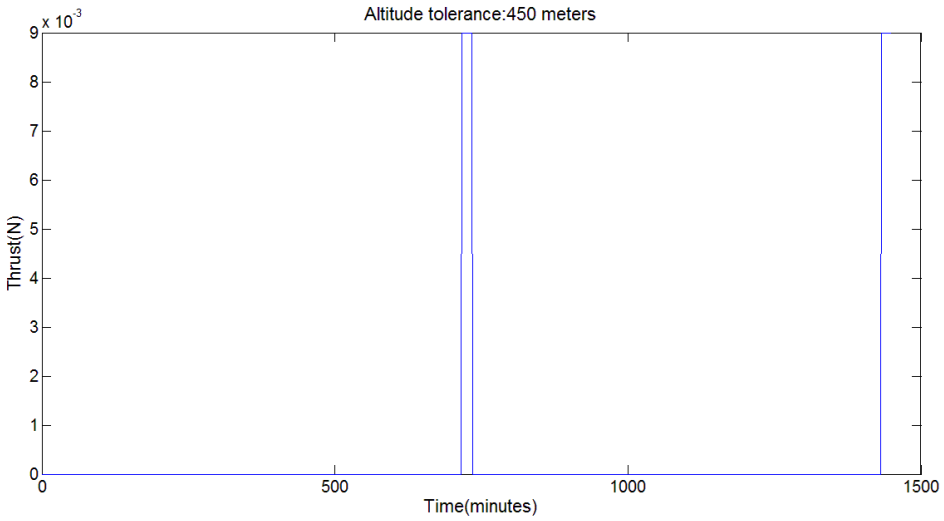

(a) Thrust

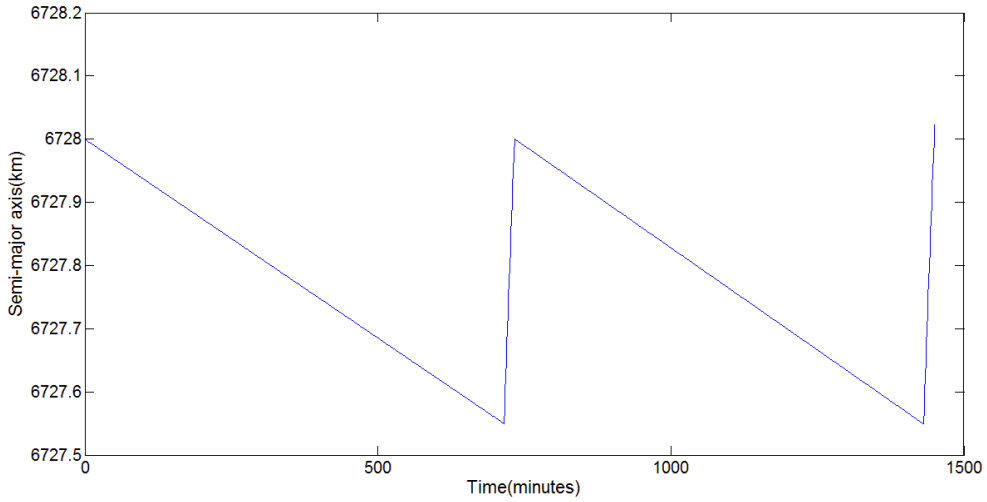

(b) SMA

Figure 31: Daily thrust and SMA profile for altitude tolerance of 450 m

To analyze long term thruster-on times and propellant consumption, if we assume that the same thrust profile will be valid for each day of the mission, it will not be correct , since the density will be time varying, that is, dependent on solar activity, and also the ballistic coefficient β given by equation 4.2.3 will increase, on account of microsatellite mass depletion due to propellant consumption. However, in order to get an idea of possible mission duration limits, we assume that the same thrust profile is valid for each day. In the figure below, we analyze a variety of possible drag compensation demonstration mission durations.

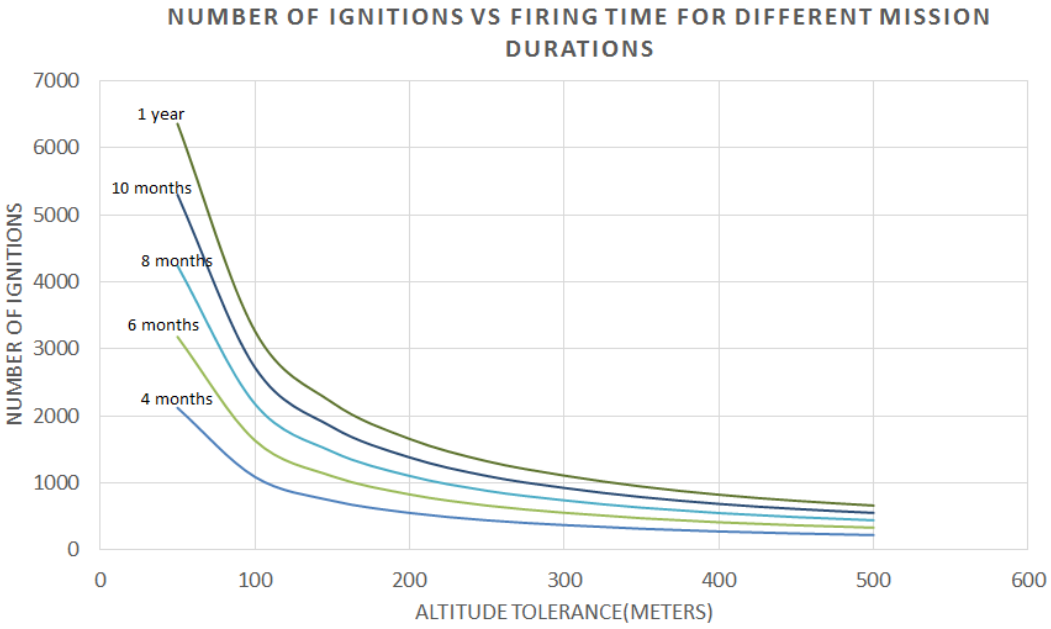

Figure 32: Number of ignitions required for various drag compensation strategies

Hence we can fix the duration of the drag compensation mission. We see that in order to satisfy REQ 1 from table 5, we choose a limit for the drag compensation phase of the mission, which we take as 3000 ignitions, since even deorbiting will be performed, as will be seen in section 4.3. The mission duration can be changed and accordingly so can the deorbiting strategy from section 4.3.

As is evident, study of short-term drag compensation will always give maximum values and the long term propellant consumption and thruster firing time will not rise linearly, as also seen in[5]. Therefore, we can analyze daily thrust profile using the studies carried out above, and for the long term analysis we can compare the total thruster firing time and propellant consumption using the worst case solar maximum density model and the more realistic NRLMSISE model, with indices $F_{10.7} = F_{10.7avg} = 250, a_p = 45$ (high long term solar and geomagnetic activities).

4.2.4 Reference case 1:Altitude tolerance of 150 meters

Altitude loss every 2 orbits	0.15 km
Thrust-on time every 3rd orbit	6 minutes
Time between firings	4.5 hours
Total thrust-on time in one day	30 minutes
Propellant consumption per day	1.8 grams
$\Delta v/day$	0.5 m/s

Table 9: Drag compensation:reference case 1

We know that thruster firing time and propellant mass consumption will not be a linear function of time. In fact , it will change as time progresses as the ballistic coefficient will increase due to mass depletion. In order to analyze long-term thruster firing time and propellant mass consumption, we use SATSLab using the maximum density model, the same model that was used to calculate daily drag compensation parameters.

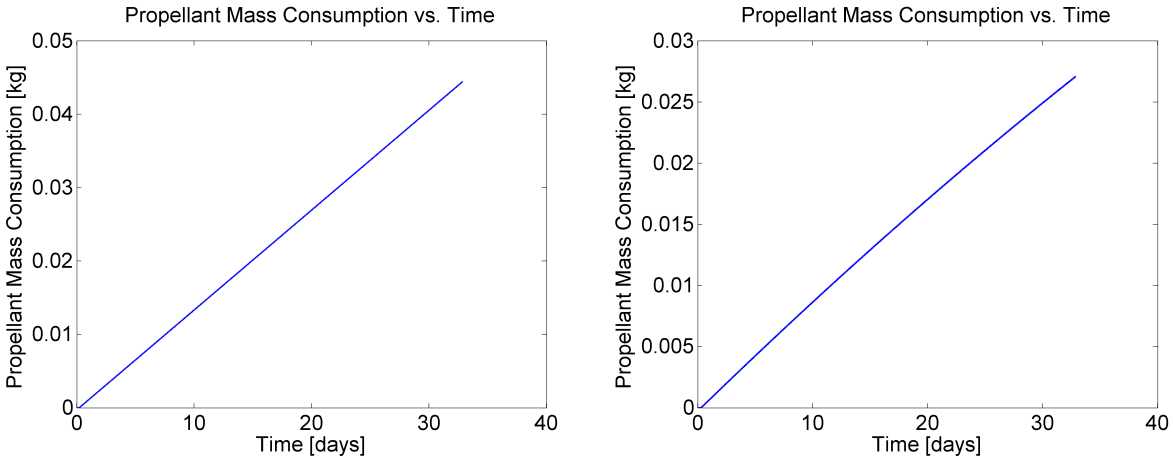

(a) Maximum density model (b) NRLMSISE-00

Figure 33: Reference case 1:1 month propellant consumption

However, to get a more realistic idea, we use the NRLMSISE-00 model:

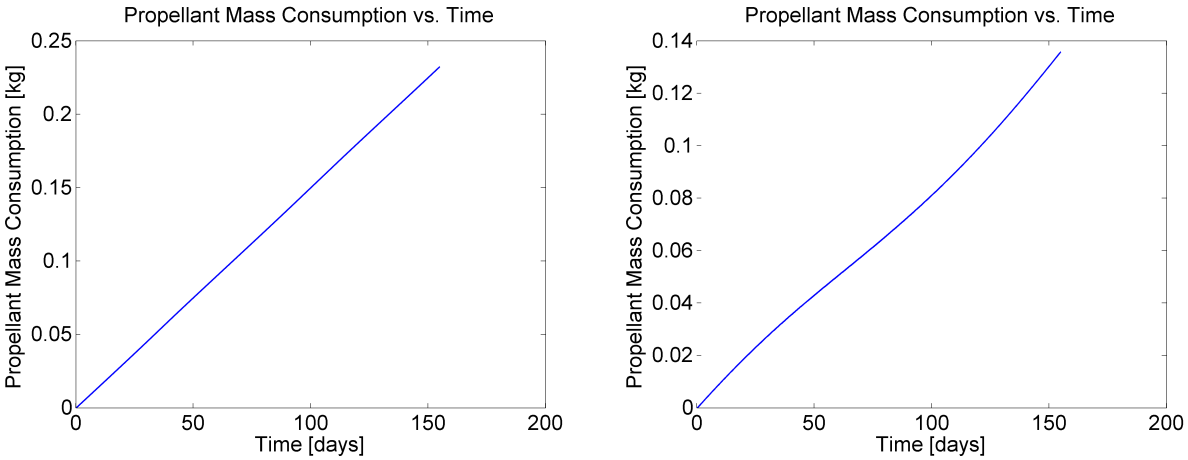

(a) Maximum density

(b) NRLMSISE-00

Figure 34: Reference case 1: 6 months propellant consumption

Requirements	1 month		6 months	
	Max Density	NRLMSISE-00	Max Density	NRLMSISE-00
Propellant(kg)	0.04424	0.027	0.2321	0.1355
Thruster firing (hours)	15.47	9.4348	80.816	47.22

Table 10: Requirements for reference case 1

We see that for the different models used there is a 40 % difference in thruster and propellant requirements, and this difference will tend to rise as time progresses.

4.2.5 Reference case 2:Altitude tolerance of 450 meters

Altitude loss every 7 orbits	0.45 km
Thrust-on time every 8th orbit	19 minutes
Time between firings	12 hours
Total thrust-on time in one day	38 minutes
Propellant consumption per day	1.855 grams
$\Delta v/day$	0.52 m/s

Table 11: Drag compensation:reference case 2

We know that thruster firing time and propellant mass consumption will not be a linear function of time. In fact , it will change as time progresses as the ballistic coefficient will decrease due to mass depletion.In order to analyze long-term thruster firing time and propellant mass consumption, we use SATSLab using the maximum density model, the same model that was used to calculate daily drag compensation parameters

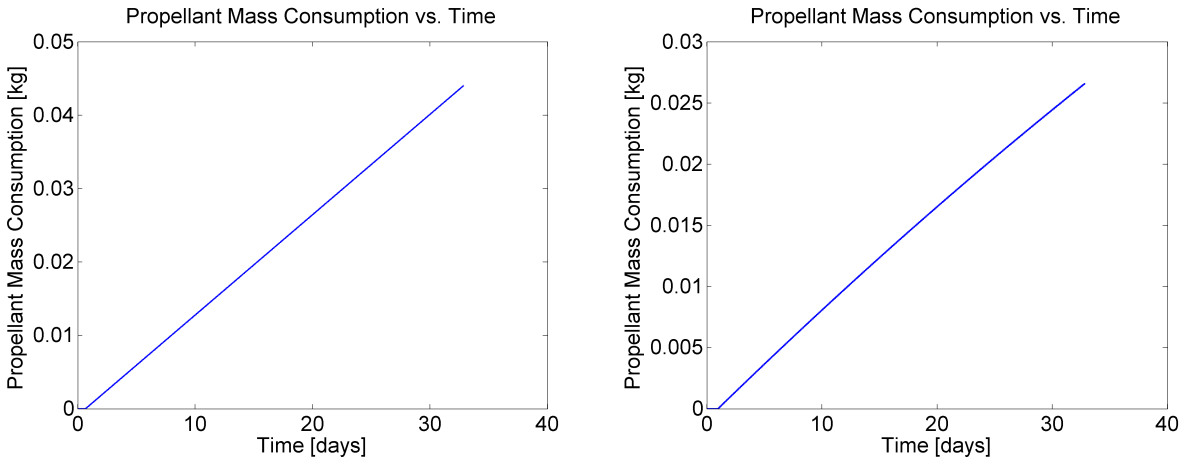

(a) Maximum density (b) NRLMSISE-00

Figure 35: Reference case 2: 1 month propellant consumption

However, to get a more realistic idea, we use the NRLMSISE-00 model:

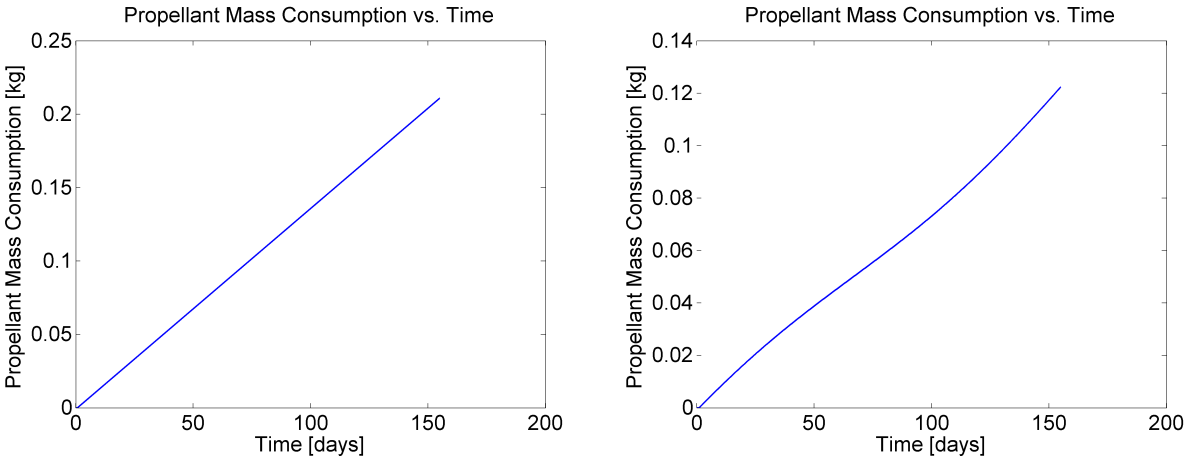

(a) Maximum density

(b) NRLMSISE-00

Figure 36: Reference case 1: 2 months propellant consumption

Requirements	1 month		6 months	
	Max Density	NRLMSISE-00	Max Density	NRLMSISE-00
Propellant(kg)	0.04402	0.02655	0.2105	0.122
Thruster firing (hours)	15.3289	9.2452	73.3698	42.5669

Table 12: Requirements for reference case 2

4.3 Deorbiting

The time taken for the microsatellite to naturally decay is highly dependent on the altitude, due to the exponential atmospheric density. Below is a graph showing time taken to naturally decay from various altitudes.

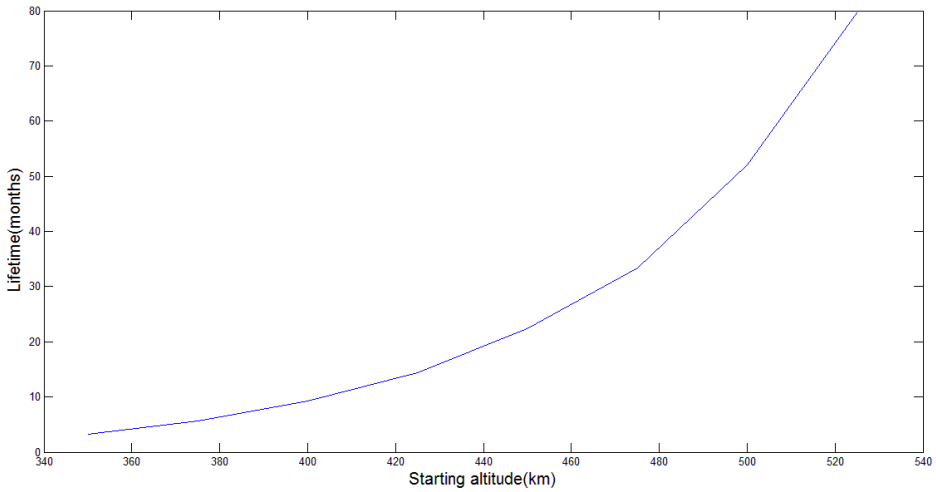

Figure 37: Satellite lifetime

As we can see, upward of 500 km, it will take about 5 years. At 350, it takes about 3 months. We have seen in section 2.1.2 the necessity to perform deorbiting.

4.3.1 Controlled vs Uncontrolled deorbiting

We are faced with two options to carry out end-of-life deorbiting:

1. OPTION 1: maneuver to an orbit for which atmospheric drag will remove the structure (uncontrolled deorbiting). The de-orbiting is initiated by one or more deceleration maneuver with the low-thrust of the HT-100D. These firing pulses by the HT-100D will be against the direction of motion, and thus firing will result in increasing the aerodynamic deceleration, ultimately reaching a lower orbit from where it can passively decay.There are no specific locations at which the thruster ignitions should take place, since we do not need to know the exact point of entry in the Earths atmosphere.

2. OPTION 2 :In case that the atmospheric destruction process is expected to be incomplete, an uncontrolled reentry is not permissible due to the risk for life on ground. This means that the HT-100D firing pulses will have to be executed and planned in such a way that the point of atmospheric re-entry, as well as point of impact on the ground will have to be predetermined. The controlled re-entry is initiated by one or several propulsive retro-burn maneuvers of sufficient Δv, in order to lower the perigee altitude. Such a controlled re-entry under a relatively steep atmospheric incidence angle

produces a confined ground impact area of parts which have survived the reentry.

Depending on the type of deorbiting chosen to be carried out, the deorbit phase of the mission will vary in complexity and duration. Controlled deorbit has to be carried out if the predicted risk of human casualties exceeds a specified limit, typically 0.01 percent per re-entry event, or the spacecraft contains hazardous objects with large masses and/or radioactive or poisonous materials. Very small satellites (mass less than or equal to 20 kg) burn up during re-entry for all initial conditions. Therefore controlled de-orbit is not required for this class of spacecraft, except if they have hazardous objects on board. Very heavy satellites survive the re-entry, at least partially in any case. Therefore in this case the re-entry should be controlled and stee[43]p enough to ensure a well-defined impact area and location. For medium-sized satellites it depends on the initial conditions whether they reach ground in larger pieces or not. To confirm that the D3SAT will burn up during reentry or lose at least enough mass to represent no severe hazard when impacting, we analyze some material thermal properties. The D3SAT can be considered as a sphere of diameter 0.4 m. The main structure is considered to be made of aluminum and the propellant tank of titanium.

Referring to [7]we get some material properties:

Material	$\rho[\frac{kg}{m^3}]$	$c_p[\frac{J}{kgK}]$	$T_m[K]$	$q_m[\frac{J}{g}]$
Titanium	4420	750	1900	400
Stainless steel	8030	611.5	1650	274
Aluminium	2800	751.1	870	385
Copper	8690	434.1	1356	243

Table 13: D3SAT material thermal properties

Where ρ :material density,c_p:specific heat capacity,T_m: melting temperature,q_m: heat of melting

Studies were done in [7, 44] taking account the temperature at a certain altitude , heat of melting and aerothermodynamic heat load generated:

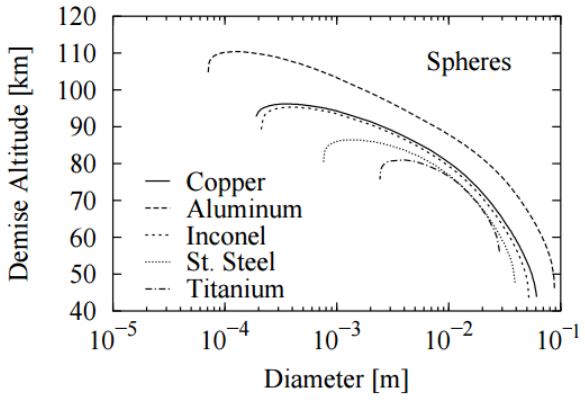

Figure 38: Demise altitude of D3SAT materials(Source:[7])

Therefore, as we can see, the D3SAT will completely break up due to friction with the atmosphere between 70-80 km altitude. Therefore controlled deorbit is not necessary.

However, for future work, suppose the need arises to track the trajectory of the ballistic reentry of the D3SAT, the conditions of the entry interface(point at which deorbit ends and natural reentry begins), will be required. This will allow employment of procedures to to make sure the D3SAT reenters at a specified set of entry interface conditions, such that precautions can be taken so that if the microsatellite does not burn up completely, any remaining debris will crash safely in uninhabited zones, J2 has a profound effect on the flight path angle at entry interface, and whether or not we take J2 into account, the entry flight path angle can differ as much as over 30% for higher initial orbits and about 10% percent for lower orbits[45]. Therefore, the J2 perturbation term is used in deorbiting analyses in addition to drag and SRP.

4.3.2 Deorbiting strategy

Using Edelbaums algorithm (equations 4.1.1 to 4.1.6), we find theoretical value of thruster-on time and propellant required to lower the altitude from an initial altitude of 350 km to a range of lower altitudes. As seen in figure 37, the time taken for a satellite to naturally decay is highly dependent on altitude, owing

to the exponential atmosphere. Therefore, we carry out an analysis to find the optimum altitude to which the microsatellite has to be lowered from the initial altitude of 350 km. This optimum altitude will be chosen based on a compromise between the time taken to lower the altitude and the time taken to naturally decay from that lowered altitude. In addition, REQ 2 from table 5 has to be also kept in mind.

The time taken to naturally deorbit from a range of altitudes below 350 km is found using Satellite Tool Kit. First, the firing time and propellant consumed for this orbit lowering maneuver is carried out without perturbations. To verify correct integration of Edelbaums algorithm, we verify the analytical results with SATSlab.The addition of perturbations: namely J2, drag and SRP decreases the firing time for deorbiting by an average of 20 %, as opposed to when orbit lowering is analyzed without perturbations.. This is due to the fact that the perturbations (primarily drag) passively helps to lower the altitude.

As stated in [43],in order to avoid excessive stabilization means, the active phase of the de-orbit maneuver shall be performed above an altitude of 300 km. However ,as we can see from the figure 39, it will take more than a month for the orbit to naturally decay from an altitude of 300 km. As a reasonable compromise between thruster operation time and time for natural decay, as a reference case ,we analyze the de-orbit maneveur from h=350 km to h=225 km.This takes 83.9834 hours(3.5 days) of continuous thrusting , with a propellant consumption of 0.2219 kg.

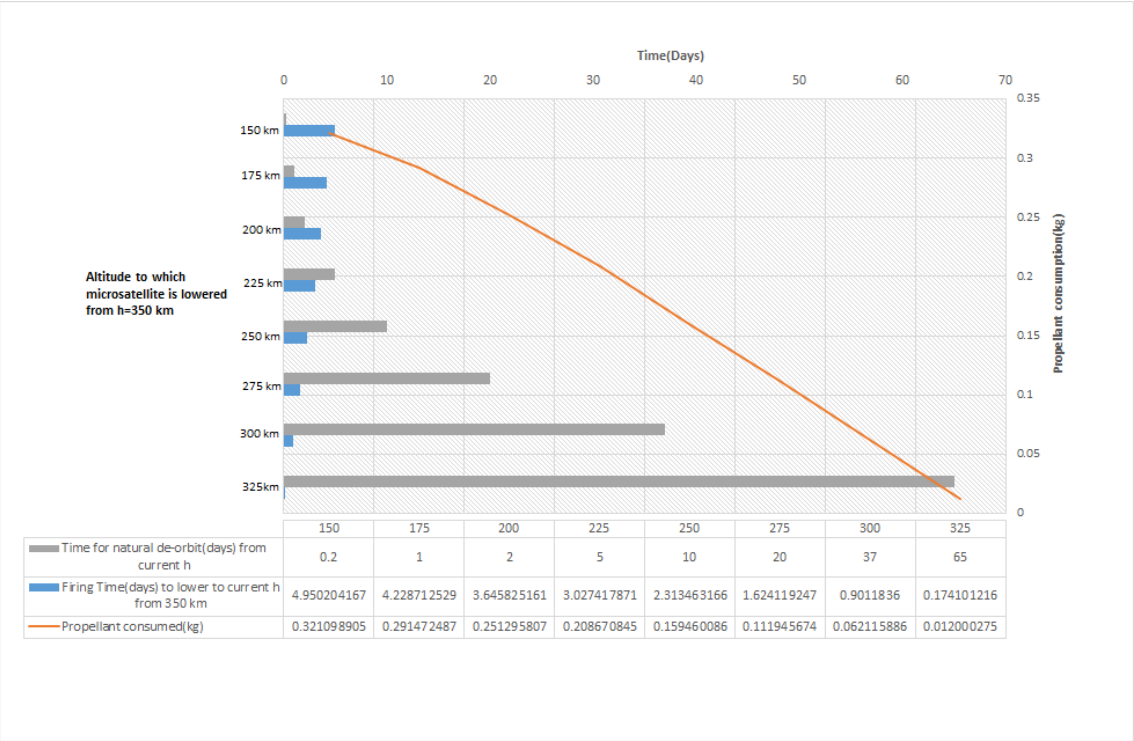

	150	175	200	225	250	275	300	325
Time for natural de-orbit(days) from current h	0.2	1	2	5	10	20	37	65
Firing Time(days) to lower to current h from 350 km	4.950204167	4.228712529	3.645825161	3.027417871	2.313463166	1.624119247	0.9011836	0.174101216
Propellant consumed(kg)	0.321098905	0.291472487	0.251295807	0.208670845	0.159460086	0.111945674	0.062115886	0.012000275

Figure 39: Deorbiting strategies

However, continuous firing is not practical, due to REQ 3 from table 5. Theoretically, as erosion of the channel wall due to ion bombardment reaches a level at which the magnetic circuit is exposed and eroded too, this will ultimately lead to a constantly higher decrease in thruster performance. Therefore, the last part of deorbit will take place with a decreasing performance, potentially causing higher deorbit times. However, this deorbiting firing time is very small compared to the lifetime of the HT-100D and therefore erosion effects can be overlooked. Restrictions from the point of the view of the power subsystem are not considered here, but are analyzed in [46].

Considering above limitations, we choose to not fire during the eclipse periods. This will increase the time taken to reach the goal. However, this strategy will also decrease thruster-on time and propellant consumption, since drag will passively help lower the altitude during the eclipse periods when the thruster is not operating.In the case of non-continuous firing, as seen in the below figures, it will take 69 hours(2.9 days) of firing and the transfer time will be 4.66 days The propellant consumption is less than 0.2 kg .

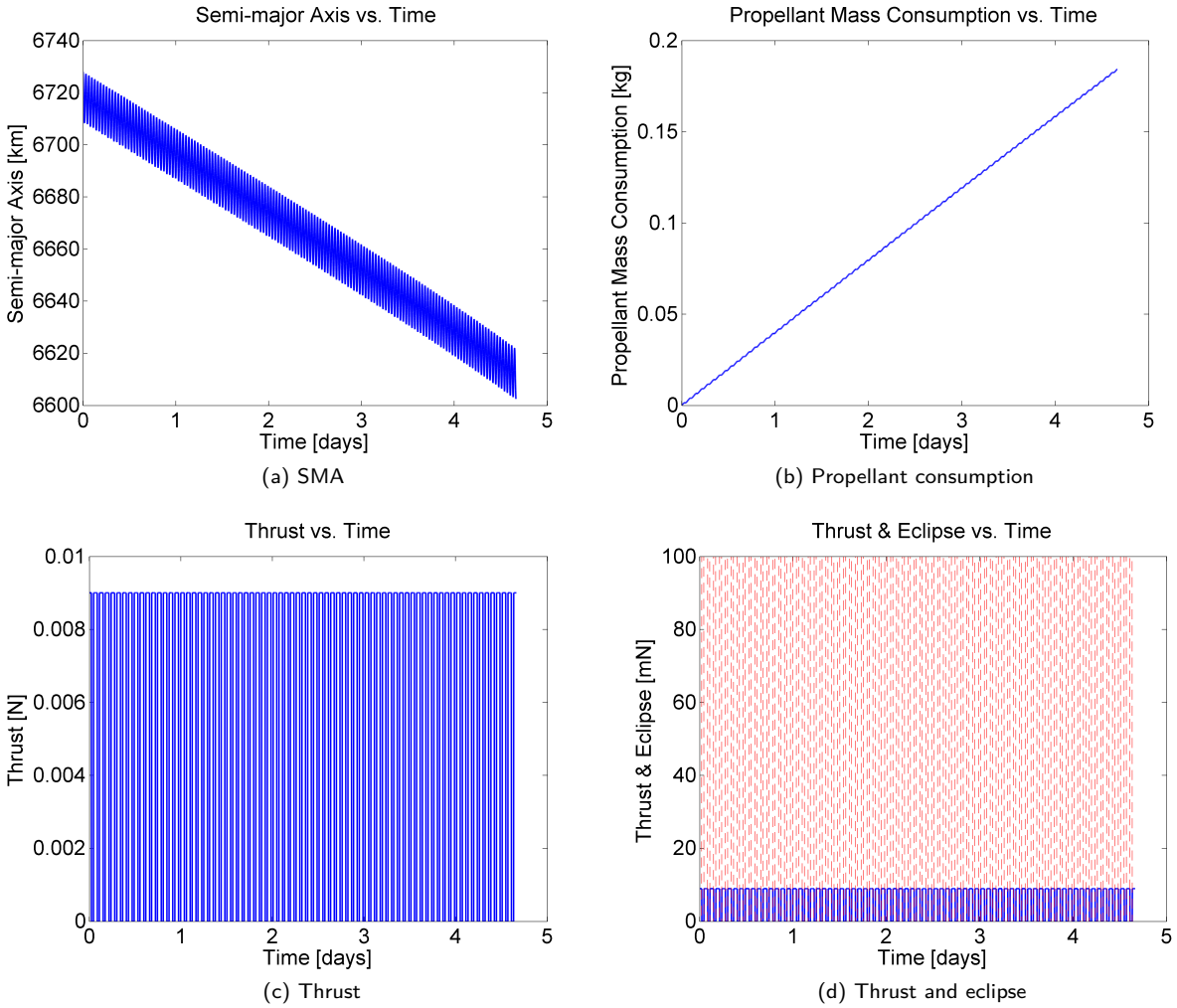

(a) SMA

(b) Propellant consumption

(c) Thrust

(d) Thrust and eclipse

Figure 40: End-of life deorbiting profile

From thus altitude of 225 km, the thruster will be switched off, and passive decay will take place. This phase will last 5 days, as seen in the figure below, during which the D3SAT will completely burn up during ballistic reentry.

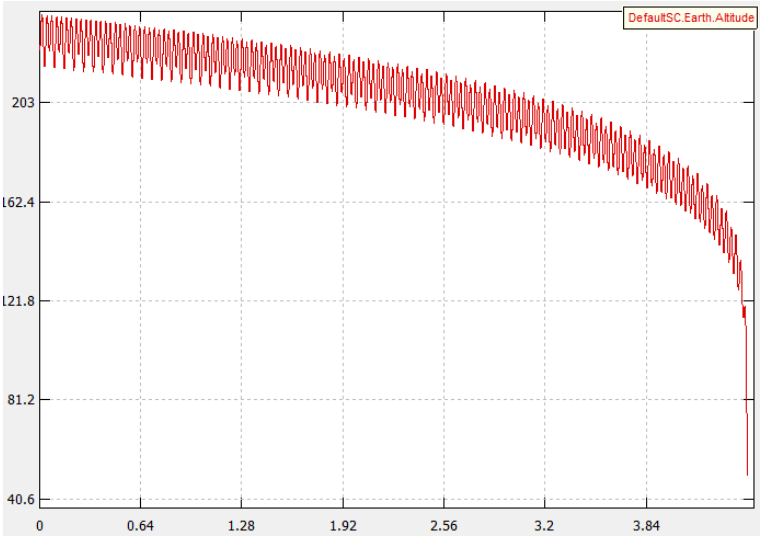

Figure 41: Passive decay orbit after uncontrolled deorbiting

4.4 Starting altitude consideration

The above mission analysis was carried out assuming a starting altitude of 350 km. However, due to launcher constraints, it is possible that the D3SAT may be inserted in a higher orbit. Assuming a starting altitude of 750 km, from figure 9, the D3SAT will have to be transferred to a lower altitude, due to the fact that at higher altitudes, due to the exponential atmosphere, the atmospheric drag will be negligible, and the HT-100D will not be able to be sufficiently characterized owing to the low orbital decay at high altitudes.

Therefore, the altitude will have to be lowered to below 500 km for the drag compensation mission to be meaningful. Below is a figure showing extra propellant required and thruster-firing times required to lower the altitude from 750 km to a range of lower altitudes.

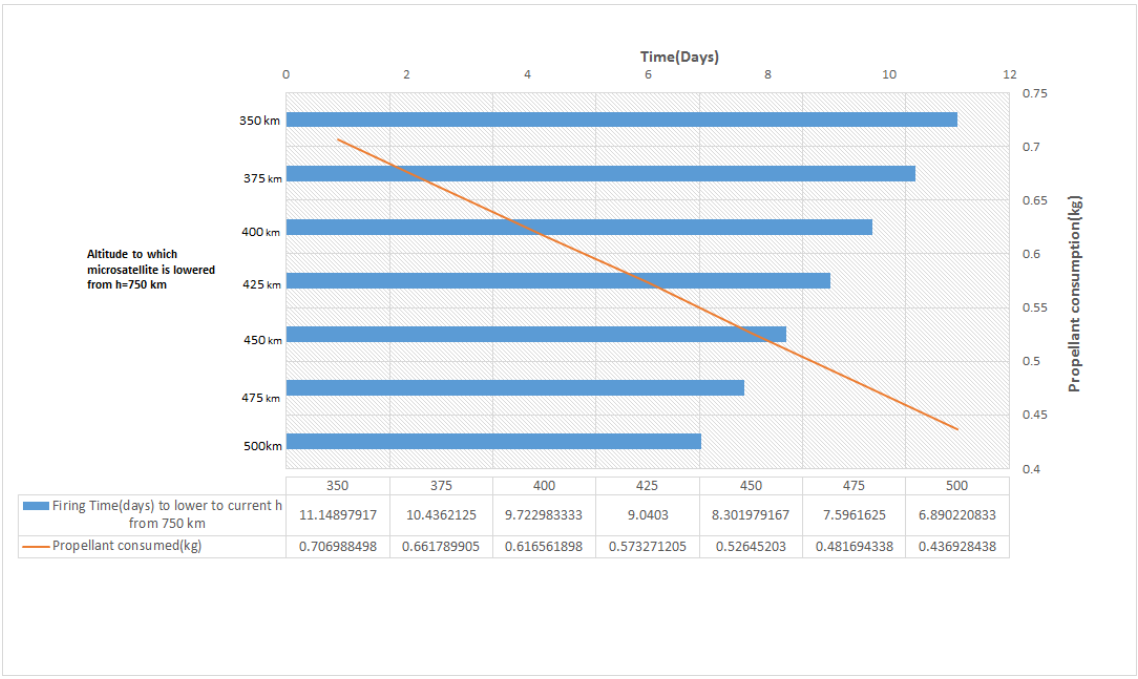

Figure 42: High starting altitude consideration

Therefore , if we assume that our mission is to be carried out at an altitude of 350 km, from the above graph ,we see that this will require about 12 days, or 268 hours of continuous thruster firing, and an extra propellant mass of 0.7 kg. However, considering the HT-100D operating constraints with regard to firing time, we choose not to fire during the eclipse periods. The below figures show the time taken to reach an altitude of 350 km from 750 km and the propellant mass required.

In the case of non-continuous firing, as seen in the below figures, it will take 255.114 hrs(10.6 days) of firing and the time taken to reach the goal will be 16 days. The propellant consumption is less than 0.7 kg .

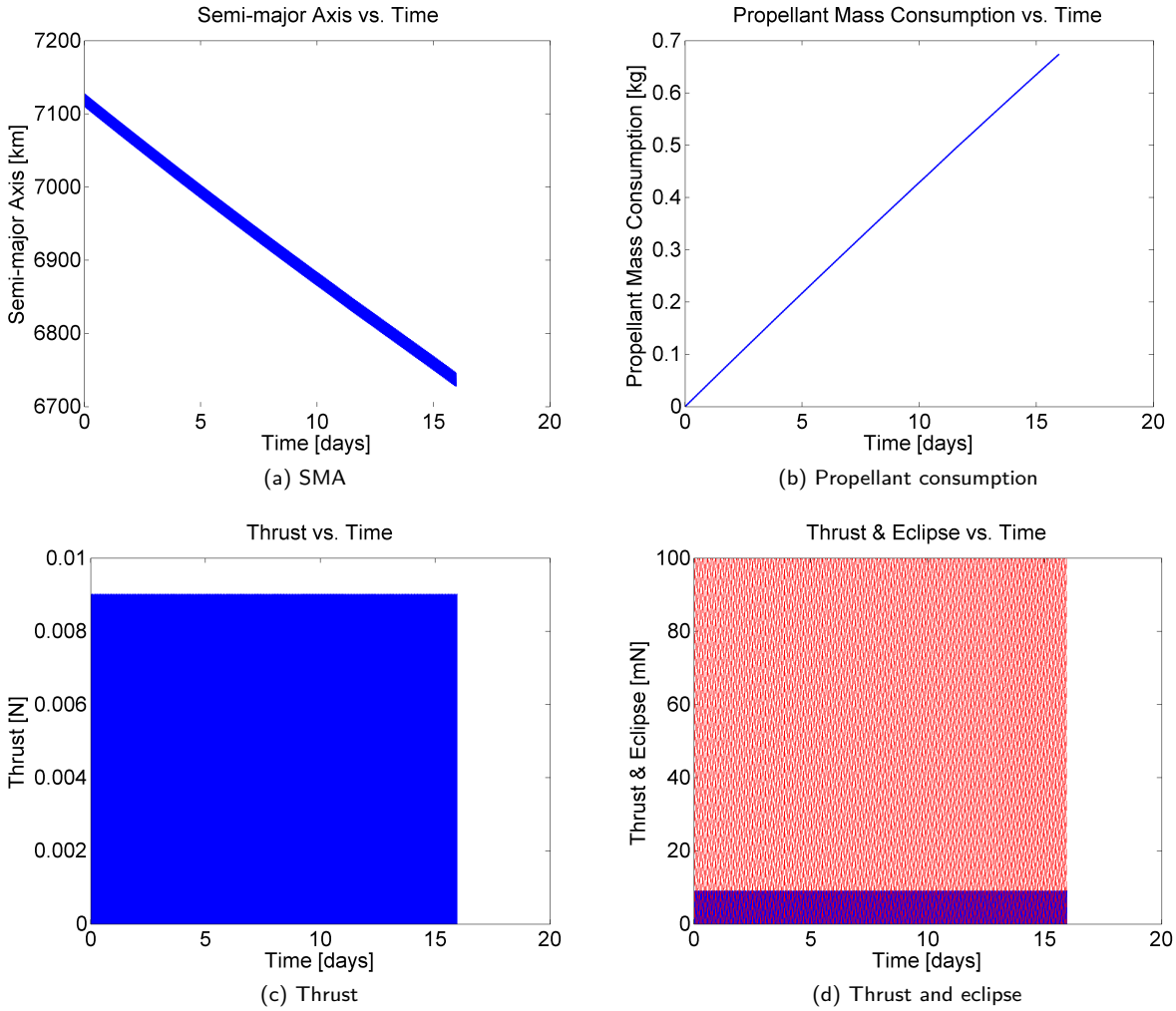

(a) SMA (b) Propellant consumption

(c) Thrust (d) Thrust and eclipse

Figure 43: Orbit lowering from high starting altitude of 750 km to 350 km

4.5 Summary

Assuming that the starting altitude is 750 km, we see that 16 days are added to the mission and 0.7 kg extra of propellant will be required.O verall, this mission can take place with very low propellant and if needed , the drag compensation strategy can be changed.

Phase	HT-100D firing time (hours)	Duration (days)	Propellant consumed (kg)	Number of ignitions
Orbit Lowering	255.114	16	0.69	240
Drag compensation	80.0816	180	0.2321	900
EOL Deorbiting	69	4.66	0.2	85
Ballistic reentry	-	5	-	-
TOTAL	406	205	1.122	1225

Table 14: Mission analysis summary

Chapter 5

ADCS Modes and Requirements

The ADCS will have to perform a range of functions. The operation of the ADCS will be divided into phases, or modes.

5.1 ADCS modes

1. DETUMBLING: When the D3SAT is released from its launcher, it will spin around in an uncontrolled way. Before the microsatellite can commence normal operations, this so-called tumbling has to be stopped.
2. INITIAL ATTITUDE ACQUISITION: After the D3SAT has been detumbled,information will be needed about the attitude. Measurements will have to be made with respect to an inertial reference frame (absolute measurement of attitude). Solar panel deployment will take place at the end of this mode.
3. NORMAL: Before firing the HT-100D, the microsatellite will have to be oriented along the orbit reference frame . The microsatellite body frame will not be naturally oriented with the orbit reference frame due to disturbances acting on the microsatellite.Disturbances acting upon a satellite can be divided into external and internal. External effects are those characterizing the Space environment. They would act event if a spacecraft itself was a rigid body. Internal disturbances are closely tied with spacecraft structure, in particular: internal moving parts and mass or radiation being emitted. If left uncompensated , the spacecraft will deviate from nominal attitude and therefore, the different components will not be pointing properly and the mission will not be successful.
4. HT-FIRING: This mode depends on the firing time and which phase of the mission is operative, namely drag compensation and deorbiting.If the D3SAT deviates from acceptable nominal attitude during firing of the HT-100D, the attitude control system will have to work to maintain the required attitude.
5. SLEW: The main objective of the mission is to evaluate the performance of the HT-100D. This involves collection of data about mass flow rate,voltage,thrust

level, operating temperature to see how different, if at all, is the performance of the HT-100 D in the space environment as opposed to the laboratory environment. Therefore, the antenna must point towards the ground station during a ground pass so that HT-100D performance data and even telemetry and house-keeping data can be sent to the ground station.

5.2 Requirements derivation

Based on the above mentioned modes, we can define mode-specific requirements.

5.2.1 Detumbling requirement

Referring to [47, 48]:

> "The worst initial tip-off rate of satellites separating from the launch vehicle is known to be 0.1 rad/s (1 rpm) in each axis."

This number is a common practice taken for microsatellites in the range of 30-90 kg.We add a 50% margin to the angular rate. This angular rate has to be reduced to a certain value, which is given to be $10^{-3} rad/s$ or $0.05^{\circ}/sec$ by the above referenced authors. Therefore as a first approximation we can state that the final angular rate of our microsatellite should be $\leq 0.05\ /sec (8.7e-4 rad/s)$.Also, we will need the detumbling time as low as possible without adding to the mass and power requirements of the ADCS hardware. Although there is no agreed upon time in literature within which detumbling should take place, we will impose a requirement that detumbling should take place within 3 orbits after release from the launch vehicle.

5.2.2 IAA requirement

It is generally difficult to get an accurate time taken to complete the detumbling mode.Hence , uncertainties arise as to the location of the microsatellite after detumbling. At the end of this mode , the microsatellite will deploy the solar panels. Considering an altitude of 350 km, the average eclipse time during one orbit is about 35 minutes, and the time period at this altitude is 91 minutes. Hence we wish to acquire the initial attitude information within the time duration during which the D3SAT is not in eclipse, so that solar panels can be deployed and

the mission can commence.Hence we impose a requirement that initial attitude acquisition should take place within 60 minutes after the detumbling mode is complete.

5.2.3 Normal requirement

This means characterizing the disturbance torque environment, and selecting appropriate hardware and control systems, which is done in section 7.4.1.However, we can define the require attitude knowledge in this section.That is, we can define the maximum acceptable deviation from nominal attitude , beyond which the ACS will have to start working.This requirement is based on the main mission objective, which is to demonstrate the working and monitor the performance of the HT-100D in a space environment, particularly with respect to drag compensation. In order to get a final criterion for the performance of the attitude estimation and control subsystem, we need to see the maximum deviation of the thrust beam from the geometrical thruster axis in order to determine the required performance of the attitude control system. Since the thruster cannot be gimballed,the deviation of the thrust vector from the body axes can arise only due to deviation of Euler angles ψ, θ, ϕ from perfect attitude$[\psi = \theta = \phi = 0]$.Ideally, the thrust vector is directed along tangential direction of the RTN frame.

Perturbations are deviations from a normal, idealized or undisturbed motion. We can consider thrust as an acceleration that introduces a perturbation to the microsatellite orbit. We wish to express the orbit behavior in terms of the orbital elements ,rather than in term of the position and velocity vectors because although position and velocity vectors undergo larger changes over time, most of the Keplerian elements undergo small variations in perturbed motion.It is much easier to see the effects of perturbations in slowly changing variables which reflect the size, shape and orientation of the orbit over time. We basically have to add the components of the thrust vector to the equations of motion of the satellite and integrate these equations in order to see the temporal orbit evolution. The general theory for finding the rates of change of osculating elements is known as the Lagrange planetary equations of motion or the Lagrange VOP (Variation of Parameters), which is for conservative effects. However, it is convenient to express the rates of change of the elements explicitly in terms of disturbing specific forces, or disturbing accelerations. For this we make use of the Gaussian VOPs, instead of the Lagrange planetary equations. The specific force components(perturbing accelerations:force/unit mass) are expressed in the RTN . From [22]:

$$\frac{da}{dt} = \frac{2}{n\sqrt{1-e^2}}\left\{esin(\upsilon)a_{pR} + \frac{p}{r}a_{pT}\right\}$$

$$\frac{de}{dt} = \frac{\sqrt{1-e^2}}{na}\left\{sin(\upsilon)a_{pR} + \left(cos(\upsilon) + \frac{e+cos(\upsilon)}{1+ecos(\upsilon)}a_{pT}\right)\right\}$$

$$\frac{di}{dt} = \frac{rcos(u)}{na^2\sqrt{1-e^2}sin(i)}a_{pN}$$

$$\frac{d\Omega}{dt} = \frac{rsin(u)}{na^2\sqrt{1-e^2}sin(i)}a_{pR}$$

$$\frac{d\omega}{dt} = \frac{\sqrt{1-e^2}}{nae}\left\{-cos(u)a_{pR} + sin(u)(1+\frac{r}{p})a_{pT}\right\} - \frac{rcot(i)sin(u)}{h}a_{pN}$$

$$\frac{d\upsilon}{dt} = \frac{h}{r^2} + \frac{1}{eh}\left\{pcos(\upsilon)\right\}a_{pR} - (p+r)sin(\upsilon)a_{pT}$$

However, the above Gaussian VOPs have some limitations. Firstly, they are limited to eccentricities less than 1 because of the presence of $\sqrt{1-e^2}$. This is suitable for us because we will be analyzing a circular orbit. However , due to the presence of e and i in the denominators, they become indeterminate for vanishing inclination and eccentricities. Therefore the need arises to express these equations in terms of non-singular elements. Referring to the work of [49], we have the Gauss equations expressed in terms on non-singular elements:

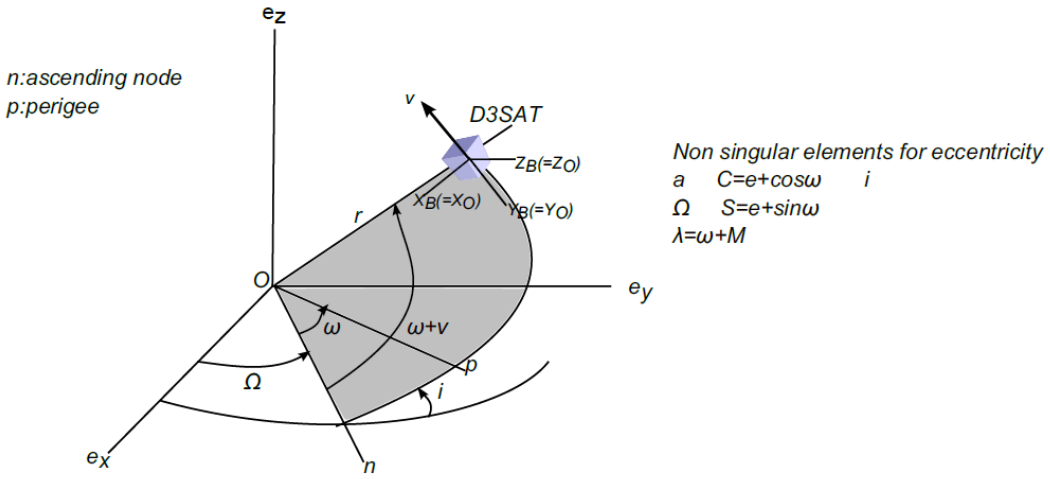

Figure 44: Gaussian VOPs expressed in non-singular elements

$$\frac{da}{dt} = \frac{2a\sqrt{1-C^2-S^2}}{\sqrt{\frac{\mu}{a}}}a_{pT} \tag{5.2.1}$$

$$\frac{dC}{dt} = \frac{-S\sqrt{1-C^2-S^2}}{\sqrt{\frac{\mu}{a}}}a_{pR} + \frac{1}{\sqrt{\frac{\mu}{a}}} \left\{-C\sqrt{1-C^2-S^2} - \frac{C}{2} + \frac{C(C^2+S^2)}{2(1+\sqrt{1-C^2-S^2}}\right\} a_{pT} - \frac{3}{2}S^2\frac{cos(i)}{\sqrt{\frac{\mu}{a}\sqrt{1-C^2-S^2}sin(i)}}a_{pN} \quad (5.2.2)$$

$$\frac{di}{dt} = -\frac{3}{2}\frac{C}{\sqrt{\frac{\mu}{a}\sqrt{1-C^2-S^2}}}a_{pN} \quad (5.2.3)$$

$$\frac{d\Omega}{dt} = -\frac{3}{2}\frac{S}{\sqrt{\frac{\mu}{a}\sqrt{1-C^2-S^2}sin(i)}}a_{pN} \quad (5.2.4)$$

$$\frac{dS}{dt} = \frac{C\sqrt{1-C^2-S^2}}{\sqrt{\frac{\mu}{a}}}a_{pR} + \frac{1}{\sqrt{\frac{\mu}{a}}} \left\{-S\sqrt{1-C^2-S^2} - \frac{S}{2} + \frac{S(C^2+S^2)}{2(1+\sqrt{1-C^2-S^2})}\right\} a_{pT} + \frac{3}{2}CS\frac{cos(i)}{\sqrt{\frac{\mu}{a}\sqrt{1-C^2-S^2}sin(i)}}a_{pN} \quad (5.2.5)$$

The thrust vector is perfectly aligned along the tangential direction of the RTN frame if the Euler angles between RTN frame and BF frame $\theta$and ψ are zero. The roll (ϕ) does not contribute to thrust misalignment. F_T is the nominal thrust provided by the HT-100D.When body frame (BF) deviates from the orbit reference frame (RTN), off-tangential components of the thrust are produced , which result in perturbing forces. These forces are resolved as shown in the figure below:

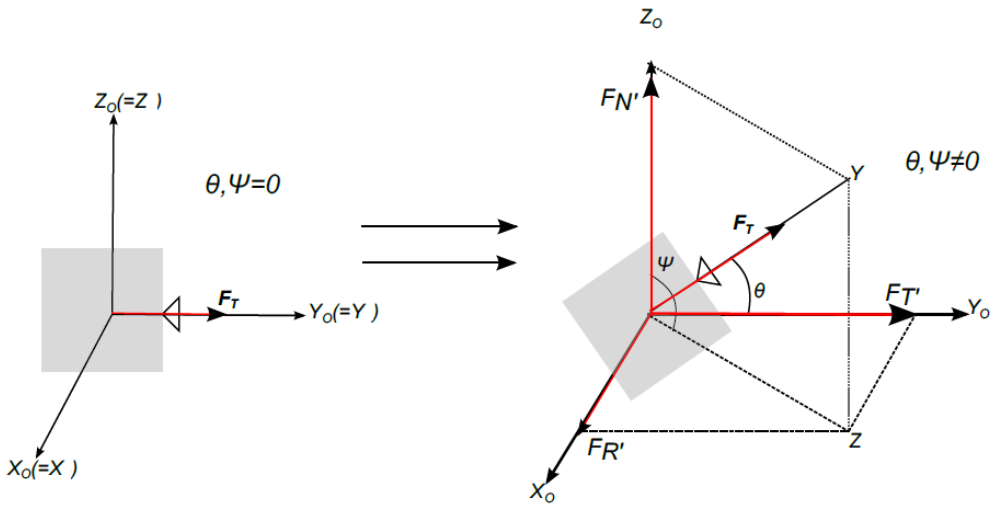

Figure 45: Effect of thrust vector misalignment

$$\begin{bmatrix} F_{R'} \\ F_{T'} \\ F_{N'} \end{bmatrix} = \begin{bmatrix} F_T sin(\theta) cos(\psi) \\ F_T cos(\theta) cos(\psi) \\ F_T cos(\theta) \end{bmatrix} \tag{5.2.6}$$

The perturbing accelerations are introduced in the previous equations to be integrated as:

$$\begin{bmatrix} a_{pR} \\ a_{pT} \\ a_{pN} \end{bmatrix} = \begin{bmatrix} F_{R'}/m(t) \\ F_{T'}/m(t) \\ F_{N'}/m(t) \end{bmatrix} \tag{5.2.7}$$

$\theta, \psi$are assumed to remain constant.

We see the effect of thrust-beam misalignment and what effects it will have on the orbital elements. That is, an analysis is carried out to see how severely the orbital parameters are changing when there are perturbing accelerations only due to off-tangential components of the thrust vector. The effect of these perturbing accelerations are studied for both drag compensation and deorbiting firing times. The result of this analysis will basically be the requirement of attitude knowledge. That is, the thrust-beam misalignment analysis is equivalent to studying and finding pitch and yaw deviations from perfect attitude (body frame is perfectly aligned with the orbit reference frame). The equations 5.2.1to 5.2.5 are integrated using the Runge-Kutta 4th order method, and the results are then com-

pared with SATSLab. Based on both thruster firing periods, we find the θ, ψangles up to which deviation of the orbital elements is sufficiently low and acceptable. These angles are then fixed as the necessary angles up to which attitude knowledge is sufficient. As a preliminary definition, it is also assumed that the same attitude knowledge will be required for the roll(ϕ)axis. This attitude knowledge will be required before the thruster firing commences, and the attitude control system will work to bring the microsatellite back towards the acceptable attitude range.

First the equations 5.2.1 to 5.2.5are integrated when $\theta = \psi = 0 \pm 180$ degrees:

parameter	initial value
a	6878 (h=400 km)
e	≈ 0
i	98 degrees
Ω	0
ω	28 degrees
F_T	9e-3 N
m	40 kg

The simulation time is taken to be 15 minutes,and no other disturbing accelerations are assumed to act on the D3SAT.

Parameter	**Analytical**	**SATSLab**
$\Delta \boldsymbol{a}(\boldsymbol{meters})$	±341.5	±341.807
$\Delta \boldsymbol{e}$	0	0
$\Delta \boldsymbol{i}$	0	0

Table 15: Thrust beam misalignment results:$\theta, \psi = 0 \pm 180°$

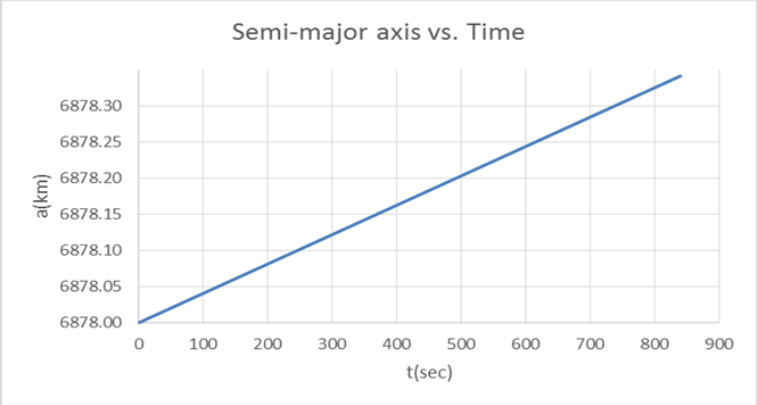

Figure 46: Thrust beam misalignment results:$\theta, \psi = 0 \pm 180°$

As expected, the semi-major axis increases when thrust vector is perfectly aligned in the tangential direction. The eccentricity and the inclination do not change. To verify correct integration of the equations , we compare the analytical results with SATSLab results.

Then, the equations 5.2.1 to 5.2.5are integrated when $\theta = \psi = \pm 5°$

Parameter	Analytical	SATSLab
$\Delta a(meters)$	±338.85	±339.223
Δe	-3e-7	0
Δi	0	0

Table 16: Thrust beam misalignment results:$\theta, \psi = \pm 5°$

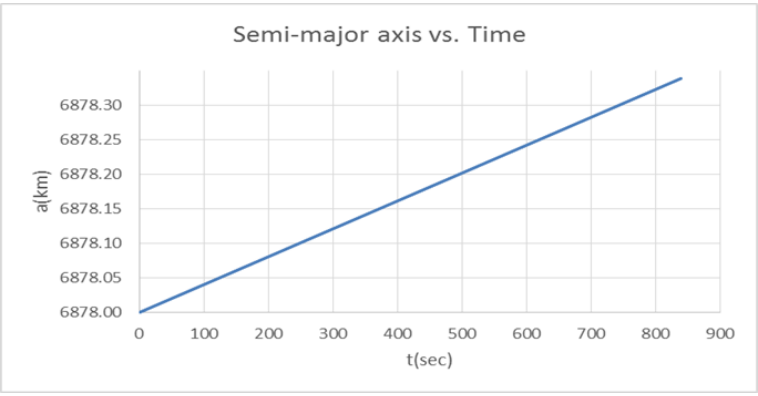

Figure 47: Thrust beam misalignment results:$\theta, \psi = \pm 5°$

Therefore, thrust is less efficient when thrust vector is not exactly along tangential direction. However even with misalignment of ±5degrees, the main deviation is in the semi-major axis from the nominal semi-major axis when the attitude deviation is zero, which is 2.64 m at the end of the firing time from analytical results and 2.57 m from SATSLab.

The above procedure is repeated for varying yaw and pitch deviations, and also a longer firing time of 60 minutes is analyzed, since the maximum firing time in one ignition is in the case of deorbiting, as seen in section 4.3. The below figure shows the deviation in semi-major axis due to deviation from perfect attitude. It is also assumed that no other perturbing accelerations act on the D3SAT.

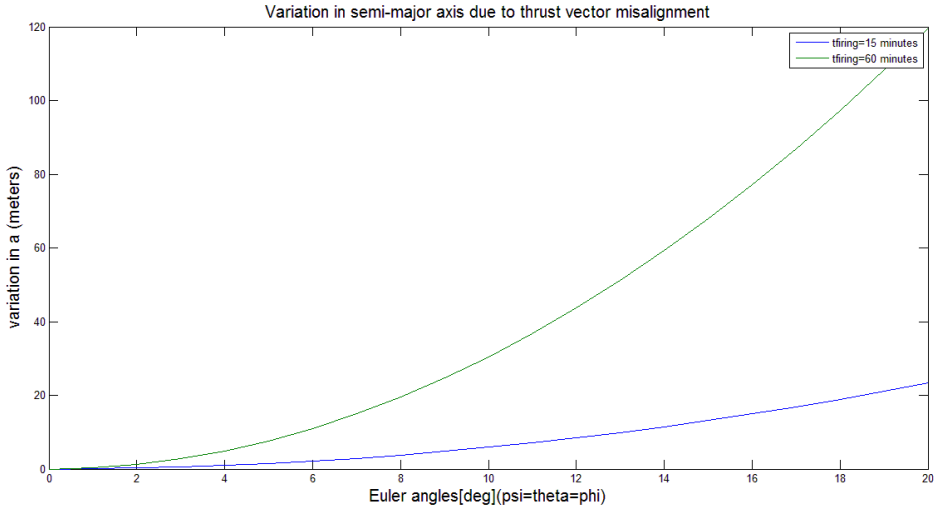

Figure 48: Variation of semi-major axis over firing period due to thrust beam misalignment

We see from the figure above that in the case of continuous firing for 60 minutes,the semi-major axis will show a difference of nearly 20m (with respect to the case when BF frame is perfectly aligned with RTN frame) when the misalignment is 5° . Therefore in order to keep variation of semi-major axis under an acceptable value, we conclude that required attitude knowledge of ±5° along each axis is required. That is, attitude knowledge in the range of 0 to 5 degrees is acceptable for the D3SAT mission.

5.2.4 HT-firing requirement

When the HT-100D is firing, we want to make sure that the device chosen to measure the angular rate of the D3SAT will have a drift rate low enough such that during the firing period, the required attitude knowledge of ±5°can be obtained. The HT-firing mode will consist of analyzing the two firing times related to drag compensation and deorbiting.

$$Drift \times t_{firing} \leq 5^{\circ}$$

We will add 20 % extra to the firing time to be on the safe side.

5.2.4.1 Drag compensation

1)For reference case 1 from section 4.2.4: $t_{firing}(minutes) = 6$

$$\therefore Drift \leq 0.0115^{\circ}/sec$$

2)For reference case 2 from section4.2.5: $t_{firing}(minutes) = 19$

$$\therefore Drift \leq 3.6549e-3^{\circ}/sec$$

5.2.4.2 Deorbiting

From section 4.3.2,$t_{firing}(minutes) = 55$

$$\therefore Drift \leq 1.286e-3^{\circ}/sec$$

The most stringent requirement for choosing the angular rate measurement device comes from the deorbiting phase, during which the firing time in one ignition will be maximum. Therefore, the choice of our measurement device should be made keeping in mind that the drift rate should be less than $1.286e-3^{\circ}/sec$.

5.2.5 Slew requirement

The objective of Slew mode is to rotate the satellite so that the antenna points towards ground station when a ground pass is approaching. This dictates the rate at which the satellite bus will have to rotate, and the angular rate which it will have to maintain during a ground pass. The worst case scenario is the one in which the X+ face containing the antenna will have to slew 180° during an overflight.

From the figure below, the maximum arch section of the orbit visible from a ground station can be calculated as :

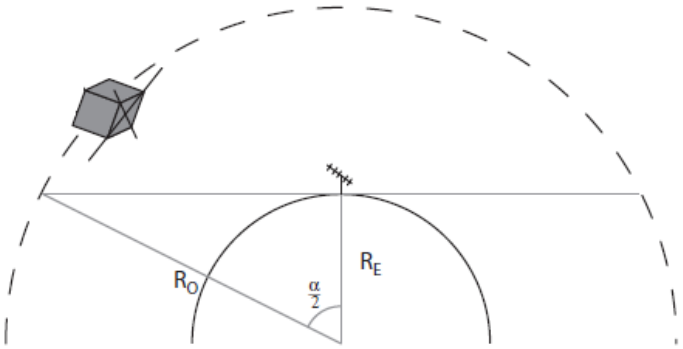

Figure 49: Ground Station visibility arc

$$\alpha = 2cos^{-1}(\frac{R_E}{R_O})$$

At an altitude of 350 km,$\alpha = 37°$.

Therefore, from [39] we can calculate maximum time in view as :

$$T_{vis} = \frac{\alpha}{2\pi} T_{period} = 560sec$$

This yields a minimum angular velocity of the satellite as:

$$\omega_{min} = \frac{\pi}{560} = 0.32°/sec$$

The D3SAT should be able to maintain an angular velocity of minimum $0.32°/sec$ during an overflight to ensure a stable communication link.

5.3 Summary

REQ A	Detumbling	$\leq 3\ orbits\ after\ release\ from\ launcher$
REQ B	Final angular rate at the end of detumbling	$< 0.05°/sec$
REQ C	Initial attitude acquisition	$< 60\ minutes\ after\ detumbling$
REQ D	Drift rate of angular rate measurement device	$\leq 1.286e-3°/sec$
REQ E	Attitude knowledge	$\pm 5° along\ each\ axis$
REQ F	Pointing rate	$> 0.3°/sec$

Table 17: ADCS requirements

Chapter 6

Attitude Estimation

Obtaining accurate attitude information is crucial to any space mission. Without reliable estimates of the spacecraft attitude, the ability to control the spacecraft, transmit data to the ground station, or meet other mission objectives may be jeopardized. Sensor information is generally combined in an attitude determination system to provide the best possible estimates at all times. Depending on the requirements of the mission, the attitude determination may be performed in real-time on-board, or carried out on the ground station in batches based on data down-linked from the spacecraft. Attitude determination systems are a diverse field, but fundamentally they all require a measurement system that includes sufficient sensors to enable that attitude information is extracted with the necessary accuracy.

6.1 Common Attitude Sensors

There are two basic classes of attitude sensors. The first class makes absolute measurements, whereas the second class makes relative measurements. Absolute measurement sensors are based on the fact that knowing the position of a spacecraft in its orbit makes it possible to compute the vector directions, with respect to an inertial frame, of certain astronomical objects, or of the force lines of the Earth's magnetic field. Absolute measurement sensors measure these directions with respect to a spacecraft or body-fixed reference frame, and by comparing the measurements with the known reference directions in an inertial reference frame, are able to approximately determine the relative orientation of the body frame with respect to the inertial frame.

Relative measurement sensors belong to the class of gyroscopic instruments, including the rate gyro and the integrating gyro.To perform attitude determination, five common sensors for spacecraft are considered: sun sensors, magnetometers, horizon crossing indicators, star trackers, and inertial measurement units. Each option is discussed individually.

1) Sun sensors

The Sun provides a well-defined reference vector. Sun sensors are visible light detectors, which measure one or two angles between their mounting base and incident sunlight. Sensors range from analog presence detectors to digital instruments which measure the sun direction to an accuracy down to one arc-minute. Sun sensors are popular, accurate and reliable, but require clear fields of view. Since most low-Earth orbits include eclipse periods, the attitude determination system must provide some way of handling the regular loss of Sun reference. Typical sun sensor accuracy range from 0.005 deg. to 4 deg[50].

2) Magnetometers

Magnetometers measure the Earth's magnetic field vector local to the spacecraft. Most magnetometers come as a three-axis package that outputs three orthogonal components of the magnetic field, Accuracy is usually limited by spacecraft noise and data is good even at high rotation rates, provided that the sampling frequency is high enough. However, only two directions of attitude can be determined at any given point in time (all but the rotation about the field magnitude), and hence they must be used in conjunction with other sensors.

3) Earth sensors

Horizon sensors,or earth sensors are infrared devices that detect the contrast in temperature between space and the Earth's atmosphere. Some nadir-pointing spacecrafts use a wide field-of-view fixed head sensor, which views the entire Earth disk and centers the spacecraft on it. The direct Earth-relative information obtained from Horizon sensors may simplify on-board processing on Earth pointing spacecraft. Typical accuracies for systems using horizon sensors are 0.1 to 0.25 deg., with some applications approaching 0.03 deg[39].

4) Star sensors

A star camera measures the elevation of the line of sight to a star as projected onto mutually perpendicular planes which contain the sensor boresight axis. The locations of two or more stars on the sensor, along with their locations in inertial coordinates are sufficient to determine the attitude of the camera with respect

to an inertial frame of reference. The star camera is generally sensitive to large angular velocities of the spacecraft as this causes a smearing of the star images on the sensor. The star tracker is, so heavy and big, especially the baffle needed to shield the sensor from sun, earth, and moon shine, that it is unfeasible for this mission.

5) Inertial Measurement Unit(belongs to class of absolute measurements)

An inertial measurement unit (IMU) is an electronic device that measures and reports a craft's velocity, orientation, and gravitational forces, using a combination of accelerometers and gyroscopes. The sensors are subject to random drift and bias errors, and as a result, the errors are not bounded. In order to provide an absolute attitude, regular updates are performed, based on references such as the Sun, stars, or the Earth. Traditional inertial reference units are mounted in a multi axis gimbal assembly. While accurate, gimballed units are mechanically complex, heavy, and use more power than the increasingly popular strap-down units. Strap-down units are typically composed of an orthogonal three-axis set of inertial angular rate sensors and accelerometers. The inertial sensors are directly mounted (strap-down) to the spacecraft structure. A number of new solidstate concepts have become available in recent years, such as fiber optic and piezo electric quartz gyros[12], resulting in decreased size, weight, and cost. Gyros typically have a drift rate of down to 0.002 deg./hour[39, 50].

6.2 Sensor selection

6.2.1 Magnetometer

Since our microsatellite will be orbiting in LEO, we can make use of Earth's magnetic field to obtain attitude information. Hence we choose a 3-axis magnetometer, which measures the geomagnetic field in body coordinates which is compared to a reference model of the Earth's magnetic field, using the position of the spacecraft, for attitude determination. Although the TAM provides three scalar measurements, only two directions of attitude can be determined at any given point in time (all but the rotation about the field magnitude). These attitude sensors have many advantages including:

1) TAMs are relatively inexpensive and reliable

2) The Earth's magnetic field is always in the field-of-view

3) three-axis attitude determination is possible with some knowledge of the spacecraft dynamics

The Earth's magnetic field is a vector quantity. The quantities that completely define the magnetic field vector,adapted from , are given by[51]:

-Declination (the difference between true north and magnetic north) (D). D is positive if magnetic north is east of true north.

-The horizontal intensity of the field (H).

-Inclination or dip, the angle the field vector makes with the horizontal, positive below the horizontal (I).

-The north component of the field (X).

-The east component of the field (Y).

-The vertical component of the field (positive downwards) (Z).

-The total intensity of the field (F)

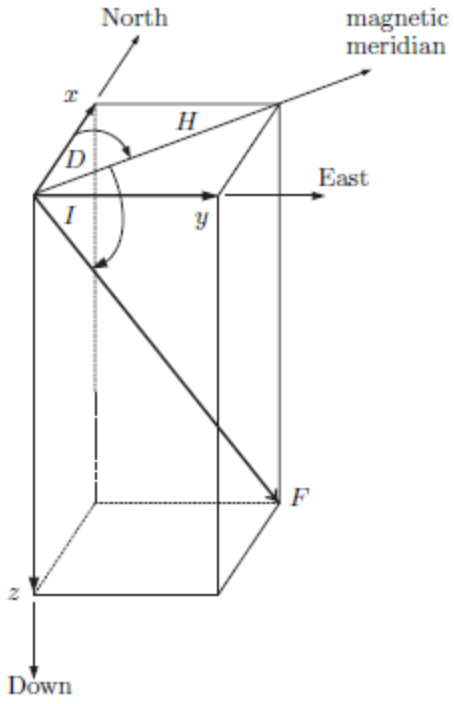

Figure 50: Earth magnetic field description

For our application, the geocentric inertial components are required as opposed to the local tangential coordinates. This transformation is given in [51] as:

$$B_x = (B_r cos\delta + B_\theta sin\delta)cos\alpha - B_\phi sin\alpha$$

$$B_y = (B_r cos\delta + B_\theta sin\delta)sin\alpha + B_\phi cos\alpha$$

$$B_z = (B_r sin\delta - B_\theta cos\delta)$$

B_r is the radial component measured outward positive, B_θ is the co-elevation measured south positive, and B_ϕ is the azimuthal component measured east positive. Hence we can see that the magnetic field is a function of both declination δ and right ascension α.

There are various methods to gain knowledge of the real magnetic field of the Earth. One way of doing this is by using a look-up table. This approach would require data uploaded from ground in order for it not to be too extensive for the storage capacity on-board. However, due to uncertainties of the magnetic field in terms of magnitude, direction as well as with the microsatellites location and altitude, as well as varying with time, a stand-alone lookup table uploaded on the computer will not be satisfactory. Another option would be to upload a smaller look-up table, and keep updating it as ground communication becomes possible. Although this would ease the work of the OBC, this would require continuous communication with the ground station, and this might cause a failure in estimating the attitude in the event of a communication failure. For this reason ,we choose to make use of a magnetic reference model. With the knowledge of the magnetometer measurements, and by comparing it the magnetic reference field model, we can get information about the attitude. Magnetic reference field models provide an easy way to calculate magnetic declination and other components of the magnetic field. These models are mathematical algorithms whose parameters are based on an analysis of magnetic monitoring satellites either over the entire world or a part of the world. Spherical harmonic analysis is the most common method used for producing global models [8]. The International Geomagnetic Reference Field (IGRF) and the World Magnetic Model (WMM) are the most commonly used models for navigational purposes. Models are traditionally updated every five years.

The International Geomagnetic Reference Field (IGRF) is a global model of the geomagnetic field surrounding the Earth, and it is updated every five years by the International Association of Geomagnetism and Aeronomy (IAGA). It consists of a set of Gaussian coefficients that is used to create a spherical harmonical

approximation of the field.It is a standard mathematical description of the Earth's main magnetic field and its secular variation. It is the product of a collaborative effort between magnetic field modelers and the institutes involved in collecting and analysing magnetic field data from satellites and from observatories around the world. The internal part of the geomagnetic field, which is almost entirely core generated, undergoes slow, but noticeable, changes on timescales of years to decades. Consequently the IGRF must be revised, typically every five years, to remain up to date and as accurate as possible[52]. The IGRF models also include a set of secular variation terms that are valid for five years after the model epoch.

We choose the IGRF model, because it is the most commonly used.The error becomes smaller the better the model being used is, hence the IGRF model will give better results than using a simple dipole model. Errors in the estimate of the satellite position will also induce errors as the measurement is compared to the magnetic field at another position.In order to visualize how the total intensity of the magnetic field varies with position, and also to visualize the predicted rate of change till the year 2020, we see the below figure.The values are derived from the 12th Generation IGRF model.

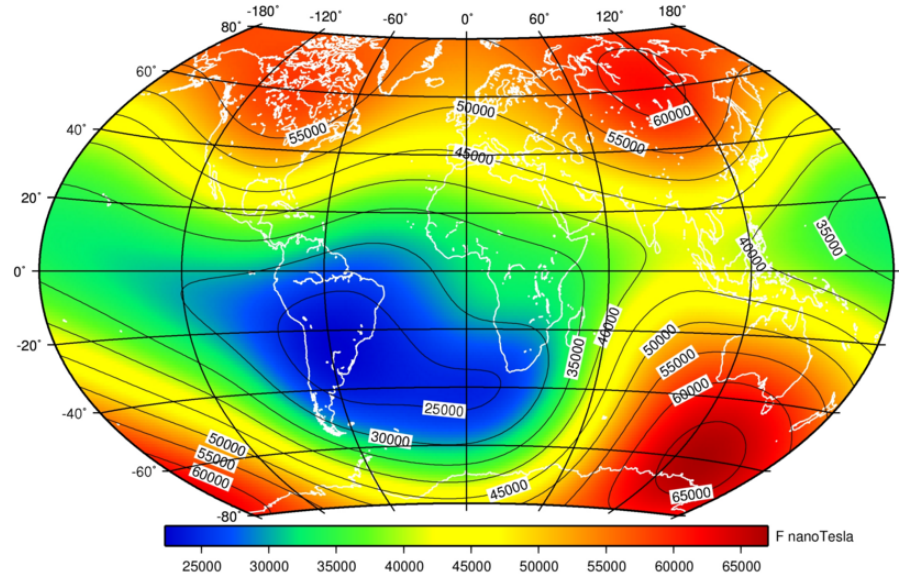

(a) Map of total intensity at 2015

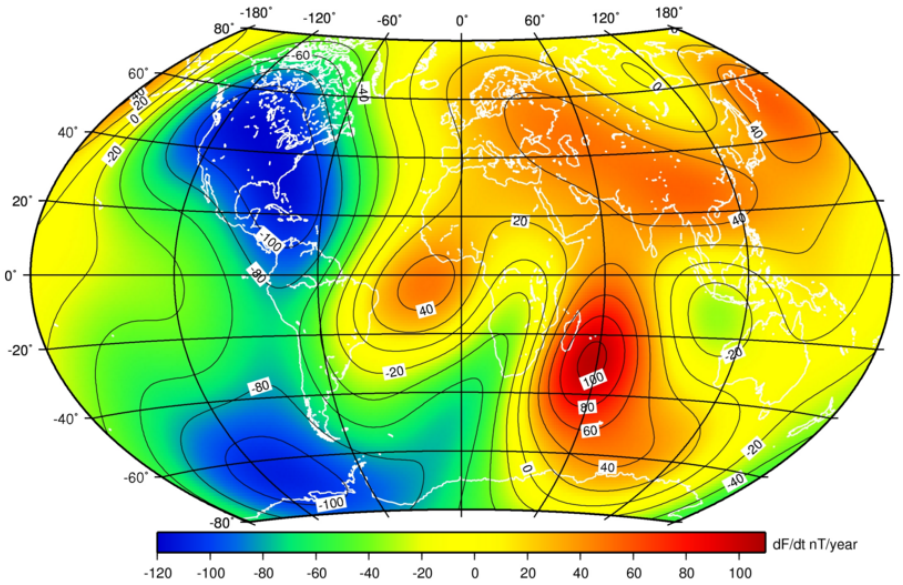

(b) Map of predicted annual rate of change of total intensity for 2015-2020

Figure 51: IGRF model:12th generation(Source:[8])

The magnetometer chosen is the 3-axis fluxgate magnetometer from Surrey Satellite Technology Limited[53]. This magnetometer measures the magnetic field and provides readings from 3 sensors arranged in orthogonal axes. It can be used in combination with a satellite position fix and the IGRF model to determine satellite attitude.Also provided is an analogue temperature sensor which provides the case-temperature telemetry.

Mass(kg)	Power(W)	Dimensions
0.19	0.3	$81.5mm \times 32mm \times 47mm$

Figure 52: Magnetometer,SSTL specifications

6.2.2 GPS

The magnetometer measurements need to be compared to the IGRF model in order to determine attitude of the microsatellite. As we have seen before, the magnetic field is dependent on the right ascension and declination. Hence, if position of satellite is known, coordinates of the IGRF model can be obtained and thus compared to the field measured by the magnetometer. This is done using GPS, since our microsatellite will be in Low Earth orbit, and therefore, will have very good visibility of GPS satellites[54].

The Global Positioning System (GPS) is a satellite navigation system for determining position, velocity and time with high accuracy. The GPS system allows a GPS receiver to determine its position and time at any place using data from at least: three satellites (for 2D positioning) and four satellites(for 3D positioning)[55]. In addition, the on-board GPS receiver can also be used for the following functions:

1) Real time orbit tracking: the receiver can be used for knowledge (and active control) during launch and orbital insertion, and also for near-real time knowledge for orbit maintenance and for rapid post -maneuver orbit recovery.

2) The GPS receiver can also provide accurate reference time synchronized to UTC better than $1\mu s$[56].

GPS Space Segment: The nominal GPS satellite constellation consists of 24 space vehicles distributed in six orbital planes with an inclination of 55 degrees in relation to the equator.They orbit the earth twice a day at an altitude of 20,200 km.

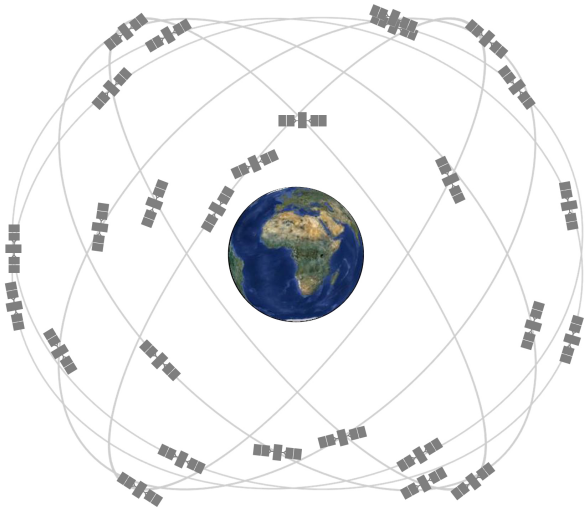

Figure 53: GPS Space Segment

GPS User Segment: This refers to the GPS receiver on-board the microsatellite. The GPS receiver must be locked on to at least 3 GPS satellites to calculate latitude and longitude, by a process called triangulation which is shown in the figure below.

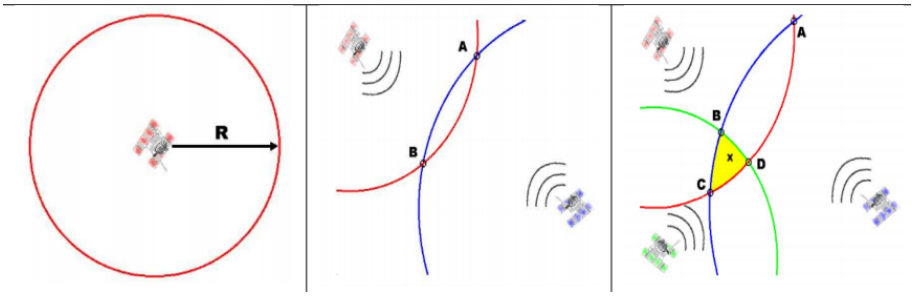

Figure 54: GPS receiver operating principle

The receiver compares the time at which a signal was transmitted from a GPS satellite to the time at which the signal was received, and it is this time difference which gives us the distance of the GPS receiver to the GPS satellite. When signals from 4 or more GPS satellites are used, the receiver can determine altitude in addition to latitude and longitude, thus giving a complete 3-D position. Once the position of the receiver has been determined,the GPS unit can calculate velocity and orbit track.The signals sent by the GPS satellites essentially contain almanac data, which contains satellite orbit information and allows the GPS receiver to predict which satellites are in view, thereby shortening acquisition time. The re-

ceiver must have a continuous fix for approximately 15 minutes to receive a complete almanac from the satellites.Ephemeris data contains precision corrections to the almanac data and is required for accurate positioning. It is continuously updated and therefore the ephemeris data is considered valid only for about 30 minutes[57].

An important parameter for the GPS receiver which measures its efficiency is Time To First FIX(TTFF). This depends on the start-up mode of the receiver:

1)Cold Start: This mode means that the receiver has been started after moving about 100 km from its initial position.In this state, the GPS receiver does not have a current almanac,ephemeris, initial position or time.In this mode, it can take up to one hour to get position information[55]. Also, the GPS receiver can make miscalculations regarding which GPS satellites to use.

2)Warm Start: This mode means that the currently store almanac,initial position and time are valid, the only uncertainty being ephemeris data which can be partially valid or invalid.TTFF is approximately 30 seconds to 2 minutes[56].

3) Hot Start: If the GPS receiver has been off for less than an hour, it has valid time, position, almanac, and ephemeris data, enabling a rapid acquisition of satellite signals.TTFF in this case is from 5-20 seconds[56, 58].

The GPS receiver selection was based primarily on the basis of accuracy of orbital position information.To evaluate the efficiency of the HT-100D for drag compensation (refer to section 4.2.4), the orbital position needs to be acquired with a reasonable accuracy. The SGR-05P Space GPS receiver[59] from Surrey Satellite Technology Limited was found to provide orbital position with an accuracy up to 20 meters. Also, the almanacs and orbital elements are are stored in flash memory to enable a worst case TTFF of 180 seconds. Since the time between firings for strategy 1 of drag compensation is 3 hours, this TTTF is more than sufficient. The SGR-05P also comes with a small patch antenna to receive signals from the GPS satellites.

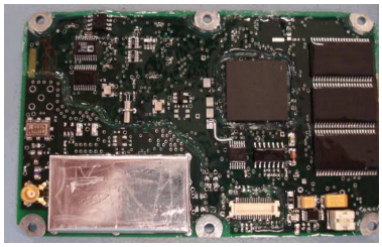

Component	Mass(kg)	Power(W)	Dimensions
Receiver	0.06	1	$100mm \times 65mm \times 12mm$
Patch Antenna	0.05		$45mm \times 45 \times 20mm$

Figure 55: SGR-05P Space GPS receiver,SSTL specifications

6.2.3 Inertial Measurement Unit

Only magnetometers cannot be used for attitude determination due to the following reasons:

Magnetometers are inherently nonlinear devices and an accurate in-flight calibration of the magnetometer is required to get to the specified accuracy. The magnetic disturbances within the D3SAT can corrupt the readings of the magnetometer. Accurate timing of the measurements is needed in order to correlate the measurements and the reference field vectors. Perturbations to the main field may vary in magnitude from fractions of a nT to thousands of nT, and this inaccuracy in the knowledge of the Earth's field model easily produces errors of 0.4 deg about each axis[60]. Furthermore the complexity of spherical harmonics models of the Earth's magnetic field as well as the complexity of the attitude estimation algorithm prevents the use of attitude estimation using only magnetometers.

To completely determine 3-D attitude, we need to incorporate some knowledge of the spacecraft dynamics, which can be done by using inertial sensors. which can be acquired by using accelerometer measurements. Accelerometers measure inertial force, such a force can be caused by gravitation, but it might also be caused by acceleration of the device. As a result even if accelerometer is in a relatively stable state, it is still very sensitive to vibration and mechanical noise in general. This is the main reason why a gyroscope is needed to smooth out any accelerometer errors.The gyroscope is not free from noise however because even though it is less sensitive to linear mechanical movements, gyroscopes have other types of problems, like drift (not coming back to zero-rate value when rotation stops). By averaging data that comes from accelerometer and gyroscope we can obtain a relatively better attitude estimate than we would obtain by using the accelerometer

data alone. This is precisely what Inertial Measurement Units are. IMUs combine 3-axis gyroscope with a 3-axis accelerometer, and along with magnetometer measurements, complete and reliable 3-D attitude information can be determined, that too at low cost and low power consumption. The choice of the inertial measurement unit is based on REQ D from table 17. Another constraint for selecting the IMU is that the gyro range should be at least ±8 deg/sec since upon release from launcher , the angular rate will be ±8.5°/sec along each axis.(from section 5.2.1). The STIM300 Inertial Measurement Unit from Sensonor [61] is a cost effective ITAR free solution. The typical gyro range offered is ±400°/sec. A lower range can be requested for reducing the cost.

Mass(kg)	Power(W)	Gyro Bias Instability (°/sec)	Dimensions
0.05	1.5	2e-6	$44.8mm \times 38.6mm \times 35.9mm$

Figure 56: STIM300,Sensonor specifications

Another option which was found was the 3DM-GX1 from LORD MicroStrain [62], which combines the 3-axis angular rate gyros, three orthogonal DC accelerometers and three orthogonal magnetometers. This can be used in conjunction with the SGR-05P.

Mass(kg)	Power(W)	Dimensions
0.074	0.78	$64mm \times 90mm \times 25mm$

Figure 57: 3DM-GX1,LORD MicroStrain specifications

If we use the above mentioned configuration for the attitude estimation subsystem, we will reduce the power consumption by 0.2 W and mass by about 0.17 kg. However, the 3DM-GX1 has not been used for space applications.Therefore we decide on the use of the STIM300,SGR-05P and Magnetometer configuration. However, for future work, attention can be focused on trying to use the 3DM-GX1 along with the SGR-05P. Both options can provide a gyro range > 8deg/sec.

6.2.4 Sun Sensor

From section 5.2.2, after detumbling, and before the solar panels are deployed, we will need the attitude information with respect to an inertial frame of reference. This can be done with the 3-axis magnetometer. However, this will require some power, and as mentioned before, due to inaccuracies in the Earth magnetic field readings, this attitude information might not be accurate. Hence we considering placing an optical sensor on the D3SAT. We compare different optical sensors[63] in the table below:

Sensor	Advantages	Disadvantages
Star sensor	- Very accurate	-high cost -high mass and power consumption
Sun sensor	-low mass -small size	-Orbit dependent(eclipse)
Earth sensor	-Earth is always visible -Reliable and cheap	-Higher power consumption due to use of infrared camera

Table 18: Comparision of optical sensors

From the point of view of power consumption, a sun sensor is the obvious choice. In addition, it can be used for sun-pointing to orient the solar panels towards the sun. Since the sun sensor is primarily used for initial attitude acquisition, it does not warrant the choice of analog fine sun sensors and digital fine sun sensors. Therefore coarse sun sensor is decided upon. A coarse sun-sensor can be used to detect the direction to the Sun by monitoring the output current. The output from a solar cell is mostly dependent on the sunlight angle of incidence with the cell and the intensity of the inbound light. When measuring the output to determine the variables producing it, current sensors are usually chosen over voltage sensors because variations in current output of the solar panels are more responsive to the incidence angle of a light source. The most commonly used sun sensor is the flat sun sensor.

Flat sun sensor(FSS)

Typical configuration includes photovoltaic cells located on all spacecraft faces.The energy per area (which generates a voltage and current) on the PV cell proportional to the cosine of the angle of incidence of the incoming light. If the PV cell were rotated around its unit normal, the angle will not change and therefore the voltage and current generated by the incoming light will not change.

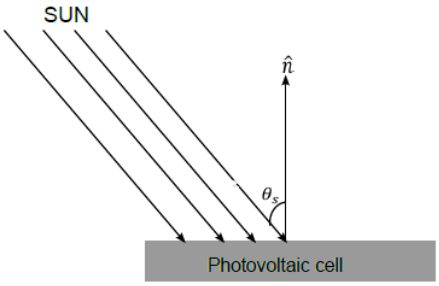

Figure 58: Flat sun sensor

We cannot place these photovoltaic cells on Y- face which contains the thruster and either on the Z- face(attachment to launcher). We can place a cell on the Y+ face but this will be shadowed during normal operation, when the solar panels are deployed. We can also place a cell on the X+ face and the X- face and on the Z+ face. The only thing that can be done with this configuration is placing it on the above faces. This can be sufficient for initial attitude acquisition. However, due to the photovoltaic cells being small, there is a possibility that they will not work sufficiently well because of shadowing by the GPS antenna on the Z+ face and by the telecommunications antenna on the X+ face.In addition, the FOV of the sensor is limited to only that light which is in front of the cell ($\theta_s < 90°$).That is, the FSS loses sensitivity when the sun vector approaches normal direction of the cell. This configuration is highly sensitive to Earth albedo.The OBC will have to store information about Earth albedo as a function of time and this will lead to increased load on the OBC. If the sun hits a face directly, while Earth albedo hits the opposite face very directly, the Earth- pointing face may face a stronger illumination, and this will give a 'wrong side' reading[64].One sensor can only able give one angle to the Sun. Atleast two flat sun sensors have to be simultaneously in FOV of the sun for bi-axis information .

To eliminate the above disadvantages we explore the use of pyramidal sun sensors(PSS).

Pyramidal sun sensor(PSS)

The incoming sunlight will generate voltages and currents on the two PV cells proportional to the angle of incidence of the light with respect to the unit normals of the PV cells By differencing the two voltages (or currents), and because the geometry of the two cell system is known, it is possible to determine where the Sun lies along the X-axis As the Sun moves toward the boresight, the angle of

incidence of incoming light becomes the same for the two cells and the voltage generated on each PV cell becomes the same. When the Sun is at the system boresight, the voltages will cancel when differenced, and the result will be a zero value for the Sun along the X-axis.

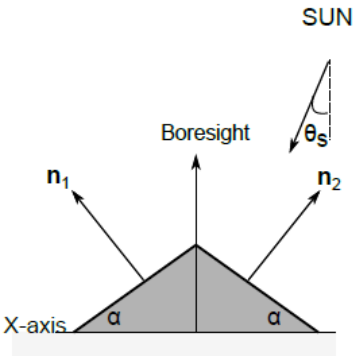

Figure 59: Single axis pyramidal sun sensor

Conceptually extending the two PV cell system to a four PV cell system is simple. Imagine the X-axis and the boresight vector in the above figure are part of a triad whose third member, the Y-axis, is generated by the right-hand rule. Imagine that the Y-axis also has a two PV cell system oriented such that the four cells create a pyramid of PV cells. Light from the Sun illuminates the PV cells located on of each of the four sides of the pyramid at some angle of incidence, causing a voltage to be generated at each cell based on the angle of incidence. By simply differencing the signals from the PV cells on opposite faces of the pyramid, a coarse direction to the sun is obtained.

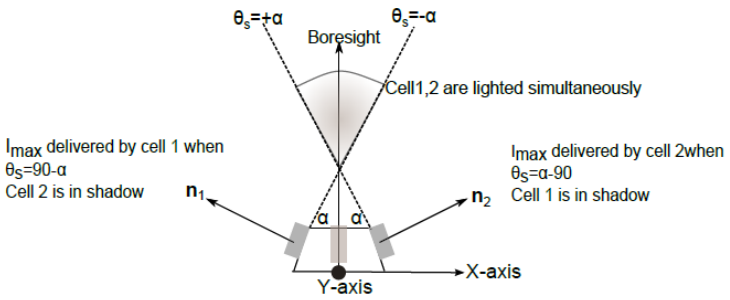

Figure 60: Bi-axis pyramidal sun sensor

These sensors eliminate all the drawbacks of the FSS.The FOV overlaps if used

in conjunction with other cells.Also, this configuration is less sensitive to albedo since baffles are generally used for pyramidal sun sensors. From section 1.3, we see the faces available for placing the PSS.

It cannot be attached on the Z- face because this face will be attached to the launcher.the X- face will contain the stowed solar panels.The Y+ face, will contain another stowed solar panel area .Therefore the candidate faces for placing the PSS are X+,Y- and Z+. We choose to place a PSS on the Z+ face (top face). If we use only one at Z+ face, assuming that after detumbling angular rate is $0.05°/sec$ (from REQ B in table 17), the worst case waiting time till the sun is in FOV of the PSS will be 60 minutes(assuming the Z+ face will have to rotate 180°). This violates REQ C from table 17.Therefore we choose to place another one on the Y- face .

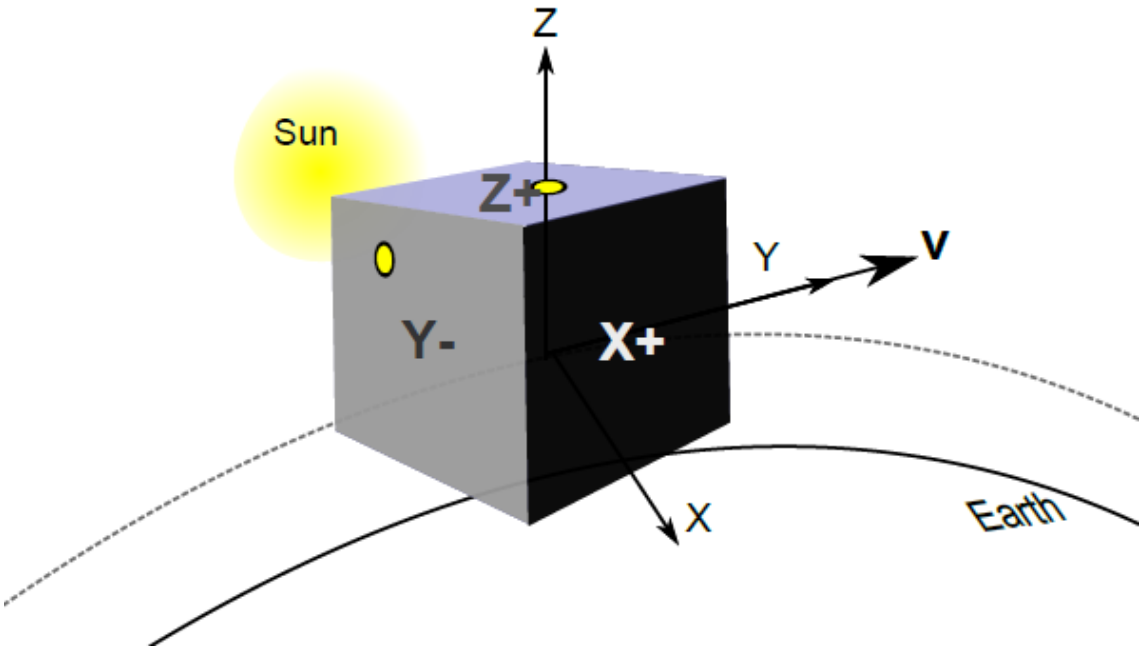

Figure 61: Sun sensor placement

The construction of a PSS is relatively simple,and it is recommended to manufacture in-house.However, in this thesis, we choose the BASS 17 from EADS Astrium[65].

Mass(kg)	Power(W)	Dimensions
0.065	None(passive equipment)	$70mm \times 82mm \times 23mm$

Figure 62: BASS 17,EADS Astrium specifications

6.3 Attitude Determination Algorithm

The pertinent combinations of inertial and magnetic sensor measurements involve the selection of an algorithm to devise an attitude estimation method.We need the D3SAT orientation and rotational velocity with respect to a known reference frame, which in our case is the RTN Frame. The sensor measurements are incorporated in an attitude determination algorithm, from where orientation and rotational velocity of the satellite can be determined, an attitude determination algorithm is used. Incorporating these vector components in suitable algorithms, the orientation and rotational velocity of the satellite can be estimated. Three attitude determination algorithms are discussed in this section.

According to the number of the involved sensors, attitude estimation methods in the literature can be cast into two groups. The first group makes use of two sensors, typically a magnetometer and an accelerometer, and includes deterministic methods. To find the attitude matrix, a classical least squares approach to the problem, as introduced by [66], is in general considered. These deterministic methods assume that all movements are quasi-static, and therefore this means that they are not taking into consideration the external accelerations. In such cases, it becomes difficult to retrieve the attitude with high accuracy since it is not straightforward to dissociate external accelerations and the gravity. Therefore, deterministic methods are often only used as a backup.

TRIAD

The Triad algorithm determines the orientation of the satellite. A triad is a set of three linear independent unit vectors that can define a coordinate system. Two

measurement vectors and their corresponding modeled vectors are used to form two orthonormal triads. These triads can then be used to construct the transformation matrix from the RTN frame to the BF frame[67]. From this matrix the satellite orientation in quaternions or Euler angles can be calculated .

The second group of methods,which are recursive estimators, are more convenient since they do not require storage of past information and allow real-time processing of new incoming information. These estimators combine readings from gyroscopes, accelerometers, and magnetometers.consists of classical filtering methods, some of which are described below: using either Kalman filters (KFs), extended Kalman filters (EKFs), or nonlinear observers. The attitude estimation in these works is affected also by errors in dynamic situation, characterized by external acceleration.

Discrete Kalmann Filter

This filtering method allows estimation of past,present and future states of a system which is acted upon by a stochastic noise.Kalman filters are based on linear dynamical systems discretised in the time domain, where the state of the system is represented as a vector of real numbers.At each time update, a linear operator is applied to the state, thus resulting in the new state (with some added noise).Also, perturbations and controls applied to the system can be added.The Kalman filter estimates a process state at some time and collects feedback in the form of measurements.

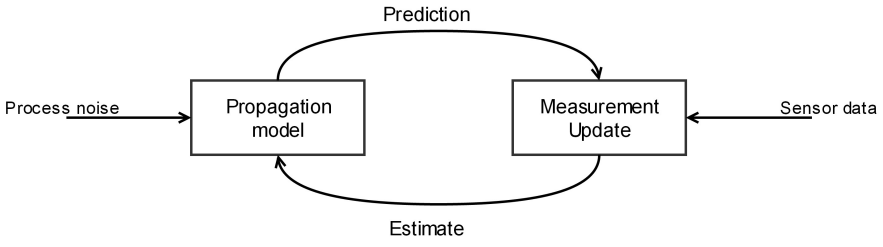

Figure 63: Kalmann filter schematic

This method has average estimation errors, and thus is suitable for use only during tumbling phase of the microsatellite.

Extended Kalman Filter

The above mentioned discrete Kalman filter is restricted to a linear assumption, which is a limiting constraint.The extended Kalman filter (EKF) is the nonlinear version of the Kalman filter which linearizes about an estimate of the current mean and co-variance[68].This filter uses all valid measurement vectors available, as well as their corresponding RTN frame modeled vectors. The Extended Kalman Filter can be used to determine the full satellite state,that is, the ECI referenced rate vector and satellite's orientation in quaternions.

In this preliminary design phase of the ADCS, the choice of the attitude estimation algorithm is not finalised. Generally speaking, different attitude estimation methods will be employed during different modes of the ADCS and this can be expanded upon in future work.

6.4 Summary

Component	Component name	Manufacturer	Number	Mass(kg)	Power(W)
Magnetometer	3-axis Fluxgate Magnetometer	Surrey Satellite Technology Ltd.	1	0.19	0.3
Inertial Measurement Unit	STIM300	Sensonor	1	0.05	1.5
GPS receiver +antenna	SGR-05P	Surrey Satellite Technology Ltd.	1	0.1	1
Pyramidal Sun Sensor	BASS17	EADS Astrium	2	0.65	-
TOTAL				0.99	2.8

Table 19: Attitude Estimation Subsystem budget

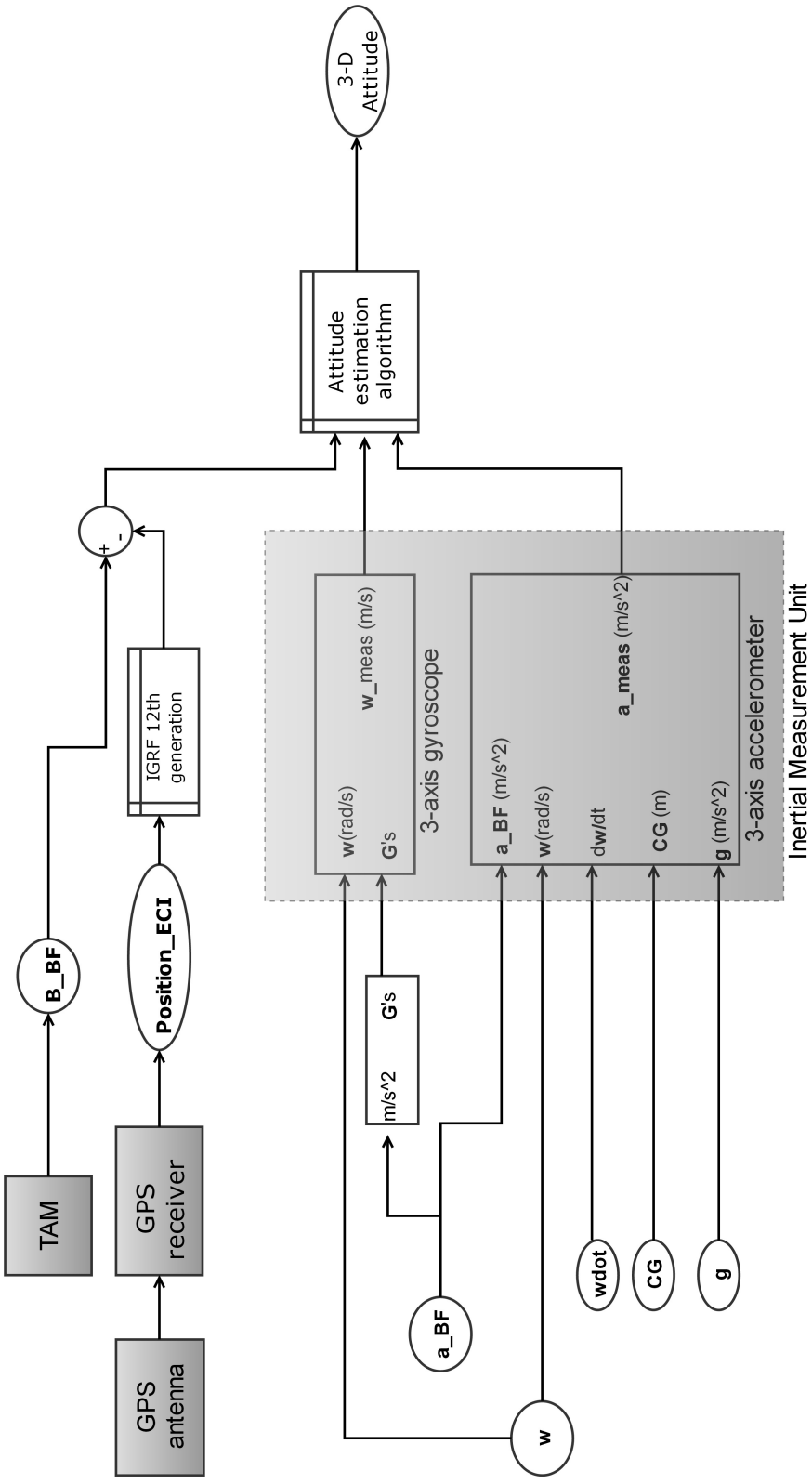

Figure 64: Attitude Estimation Subsystem schematic

Chapter 7

Attitude Control

After determining the attitude of the D3SAT, we will need to change it according to the mission and mode requirements. For example, we may need to compensate for disturbance torques or rotate the spacecraft to point at a new subject. Applying a torque changes a vehicle's attitude, and that is why we need the attitude control subsystem , which consists of actuators and and control system to control these actuators. Actuators provide "torque on demand" to rotate a spacecraft as needed. Just as several different types of sensors often work together to accurately measure attitude, typically two or more types of actuators combine to apply torque to achieve a desired attitude.Before moving on to selecting the actuation technique and actuation hardware, we first analyze the disturbance torques which warrant the need for attitude control.

7.1 Torque Budget

We start by analyzing the worst-case torque environment at an altitude of 350 km,which is the altitude at which the drag compensation phase of the mission will take place. Then, this torque environment will be calculated at a higher altitude of 850 km, and the more severe torque environment will be used to design and specify the attitude control system.

7.1.1 Aerodynamic Drag Torque

In LEO, there is some residual atmosphere.However,the density being low, conventional fluid mechanics theories based on a continuum model do not apply , and interaction between the atmosphere and spacecraft must be treated at a molecular level. Therefore we assume that the momentum of molecules arriving

at the surface of the spacecraft is totally lost to it , and that the thermal motion of the atmosphere is negligible compared to the speed of the microsatellite. When the center of aerodynamic pressure is not aligned with the the center of mass, a torque results,given by [39]:

$$\tau_a = \frac{1}{2} C_D \rho A v^2 (C_{pa} - C_m) \tag{7.1.1}$$

Each of the parameters used in the above equation will be explained below.The worst case values will be selected, so that essentially we add a factor of safety while designing and specifying attitude control hardware.

Impacted area A = cross-sectional area perpendicular to the velocity vector at the along-track direction of the orbit.

It is clear that, due to the finite thickness of the satellite, the maximum cross-sectional seen by drag direction is not at incidence angle $\alpha_i = 0$ degrees.

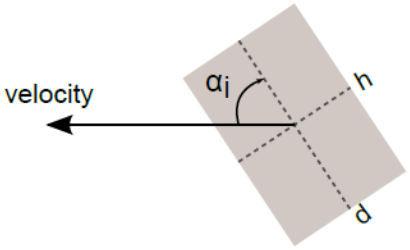

Figure 65: Definition of incidence angle α_i

Impacted area A is a function of the incidence angle α_i, and is given by [69]:

$$A(\alpha_i) = \frac{\pi d^2}{4} sin(\alpha_i) + dhcos(\alpha_i) \tag{7.1.2}$$

To find worst-case drag impacted area to be used to estimate the worst case torque, equation 7.1.2can be differentiated and set to zero, resulting in:

$$\alpha_{imax} = tan^{-1} \left[\frac{\pi d}{4h} \right] \tag{7.1.3}$$

Back-substituting equation 7.1.3 in 7.1.2 , we can find the worst case cross-sectional area which will result in worst-case aerodynamic drag torque.

C_{pa} =center of aerodynamic pressure and C_m =center of mass and when the aerodynamic eccentricity $C_{pa} - C_m \neq 0$, a drag torque results.

The value of α_{imax} can be used to calculate the most extreme value of aerodynamic eccentricity, from [70] :

$$C_{pa} - C_m(inches) = -55.805sin(\alpha_{imax}) + 94.439sin^2(\alpha_{imax}) + 35.21sin^3(\alpha_{imax}) - 32.966sin^4(\alpha_{imax}) \quad (7.1.4)$$

Strictly speaking, there exist in literature only recommended values for aerodynamic eccentricity for small satellites and the above formula has been used for larger structures. However, the value of aerodynamic eccentricity calculated from equation 7.1.4 is consistent with recommendations from [71], that the value of the aerodynamic eccentricity should be taken as one-third of the maximum spacecraft dimension. As we will see in the successive sections, in Low Earth Orbit, the maximum torque acting on our microsatellite will be the aerodynamic drag torque. Hence it is crucial to analyze the effect of the shape of the microsatellite, and what repercussions this will have on the aerodynamic drag torque. The D3SAT was initially designed as a cube of $40cm \times 40cm \times 40cm$. In the figure below, we fix d=0.4 meters, and vary h.

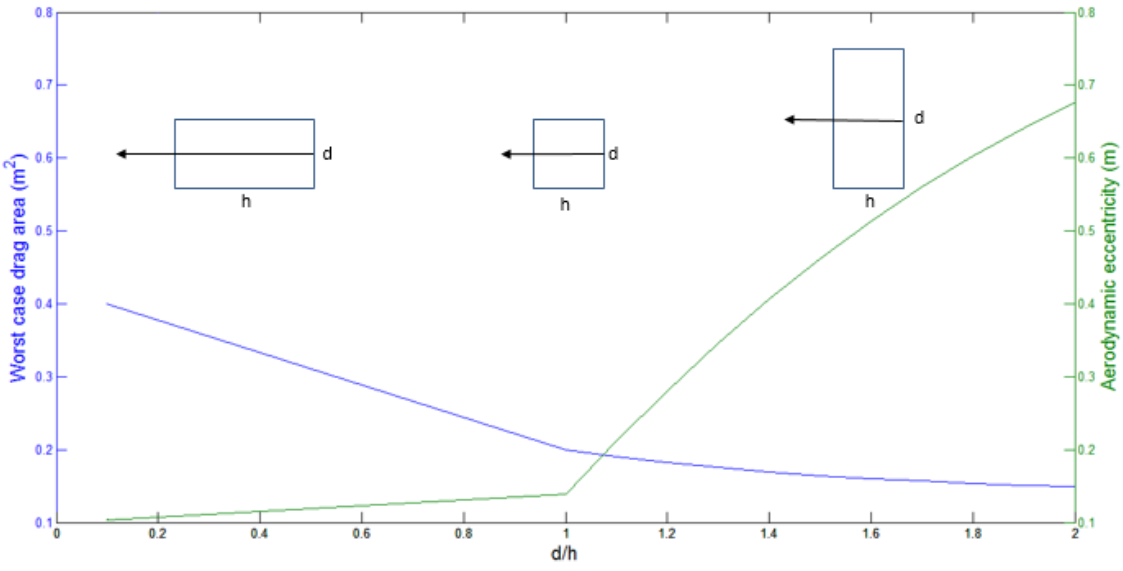

Figure 66: Effect of shape of the D3SAT on τ_a

We can see, that when d/h<1 , the aerodynamic eccentricity is low, but the worst case drag area is high.Near the region of d/h =0, flat plate analysis is approached.

When d/h>1,the worst case drag area will be low, but the aerodynamic eccentricity will rise drastically. Therefore, as a best compromise, we choose to proceed with d/h=1 for the microsatellite structure.

Fixing d=h=0.4 m, we want now find the worst case drag-impacted area and aerodynamic eccentricity to be used in our calculation for aerodynamic drag torque from equations 7.1.2 and 7.1.3.

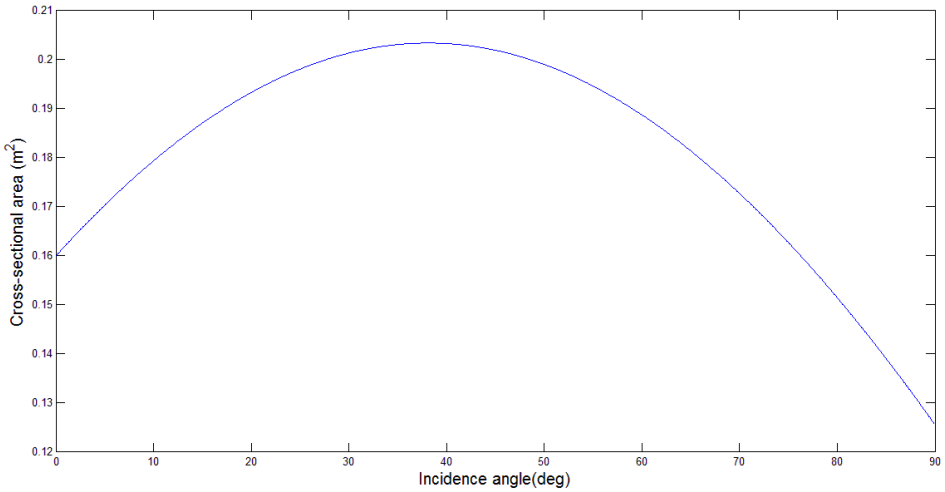

Figure 67: Worst-case drag impacted area

The worst case drag area of $A = 0.2\,m^2$is obtained for $\alpha_i = 38.14°$. Also the aerodynamic eccentricity from equation 7.1.4 is found to be 0.1 meters. The atmospheric density used is the worst-case density which occurs during period of maximum solar activity, taken from [39] as $\rho = 1.98e-11\,kg/m^3$. Now we move on to the choice of drag coefficient C_D As $\rho$and the C_D value are factored together as shown, the C_D value will absorb the errors of the atmospheric density,as well as absorb the uncertainties in the instantaneous cross-sectional area of the satellite[72].

A measure of the kinetic energy lost by molecules on collision with surfaces is the energy accommodation coefficient α_e,which is given by:

$$\alpha_e = \frac{E_i - E_r}{E_I - E_W} = \frac{T_i - T_r}{Ti - T_w}$$

where E_i is the kinetic energy transported to the unit area of the satellite surface by incident molecules, E_r is the kinetic energy carried away by reflected

molecules, and E_w is the energy that would be transported away if the reflected molecules had adjusted to the surface temperature before re-emission. The subscripts on the temperatures have the same meanings as those on the energies. A review of satellite measurements has revealed that, in low Earth orbit near 200 km, α_e is near unity and above 200 km, the accommodation coefficients are lower and when the accommodation coefficients are approaching 0 (which is the case at our altitude of 350 km),we see that the value of $C_D$should be selected based on diffuse reflection on a sphere[9].Diffuse reflection means that the air molecules are reflected off the surface of the microsatellite at many angles. Referring to[73] we see that appropriate value of drag coefficient should be 2.4. This value is also confirmed from the figure below:

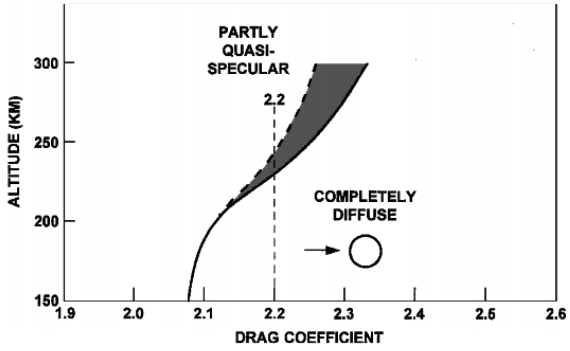

Figure 68: Choice of C_D(Source:[9])

The velocity v is the circular velocity, equal to 7.7 km/s.The worst-case value of aerodynamic drag torque is about $21\mu N - m$ at 350 km.

7.1.2 Magnetic Field Torque

The liquid core of the Earth generates a magnetic field that will have effects on the space surrounding the planet. Due to the fact that spacecrafts have some level of residual magnetic moment, the surface of the spacecraft can develop a charge of its own giving it a distinct dipole-north/south ends, like a compass. Just as a compass needle rotates to align with Earth's magnetic field, the dipole charged spacecraft will similarly try to rotate as it passes through the magnetic field. The size of this magnetic torque depends on the spacecraft's effective magnetic dipole and the local strength of Earth's magnetic field. The Earth's magnetic field is complex, asymmetric and not aligned with the Earth's spin axis, and varies with geographical movement of the dipole as well as changes in solar particle flux.

However, we model the Earth's magnetic field as a dipole and determine the maximum possible value of the magnetic torque for the microsatellite. To try to model all of this would be very time demanding and not very constructive. Hence we have to make a rough approximation. The torque is given by [39]:

$$\tau_B = D_{residual} * B \tag{7.1.5}$$

Sources of magnetic disturbance originating from the microsatellite can be caused by permanent magnetism originating from components on-board, or from spacecraft generated current loops. It is very difficult to have a model for this internal dipole generated by the microsatellite, for the reason that different electronics have different characteristics and on the satellite many different components are being used.There are two possible ways to estimate this residual dipole moment:

1)Estimation in the laboratory on the basis of measurements made on similar components which are being used for the mission

2)Comparison with previous microsatellite missions having similar mass and power properties and having similar mission profiles

Referring to [74], we get recommended values of spacecraft residual dipole moment:

	Residual dipole moment per unit mass $[A - m^2/kg]$	
Class	**Non-spinning spacecraft**	**Spinning spacecraft**
1	1×10^{-3}	0.4×10^{-3}
2	3.5×10^{-3}	1.4×10^{-3}
3	$\geq 10 \times 10^{-3}$	$\geq 4 \times 10^{-3}$

Class 1:Magnetic torques are much more dominant than other disturbance torques
Class 2 :Magnetic torques are comparable with other disturbance torques
Class 3:Magnetic torques can be considered insignificant with respect to other disturbance torques

Table 20: Residual dipole moment

From the above table, we select residual dipole moment per unit mass for a class

2 non-spinning spacecraft. Since the mass of the D3SAT is taken as 40 kg, we get $D_{residual} = 3.5 \times 10^{-3} \times 40 = 0.1A - m^2$

Recommendations to control spacecraft magnetic dipole moment:

Hard magnetic materials must be chosen over soft magnetic materials.In hard magnetic materials, magnetic moment is not changed significantly due to change of magnetic field around it .Aluminum, fiberglass, magnesium and titanium are all non-magnetic. These are among the most desirable materials for use in the structure.Ordinary nickel welding wire used for inter-connections between components in welded modules is highly magnetic and it is recommended to not not be used on D3SAT mission. A nickel-copper alloy should be considered for welding.With respect to the solar arrays, effort should be made to minimize the loop area of the current routes, and a common and effective technique is to route current wires directly behind the solar cells.The residual magnetism when the HT-100D is off and the interaction of the magnetic circuit of the HT-100D with the microsatellite is out of the scope of this thesis, and is a recommendation for future work.

The magnetic field vector will be taken as the maximum, in order to calculate the worst-case magnetic field torque. As a starting point, we use the MATLAB function *igrf* in order to see the distribution of the magnetic field lines, and see where the earth magnetic field strength is the maximum.

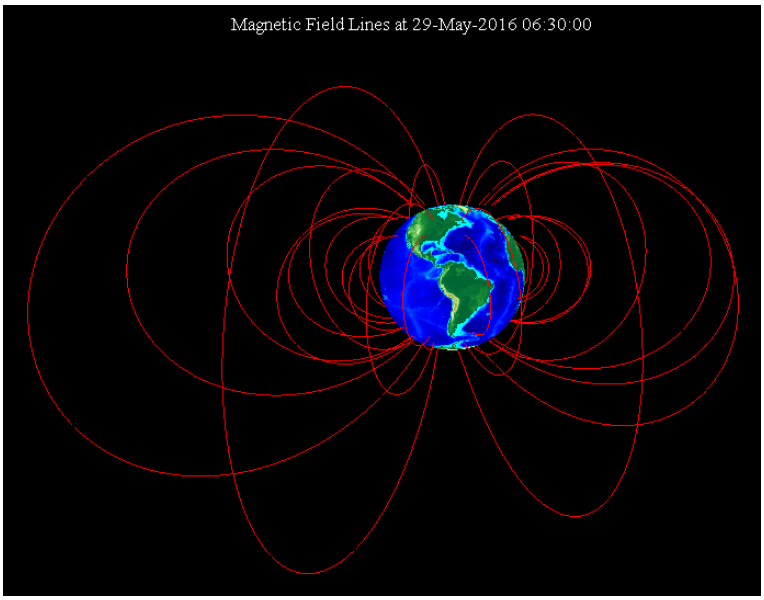

Figure 69: Earth magnetic field lines

The magnetic field strength is found to be maximum at the magnetic south pole, which as of 2015 is located at $64.28°S, 136.59°E$. The value of the magnetic field vector over the magnetic south pole in May 2016 is : $\mathbf{B} = 1e-4 \begin{bmatrix} 0.0140 \\ 0.0105 \\ -0.5601 \end{bmatrix} T$

The strongest magnetic field will be along the Z-component of the magnetic field vector. The values drift over time and in order to calculate the worst-case earth magnetic field torque, we analyze the variation in Z-component of magnetic field and the total intensity from 2016-2020.

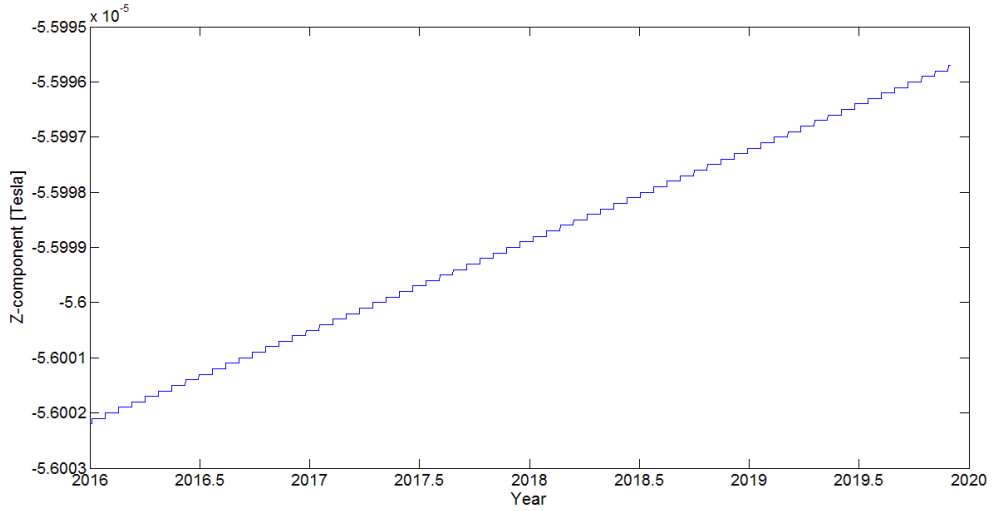

(a) Z-component

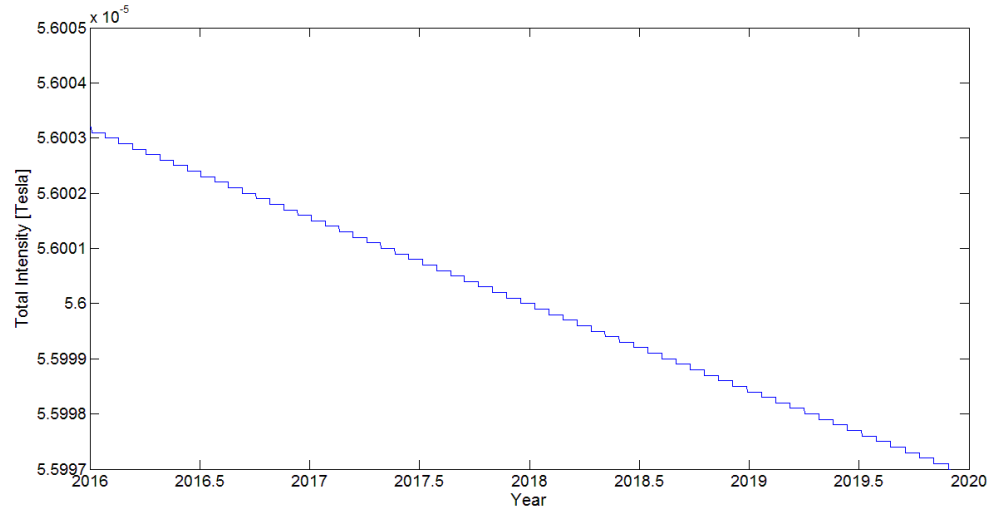

(b) Total intensity

Figure 70: Variation of Earth magnetic field from 2016-2020

Therefore ,we can confirm that the worst case intensity to be used in calculation of magnetic field torque is $5.6e-5T$.The worst-case value of magnetic field torque at 350 km is about $5.6\mu N-m$.

7.1.3 Solar radiation pressure torque

The photons from the sun contain momentum which produce an effective pressure on the microsatellite surface, due to momentum transfer. These photons with the spacecraft can be absorbed, specularly reflected, diffusely reflected or transmitted from the spacecraft surface. Different surfaces will experience different pressure forces, for example, the solar arrays would absorb more light than the metallic surfaces. Also, surfaces that are at angles to the sun would have less pressure than those faces which directly face the sun. By assuming a uniform reflectance, we can use the following equation, adapted from [39]:

$$\tau_S = \frac{\Phi}{c} A_s q (C_{ps} - C_m) cos\varphi \tag{7.1.6}$$

The solar constant $\Phi = 1367 W/m^2$at 1 AU. The solar constant varies with time. Its variations are conventionally related to the solar activity variation, i.e., to the physical processes on the Sun.The long-term variations of the solar constant are related not only to the variation of solar activity, but also to the celestial mechanical processes that change the distance between the Sun and the Earth. During the unperturbed motion of the Earth, the solar constant varies within an annual orbital motion of the Earth around the Sun with regular annual variation, with the maximum being at the perigee and the minimum at aphelion. However, the real orbital motion of the Earth is a perturbed motion,and the Earth is at a different distance from the Sun from year to year (while passing through the equinoctial and solstitial points). We choose a worst-case value of the solar constant based on the constant model of the solar flux, as shown in the table below, adapted from [75].

Mean solar flux at 1 AU	$\Phi = 1371 \pm 10\ W/m\text{^}2$
Maximum solar flux(summer solstice)	$\Phi = 1428\ W/m\text{^}2$
Minimum solar flux (winter solstice)	$\Phi = 1316\ W/m\text{^}2$

Table 21: Variation of solar constant Φ

Hence we choose $\Phi = 1428\,W/m^2$.The speed of light is $c = 3e8\,m/s$.

The sunlit areaA_S is taken as $A_S = A + A_{s1} + A_{s2}$,where A is taken as the drag impacted area,$A_{s1} = 0.6m$and $A_{s2} = 0.9m^2$are the areas of the two solar panels. The final sunlit area is taken as $1.6\,m^2$.

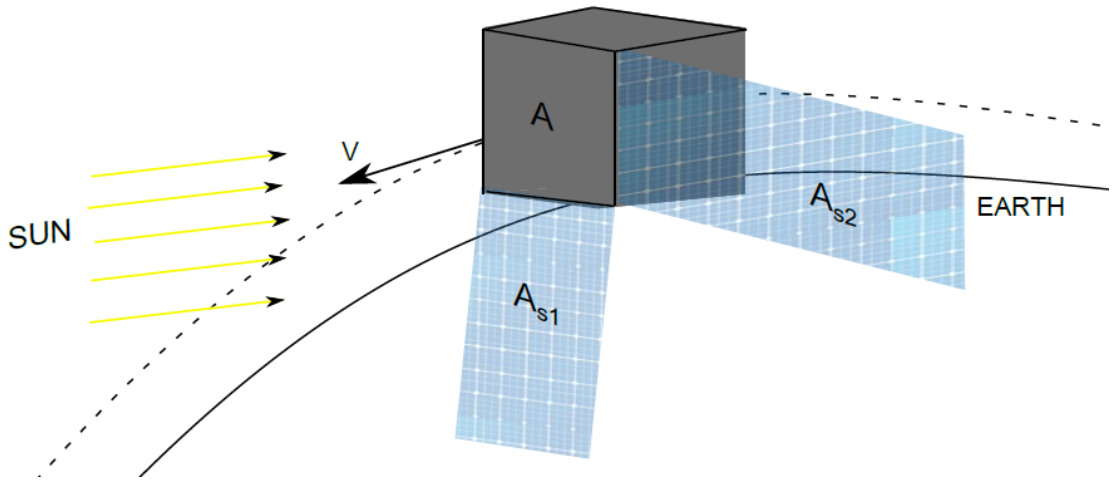

Figure 71: Sunlit area A_S

Interaction of photons with the sunlit area can occur in three ways:photons are absorbed by the sunlit face and transmit energy to the spacecraft; photons are reflected off of the spacecraft, imparting even more energy to the spacecraft;photons heat up the spacecraft, which can change the thermal radiative characteristics of the spacecraft. The unitless reflectance factor q must account for for different materials of the D3SAT and the material of the solar panels.q is considered 0 if the body is translucent,$q = 1$ is perfect absorption takes place at the surface and $q = 2$ if the photons are perfectly reflected off the sunlit area. Since the area of solar panels is much greater than the drag impacted area, it makes sense to take the value of $q = 1$, since the solar panels absorb the solar energy and convert it to electrical energy.The reflectance factor is very difficult value to characterize and know accurately[22].However, a representative value for finding the reflectance factor based on the diffuse reflectivity value δ for the solar panel material.For typical GaAs cells, from [76],$\delta = 0.168$.From the same paper,an approximation for the reflectance factor is given as:

$$q = 1 + \frac{4}{9}\delta = 1.08$$

Photons act on average through the center of pressure; if that isn't aligned or coincident with the center of mass then a torque is applied to the spacecraft. For this analysis, center of solar radiation pressure C_{ps} is taken as equal to C_{pa}.Therefore $C_{ps} - C_m = C_{pa} - C_m = 0.1\,m$.

φ is angle of incidence of the sun on A_s,and as seen from the figure below, the solar radiation pressure torque is maximum when the angle of incidence is zero, that is, when the photons from the sun are normal to the sunlit area .

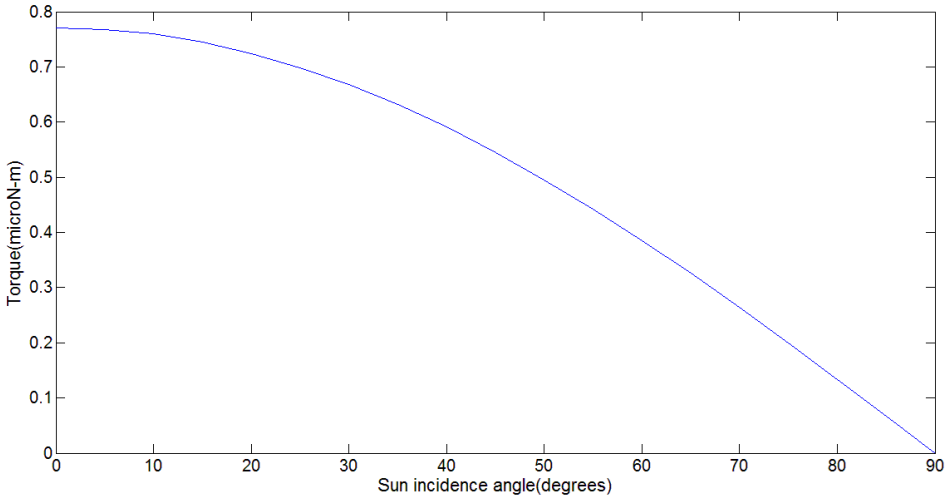

Figure 72: τ_S variation with incidence angle φ

The worst-case value of solar radiation pressure torque at 350 km is $0.7\,\mu N - m$.

It has been studied in [46], that for drag compensation, a solar array area of $0.6\,m^2$ is required for the reference case 1, and for deorbiting to 225 km from 350 km, an extra $0.9\,m^2$is required to supply the extra power required for deorbiting. Therefore, it is suggested that during drag compensation, only one solar panel of $0.6\,m^2$will be deployed and this configuration will stay for a major part of the mission, thereby rendering SRP torque negligible. An additional solar array area $0.9\,m^2$ can be deployed when deorbiting has to be performed. This way, during drag compensation the SRP torque will be about $0.3\,\mu N - m$ and during deorbiting, it will increase to about $0.7\,\mu N - m$,as seen in the figure below:

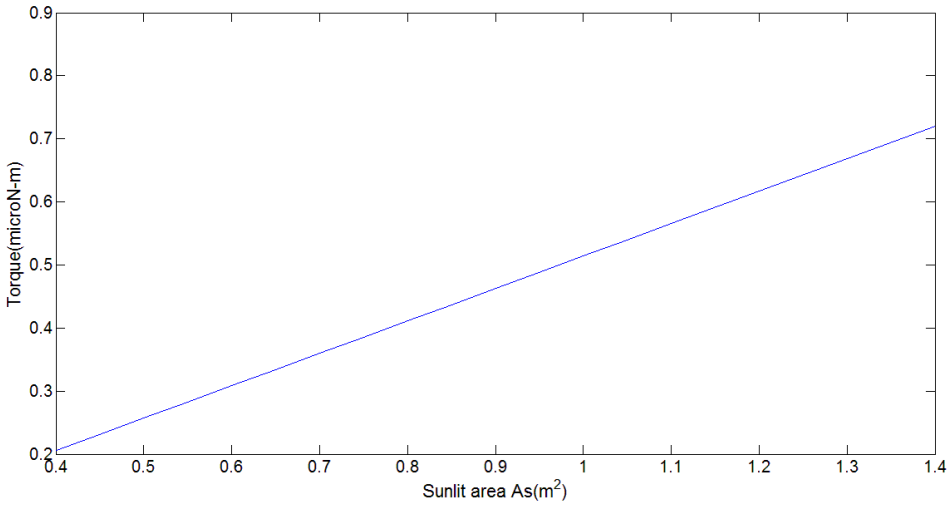

Figure 73: Effect of sunlit area $A_S$on τ_S

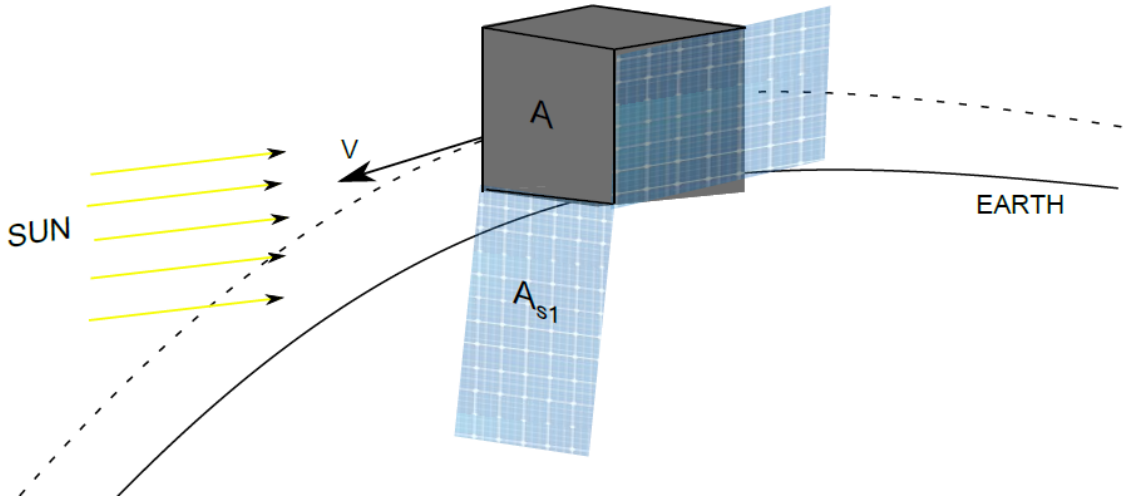

Figure 74: Proposed solar array configuration during drag compensation

7.1.4 Gravity Gradient Torque

The Earth's gravitational force is not constant with distance from the center, but decreases quadratically. Hence the gravitational force at some distance on the D3SAT will be different on some point farther away. This produces a torque, which is given by[39]:

$$\tau_{gg} = \frac{3\mu}{2R^3}(I_y - I_x)sin(2\theta) \tag{7.1.7}$$

Where I_x,I_y=smallest and largest moments of inertia .$\theta$is the angle of deviation of the Y-axis from the local horizontal.It is basically the pitch angle. As the pitch angle deviates from zero value, due to the deployed solar panel, it will result in the build-up of gravity gradient torque, as shown in the figure below.

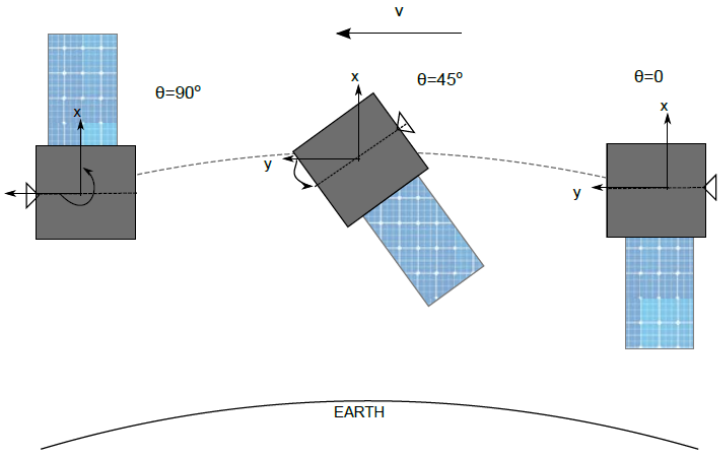

Figure 75: Definition of θ for τ_{gg}

We can see from the figure below that gravity gradient torque is maximum when $\theta = 45°$.

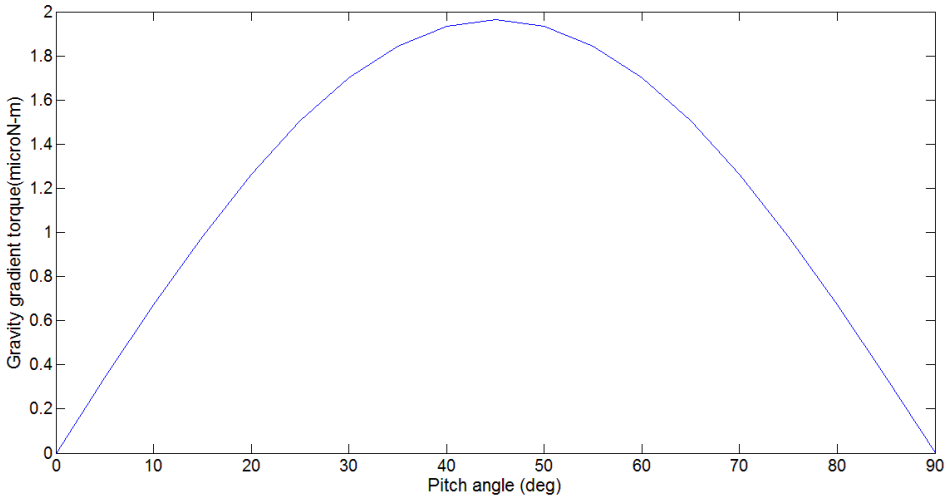

Figure 76: Effect of θ deviation on τ_{gg}

If the required attitude of ±5°along all axes is maintained, the gravity gradient torque will be negligible.However, to include the worst-case scenario in the torque budget, we take the maximum value of this torque at 350 km, which is $2\,\mu N - m$.

After calculating the worst-case torque environment at an altitude of 350 km ,the worst-case torques at an altitude of 850 km is calculated.As can be seen in the figure below,the dominant torques at 350 km are the aerodynamic drag torque and the magnetic field torque.

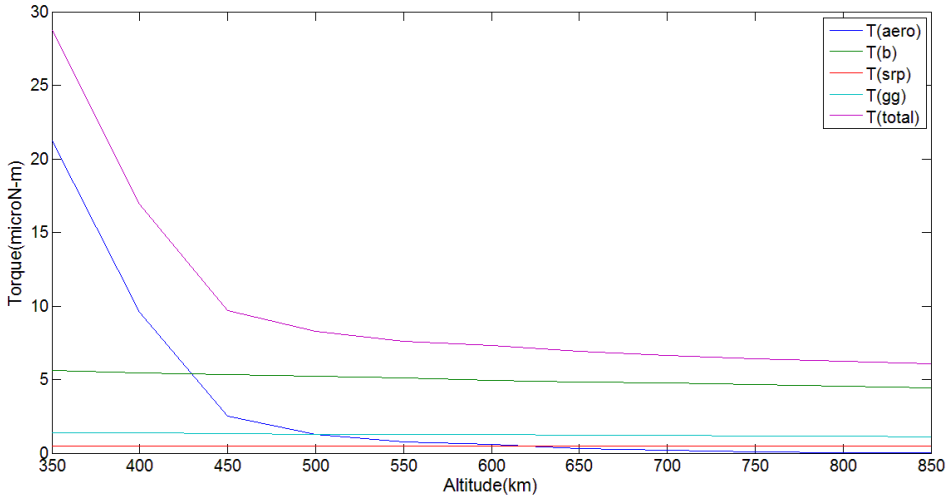

Figure 77: Disturbance torques as a function of altitude

TORQUE ($\mu N - m$)	h=350 km	h=850 km
Aerodynamic drag	21	0.03
Earth Magnetic Field	5.6	4.4
Solar Radiation Pressure	0.7	0.8
Gravity Gradient	1.4	1.1
TOTAL	28.5	7

Table 22: Torque budget

Besides the above external disturbances, there can be internal torques generated by the microsatellite itself, for example:

1)Dynamic imbalance due to rotating components with off-diagonal inertia terms

2)Friction from rotating or sliding parts

3)Thermal deformation

4)Uncertainty in center of gravity

5)Dynamics of flexible bodies

These internal disturbance torques are ignored in this thesis.

7.2 Selection of ACS technique

We can conceptually divide actuator types into two general classes, passive and active. Passive actuators operate more or less open loop. In other words, after the spacecraft is in the desired attitude, passive actuators will keep it there with little or no additional torques needed. Active actuators, on the other hand, require continuous feedback and adjustment. Before selecting whether we have to implement active or passive control, we will first study the types of passive and active actuation techniques.

Passive attitude control

1)Gravity gradient

This type of passive actuator exploits the effect of the gravity gradient disturbance torque discussed in section 7.1.4. This "free" torque can be used to keep a spacecraft oriented in a local vertical, or "downward," orientation. However, to maximize the effect of this cheap and reliable attitude actuator, a spacecraft usually uses deployment of weighted booms. In spite of this technique being simple and cheap, this cannot be used since the torques generated by this type of arrangement are symmetric around the nadir vector, thereby controlling only the pitch and roll axes, and not influencing yaw. Yaw orientation will be required, since the thruster cannot be gimballed.

2) Spin stabilisation

A spin-stabilized spacecraft takes advantage of the conservation of angular momentum to maintain a constant inertial orientation of one of its axes. Since the angular-momentum vector of a spinning mass is fixed in inertial space, the spacecraft tends to stay in the same inertial attitude. This is not sufficient, since we

have to perform different functions with our thruster. One way to avoid Earth-pointing limitations of spin stabilization is to use a dual-spin system, where the satellite will have two sections spinning at different rates about the same axis. However, the need for independently spinning sections makes this configuration much more complex, on account of the electrical connections needed between the two sections and also the need for reliable bearings which helps to reduce the friction between the two parts. Also, this configuration causes the satellite to be in constant rotation, and therefore we reject this attitude control technique.

3)Dampers

A damper is a device that changes angular momentum by absorbing energy. Attitude dampers use friction or other means to convert angular momentum energy into other forms. For a small satellite, this option does not make sense this will add to thermal problems, and also increased mass due to viscous fluid used for damping.

In order to get a reasonable accuracy on the attitude control, active stabilization methods are required. They are more expensive and harder to implement then passive methods, but is necessary to be able to carry out the D3SAT's main mission. The benefits include the capability to have the microsatellite autonomously track any arbitrary pointing requirement and also allows a huge flexibility of maneuvers the satellite can perform. Various types of active actuation are studied to analyze their feasibility for the mission. Since we have only one thruster, and it cannot be gimballed, it is clear that we will not be using the HT-100D for attitude control. Therefore the techniques studied below all belong to the class of momentum-control actuation, which use devices that vary the angular momentum of small rotating masses within the satellite to control its attitude.

Active attitude control

1) Momentum wheels

Momentum wheels, also called biased momentum systems, rely on a single wheel with a large, fixed momentum to provide gyroscopic stiffness to the microsatellite. The speed of the wheel gradually increases or decreases in the process of rejecting disturbance torques. This works in a similar way to spin stabilisation and therefore this option can be rejected.

2) Reaction wheels

Reaction wheels, or zero-bias systems have their normal momentum at or near zero. Typically, an attitude control system uses at least three separate reaction wheels, oriented at right angles to each other. Each wheel spins independently to rotate the spacecraft and absorb disturbance torques, by changing the magnitude of spin.

3) Control Moment Gyroscopes

Attitude control systems using control moment gyroscopes rely on three or more wheels, each with a large, fixed momentum. The wheels are mounted on gimbals, which allow them to rotate freely in all directions, thereby changing the satellite orientation. Recall that reaction wheels change momentum by changing magnitude only, whereas CMGs change momentum by changing their magnitude and direction.

Both control moment gyroscopes and reaction wheels are suitable candidates as actuators for the attitude control system. In the following section, we compare these two options and make a final selection.

7.3 Selection of ACS hardware

A reaction wheel is a momentum exchange device mounted a spacecraft. In the absence of external torques, if the if the angular momentum of the wheel is changed, there must be a corresponding opposite change of angular momentum of the microsatellite. To control the microsatellite attitude, angular momentum is transferred between the wheel and the microsatellite platform. By mounting three reactions wheels with spin axes in not in the same plane, a torque can be created about an arbitrary axis of the satellite. When the spacecraft attitude is controlled using these reaction wheels, when the angular momentum of the microsatellite changes, the wheels will have a changed angular momentum. Therefore, reaction wheels cannot be used exclusively because the angular momentum storage capacity is limited and hence arises the need to augment this system with reaction-type actuators, which create an external torque and hence desaturate the reaction wheels.

Before commanding a control torque to the CMG, the gimbal angular rates must be calculated, therefore making the CMGs more computationally burdensome. The torque provided by CMGs are always higher, and that too with lower power consumption, as seen below in [10], where a market study has been done of commercially available control moment gyroscopes and reaction wheels.

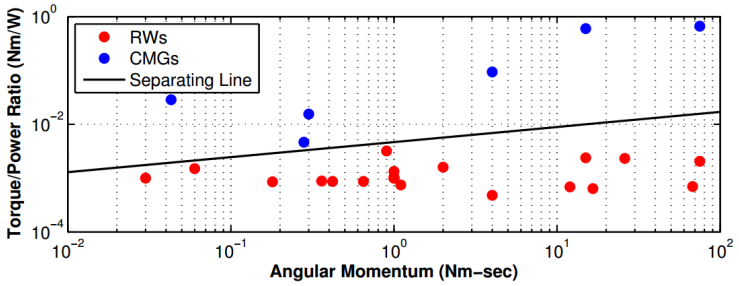

Figure 78: Torque/power vs. momentum comparison of CMG's and RW's([10])

Therefore we see that CMG's are more efficient from the power point of view. However,the additional gimbal motor and hardware for the CMG will add to the mass and volume. This can be seen in the figure 79, which is taken from the same paper referenced above. In addition, CMGs provide pointing accuracy equivalent to reaction wheels but offer much higher slew rates and are especially effective on very large platforms. Keeping in mind the mass and power constraints of our small satellite, we choose reaction wheels as the attitude control hardware.

One important limitation of all momentum control devices is the practical limit on how fast a given wheel can spin. In operation, the reaction wheels must gradually spin faster and faster to absorb the disturbance torques. Typically, a periodic disturbance torque along one spacecraft axis would result in a cyclic variation in the angular velocity of the wheel directed along that axis, while a constant (secular) disturbance would lead to a linear increase in angular velocity[77]. This is due to the fact that the wheel would be accelerated at a constant rate in order to transfer to it the excess angular momentum generated by the external disturbances. If the disturbance is cyclic , the wheel may not approach the design limit for its rotational speed, or 'saturation' for a long time. However, secular disturbances, which build up over time, will cause the wheel to approach saturation. Therefore, an independent external torque must be applied to force the wheel speed back towards zero, so that the reaction wheels such that they can continue to provide torque[78]. This process is known as momentum dumping.

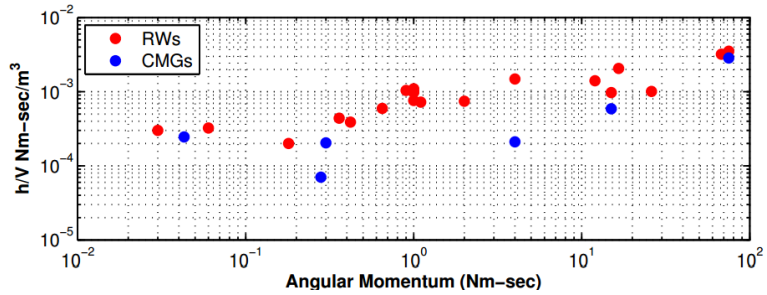

(a) Angular momentum/volume vs. momentum

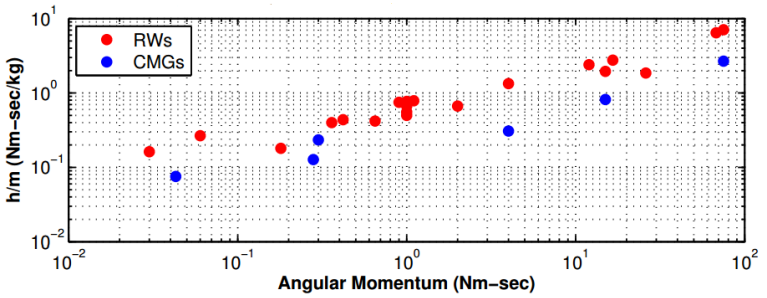

(b) Angular momentum/mass vs momentum

Figure 79: Mass and volume comparison of CMG's and RW's(Source:[10])

For small satellites in Low Earth orbits (LEO) magnetorquers provide a cheap, reliable and effective external torque for momentum desaturation purposes[79, 80]. Magnetic coils, or magnetorquers, are winded electromagnetic coils with or without metallic cores. The magnetic coils creates a magnetic field when electrical current is applied. This electromagnetic field then tries to align with Earth's magnetic field, dragging the rest of the microsatellite with it, creating a torque acting on the satellite. Magnetorquers can be thought of as a compass, which acts as shown in the figure 80. The magnetic coils are cheap and light,and they never saturate, because they can always carry electric current. However the torque produced by them is highly dependent on the Earth's magnetic field. It's only possible to apply a control torque in the direction perpendicular to the geomagnetic field vector. That is why 3 magnetorquers are required, one along each axis.

Another disadvantage of magnetorquers is that very high magnetic flux densities would be needed if quick maneuvers need to be executed. This means either very high current in the coils, or much higher ambient flux densities than are available in Earth orbit. As a result, the torques provided are very limited and only serve to accelerate or decelerate the change in a spacecraft's attitude by minute amounts. Thus, using magnetorquers in conjunction with reaction wheels is the best option

to have the most control torque available.

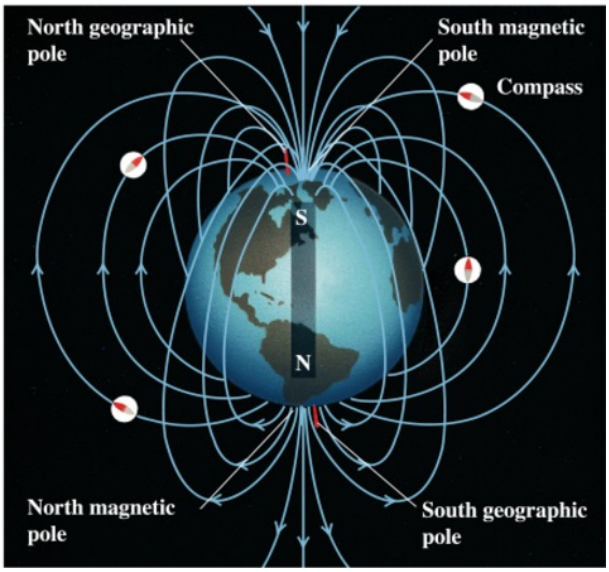

Figure 80: Magnetorquer working principle

7.4 ACS hardware sizing

7.4.1 Reaction wheel sizing

The torque provided by the reaction wheels must be equal to the worst case torque plus a certain margin. If we add a safety margin of 30 %, this means that the required torque of the reaction wheel at 350 km is 36.6 $\mu N - m$.The required torque levels of the reaction wheels to reject external disturbance torques at different altitudes (with a margin of 30 %) are shown in the figure below:

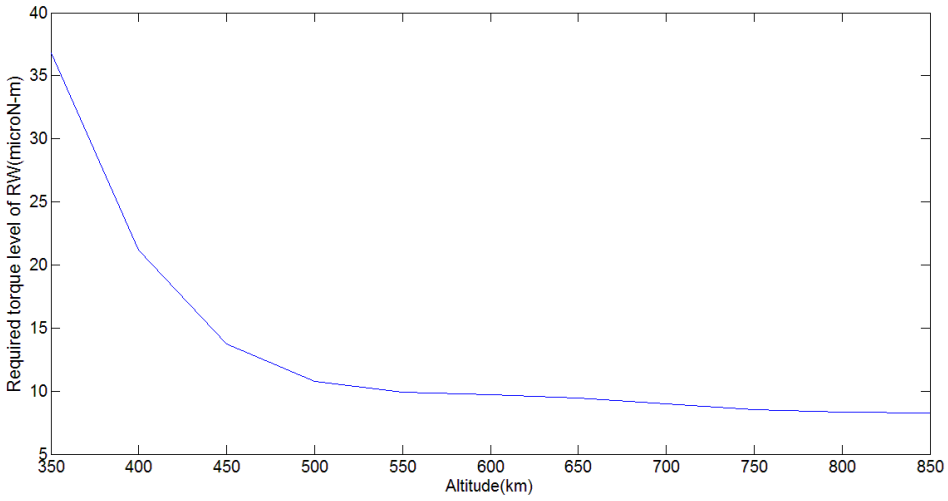

Figure 81: Required torque level of reaction wheels with altitude

This torque level is well below the available capabilities of numerous candidate reaction wheels for microsatellites. Therefore, we will size the reaction wheels not on the basis of torque rejection, but on the basis of angular momentum storage. In sizing wheels, it is important to distinguish between cyclic and secular disturbances. Cyclic disturbance torques oscillate over an orbit, whereas secular disturbance torques build up angular momentum over time. For reaction wheels, cyclic torques build up angular momentum over time, as the wheels provide opposing compensating torques to maintain the desired attitude[39]. Cyclic torques can be easily handled by the reaction wheels, as they will have to store this torque only for a short time. Typically, the angular momentum capacity of a reaction wheel (limited by its saturation speed) to handle the cyclic storage during an orbit without the need for frequent momentum dumping is used for sizing.

To classify our external disturbance torques, we see their short-term behavior (over 1 orbit) and long-term behavior (over one day).

In order to see how the disturbance torques will act on the D3SAT, it is important to first see the effect of perturbing accelerations on the microsatellite. These perturbations will cause the microsatellite orbit to deviate from theoretically regular orbital motion. Therefore, the radius and velocity vector components of the D3SAT will be perturbed, and this will cause a slightly different external disturbance torque profile to be experienced by the D3SAT. The method used to find this perturbed motion is Cowell's method. For the two-body problem with perturbations, the equation is given by:

$$\ddot{\vec{r}} + \frac{\mu}{r^3}\vec{r} = \vec{a_p} \tag{7.4.1}$$

Equation 7.4.1 is a second order non-linear differential equations can be broken down into:

$$\dot{\vec{r}} = \vec{v} \quad \vec{v} = \frac{-\mu}{r^3}\vec{r} + \vec{a_p} \tag{7.4.2}$$

$\vec{a_P}$represents the sum of the perturbing accelerations.The perturbing accelerations considered are only drag and J2.

The acceleration due to drag is given by:

$$a_{drag} = -1/2 \cdot \rho A \cdot C_d \frac{norm(v)\cdot}{m}\vec{v} \tag{7.4.3}$$

The acceleration due to J2 is given by:

$$a_{J2} = -\frac{(3J_2\mu R_E^2)}{2 \cdot norm(r)^7}\begin{bmatrix} X(X^2+Y^2-4Z^2) \\ Y(X^2+Y^2-4Z^2) \\ Z(3X^2+3Y^2-2Z^2) \end{bmatrix} \tag{7.4.4}$$

Where X, Y, Z are the components of $\vec{r}$.

Equations 7.4.1to 7.4.4 are numerically integrated by adapting a MATLAB script[81]which is available at [82].Since the worst case torque environment is at an altitude of 350 km (from table 22), and since we are assuming a circular orbit, the initial conditions will be:

Classical Orbital Elements		Position and Velocity Vectors	
a	6728 km	R_X	6728 km
e	0	R_Y	0
i	98 degrees	R_Z	0
Ω	0	V_X	0
ω	0	V_Y	-1.071 km/s
ν	0	V_Z	7.622 km/s

Using $\vec{r}(t)\ and\ \vec{v}(t)$, the torque profile for each of the external disturbance torques discussed in section 7.1 is found over 1 orbit and over 1 day. The assumptions made have been specified.

1)Atmospheric drag torque

The assumption of small Euler Angles is made. It is also assumed that the drag area A , C_D and $C_{pa} - C_m$ remains constant. The density model is the worst case density during solar maximum taken from [39].

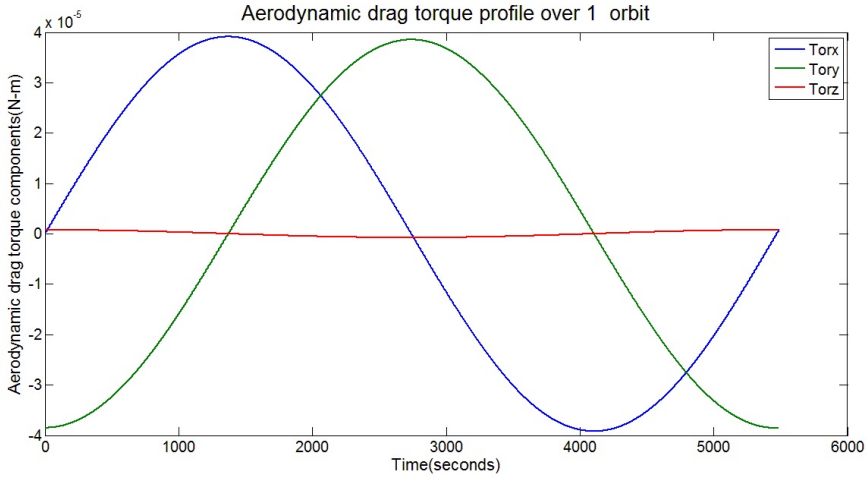

(a) 1 orbit

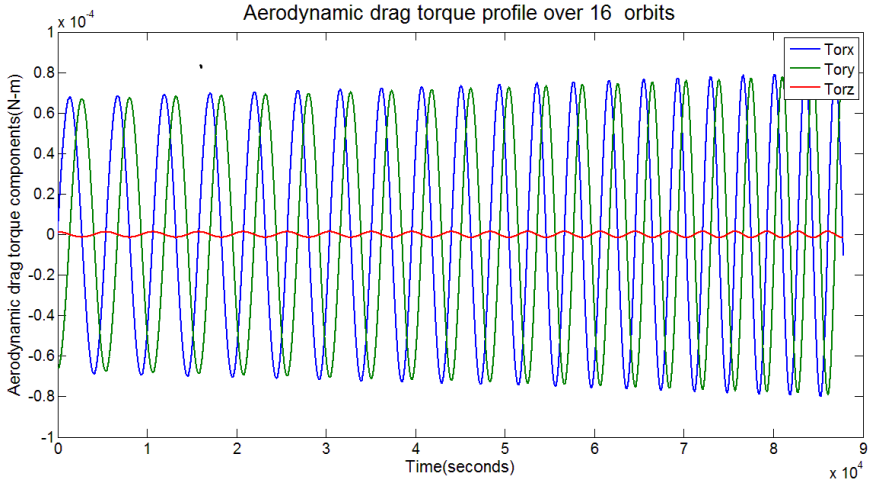

(b) 1 day

Figure 82: Atmospheric drag torque profile

We can see that the atmospheric drag torque exhibits secular behavior, thereby building up angular momentum in the reaction wheel over time.

2)Magnetic field torque

The assumption of small Euler Angles is made. It also assumed that $D_{residual} = 0.1\,A - m^2$ in all axes. The position vector is converted to latitude and longitude function using the MATLAB function *ecef2lla*, and the latitude and longitude information is used to find the geomagnetic field components using the function *igrf*.

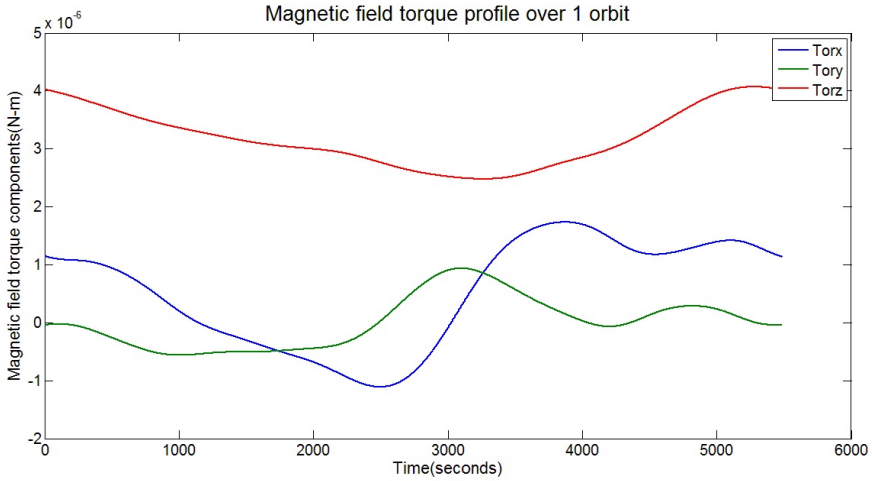

(a) 1 orbit

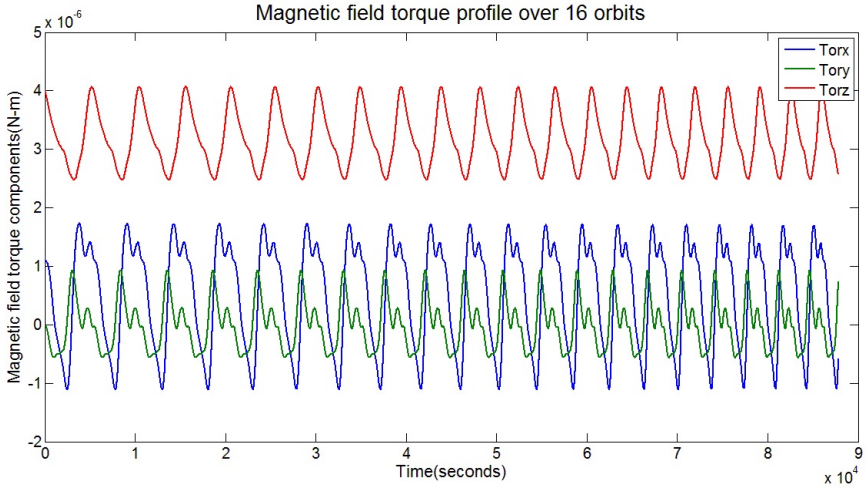

(b) 1 day

Figure 83: Magnetic field torque profile

The magnetic field torque profile is cyclic, and thereby the reaction wheel will only have to store the torque for a while.

3)Solar radiation pressure torque

As seen in table 22, the solar radiation pressure torque is negligible compared with the other disturbance torques. We assume that the $A_s$and $C_{ps} - C_m$ remains constant. Under these assumptions, from [39], we see that the solar radiation pressure torque will exhibit cyclic behavior.

4) Gravity gradient torque

We assume that as the initial condition, maximum deviation of the Y-axis from the local horizontal ,that is, pitch angle $\theta = 45°$, since this angle will cause the worst case gravity gradient torque(from figure 76) . This will result in a secular behavior of the gravity gradient torque, as shown below.

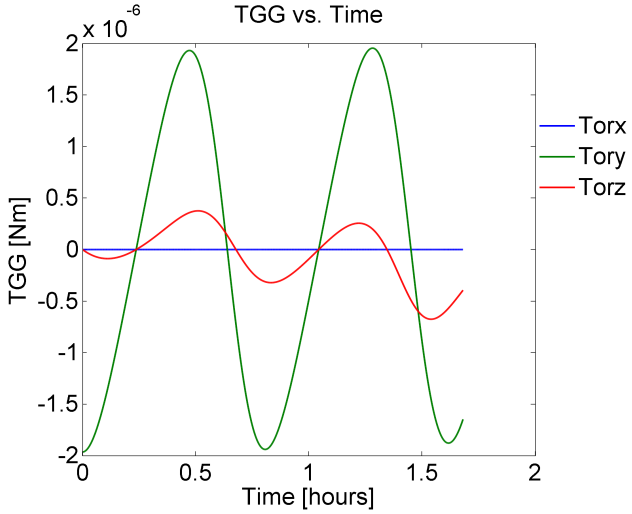

(a) 1 orbit

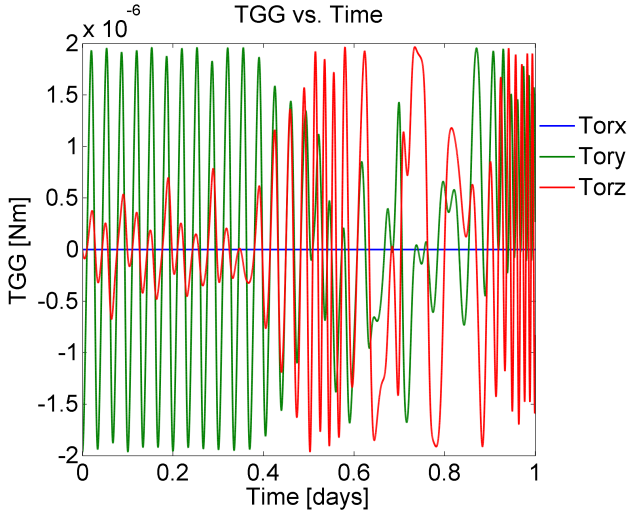

(b) 1 day

Figure 84: Gravity gradient torque profile

Therefore we can assume that gravity gradient torque and aerodynamic drag torque act throughout the orbit, whereas the solar radiation pressure torque and magnetic field torque are cyclic ,and accumulate in a quarter of the orbit([5],[39]). The required angular momentum storage capacity of the reaction wheel can therefore be calculated as:

$$H = [\tau_a + \tau_{gg} + (\frac{\tau_b + \tau_{srp}}{4})] * T * 0.707 \tag{7.4.5}$$

where 0.707 is the RMS average of a sinusoidal function.

At an altitude of 350 km, we get required momentum storage capacity of the reaction wheel $H = 0.1\,N - m - s$.

The torques used are the worst case torques from table 22.

We also see the storage momentum requirements at different altitudes.Using a power model from [10], we can see the Power demand by the reaction wheel $=1000\tau + 4.51H^{0.47}$, which is the power required to maintain nominal torque level at nominal speed(this power model was determined in [10]by examining 20 reaction wheels for small satellites). T is taken from figure 81.

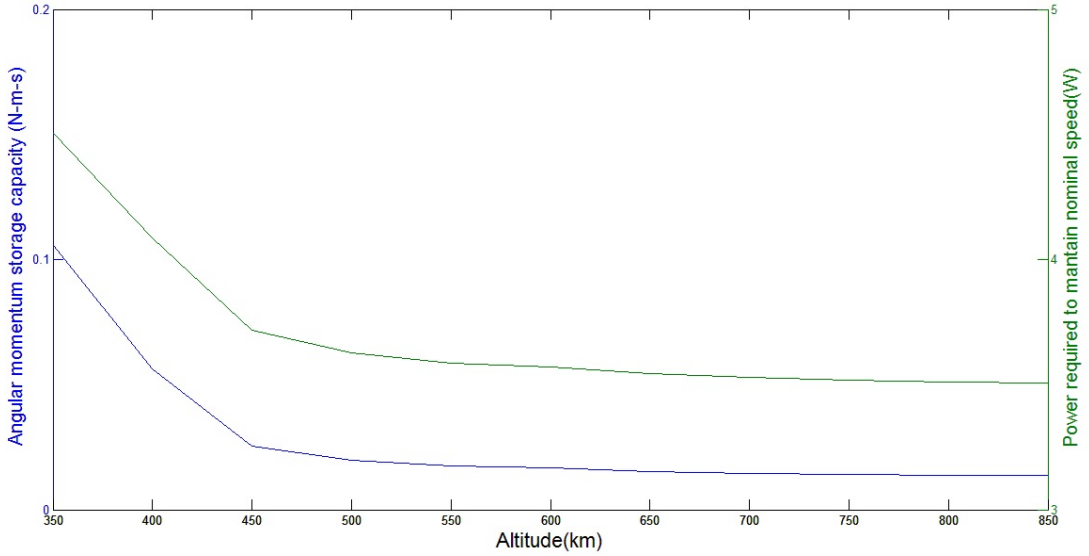

Figure 85: Reaction wheel requirements with altitude

For the required angular momentum storage capacity at an altitude of 350 km, we choose the reaction wheel RW 35 from Astro- und Feinwerktechnik Adlershof GmbH which has can provide nominal torque of $0.005\,N-m$ and has angular momentum storage capacity of $0.1\,N-m-s$ at the nominal rotational speed of $5000\,rpm$([83]). In addition, it also comes equipped to provide extensive housekeeping data.

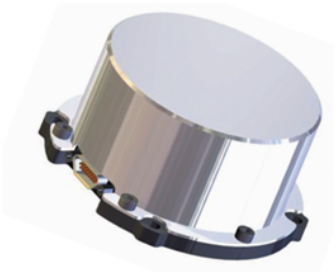

Mass(kg)	Power(W)	Dimensions
0.5	3	$95mm \times 95mm \times 40mm$

Figure 86: RW 35 ,AFAG specifications

7.4.2 Magnetorquer sizing

The magnetorquer is selected based on the magnetic moment capacity, which we can calculate in a first approximation as the maximum torque to be rejected at a certain altitude divided by the worst-case magnetic field strength at that altitude[39]. The worst case magnetic field strengths are over the magnetic south pole, as seen in section 7.1.2. The required dipole of the magnetorquers at various altitudes are shown in the figure below.

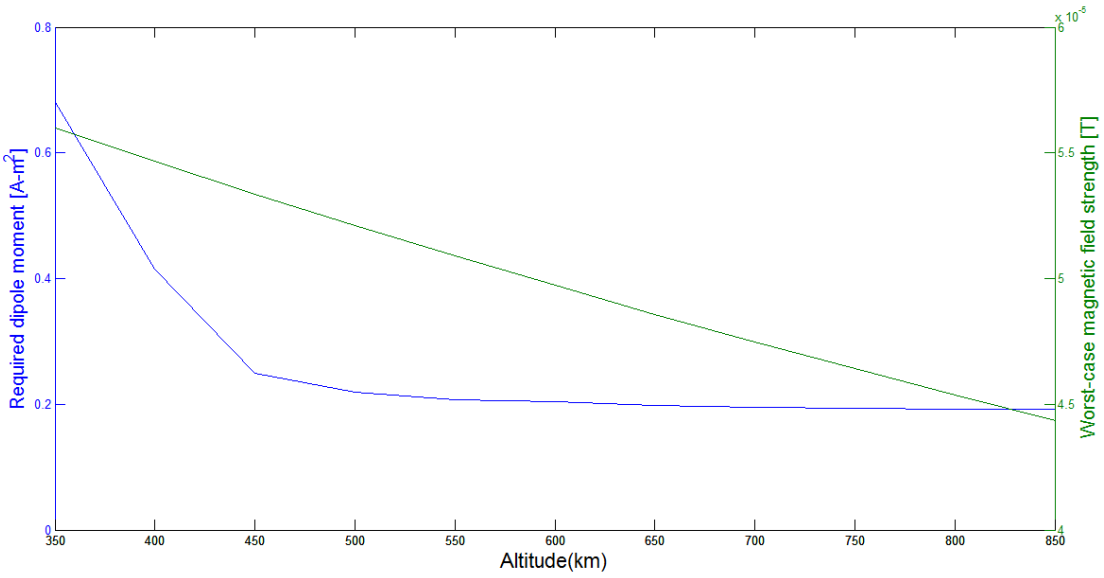

Figure 87: Required magnetorquer dipole vs altitude

We see that as the altitude increases, the worst-case magnetic field strength as well as the total worst-case torque decreases, thereby decreasing the required

dipole moment of the magnetorquer.We see that the required dipole moment at 350 km is $D = 0.6\,A - m^2$.However, data compiled from various magnetorquers from $D = 0.1\,A - m^2$ to $D = 5\,A - m^2$manufactured by ZARM Technik (taken from datasheets [84],[85],available online) which is one of the leading suppliers for attitude control equipment, shows that if we select a magnetorquer with $D = 1\,A - m^2$, we can reduce the power consumption with only a slight increase in mass,as shown below:

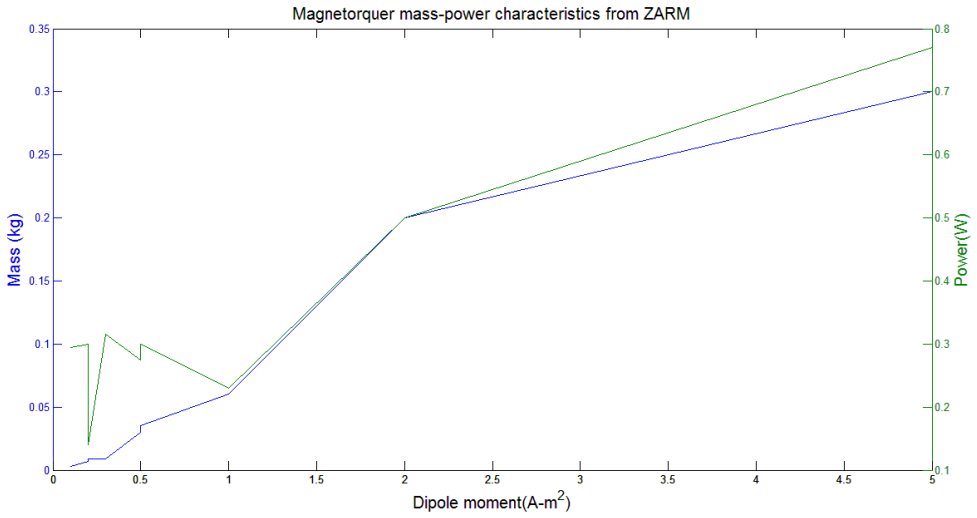

Figure 88: Magnetorquer mass-power characteristics from ZARM Technik

The chosen magnetorquer is the MT1-1 from ZARM Technik AG.

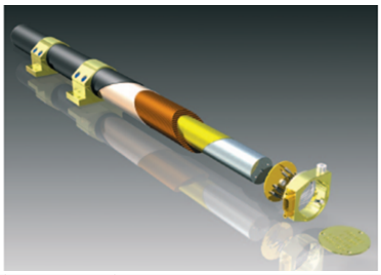

Mass(kg)	Power(W)	Dimensions
0.06	0.23	$Diameter = 135mm, Length = 132mm$

Figure 89: MT1-1, ZARM Technik specifications

7.5 Summary

Component	Component name	Manufacturer	Number	Mass(kg)	Power(W)
Reaction wheel	RW 35	Astro- und Feinwerktechnik Adlershof GmbH	3	1.5	9
Magnetorquer	MT1-1	ZARM Technik AG	3	0.18	0.69
TOTAL				1.7	9.69

Table 23: Attitude Control Subsystem budget

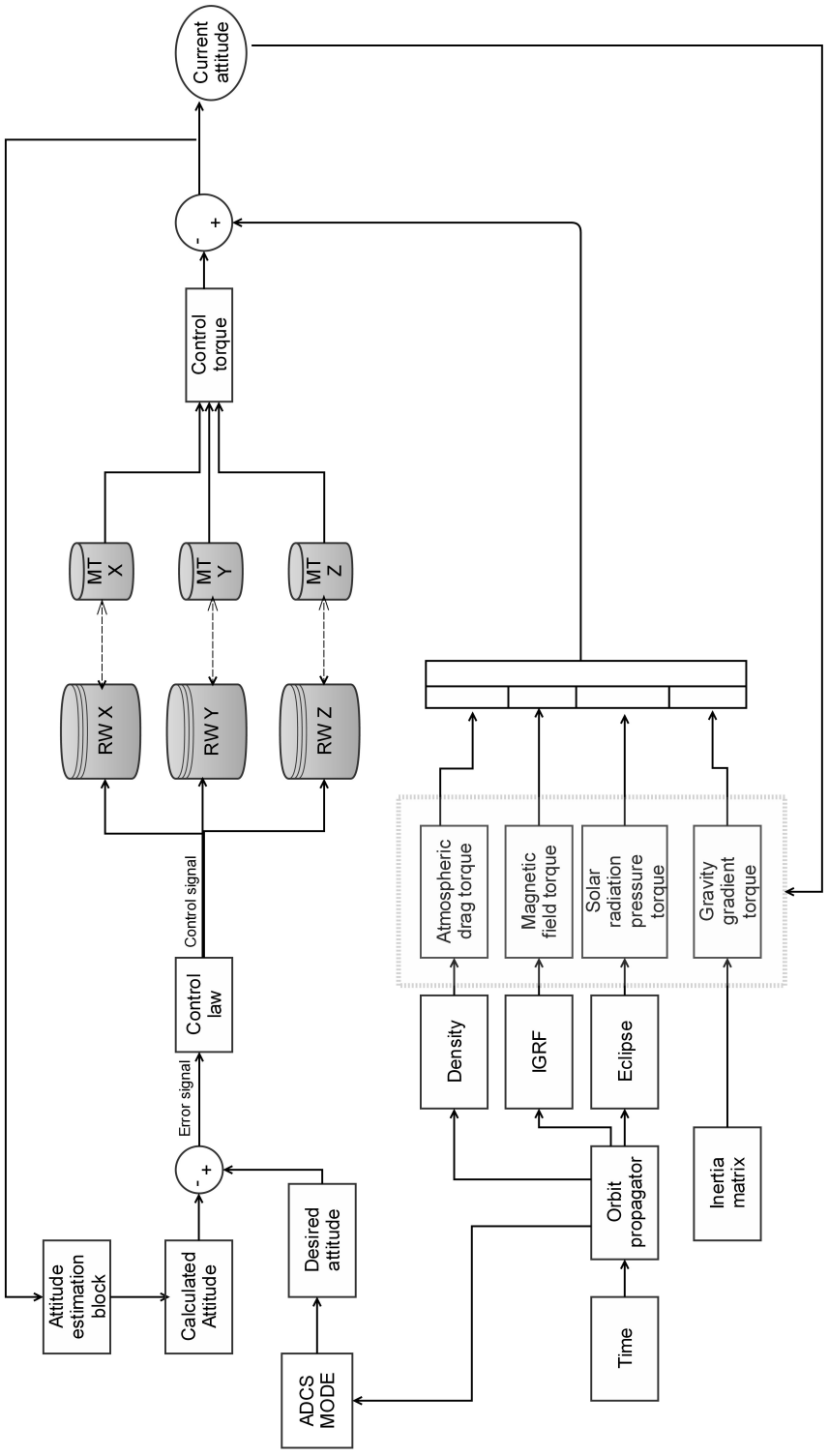

Figure 90: Attitude Control Subsystem schematic

Chapter 8

Attitude Kinematics and introduction to control theory

8.1 Effect of external disturbance torques on attitude motion

The equations that describe satellite dynamics are the well known Euler equations of motion. Two assumptions are made for the dynamic model: The body reference frame is assumed to coincide with the principal axes of the D3SAT body;the microsatellite acts as a rigid body. The Euler equations of motion are given by[35]:

$$I_{xx}\dot{\omega}_x + (I_{zz} - I_{yy})\omega_y\omega_z = \tau_x \tag{8.1.1}$$

$$I_{yy}\dot{\omega}_y + (I_{xx} - I_{zz})\omega_z\omega_x = \tau_y \tag{8.1.2}$$

$$I_{zz}\dot{\omega}_z + (I_{yy} - I_{xx})\omega_x\omega_y = \tau_z \tag{8.1.3}$$

τ_x, τ_y, τ_zrepresent the sum of external torques applied to the body.

The relation of the angular velocities to the orientation of the satellite is described by attitude kinematics. In atmospheric flight mechanics, the most common Euler angle set for describing vehicle orientations with respect to the origin the orbit reference frame is the 3-2-1 Euler angle sequence $(\psi, \theta, \phi)$with the notation the yaw, pitch, and roll angles(refer to section 3.2.2).

A common task encountered in attitude determination, but also arising in conversion from one attitude representation to another in dynamic analysis and synthesis applications, is extracting the Euler angles from the rotation matrix elements. As mentioned before,propagation of the orientation of an object is most

efficiently done with quaternions.Interested readers can refer to [30] for detailed definitions of methods to acquire the Euler angles from the rotation matrix using a wide range of Euler angle sequences, as well as for methods to acquire attitude information using quaternions. Once the the Euler angles have been extracted, the time evolution and description of the Euler angle rates as a function of the angular velocity vector components is of interest, since it is these rates which will determine the required control torques. From [86]:

$$\begin{bmatrix} \dot{\psi} \\ \dot{\theta} \\ \dot{\phi} \end{bmatrix} = \begin{bmatrix} 0 & \frac{sin\psi}{cos\theta} & \frac{cos\psi}{cos\theta} \\ 0 & cos\psi & -sin\psi \\ 1 & \frac{sin\psi sin\theta}{cos\theta} & \frac{cos\psi sin\theta}{cos\theta} \end{bmatrix} \begin{bmatrix} \omega_x \\ \omega_y \\ \omega_z \end{bmatrix} \tag{8.1.4}$$

We will see how the attitude motion evolves when there are no external torques acting upon the microsatellite. This is done by setting the right-hand side of equations 8.1.1 to 8.1.3 to zero, and then numerically integrating equations 8.1.1,8.1.2,8.1.3 and 8.1.4 using the MATLAB function *ode45*. Then, to see the effect what effect the external disturbance torques will have on the microsatellite attitude motion, the right hand side of the equations 8.1.1 to 8.1.3 are set equal to $\boldsymbol{\omega}_B + \boldsymbol{\omega}_a$(the most dominant disturbance torques which have been calculated in section 7.4.1). The initial conditions set are the same for both the cases.

Parameter	Value
ω_x	$1e-4\,rad/s$
ω_y	$2e-4\,rad/s$
ω_z	$3e-4\,rad/s$
ψ	$5°$
θ	$10°$
ϕ	$15°$

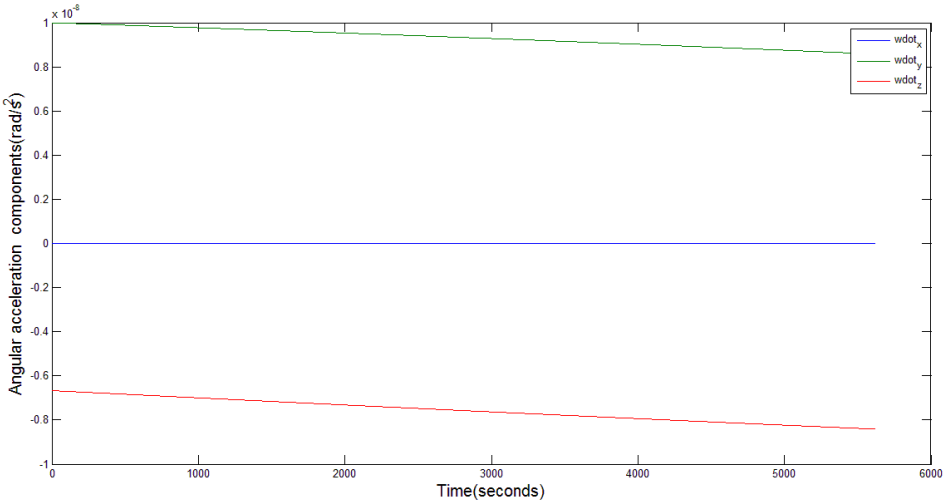

(a) $\tau = 0$

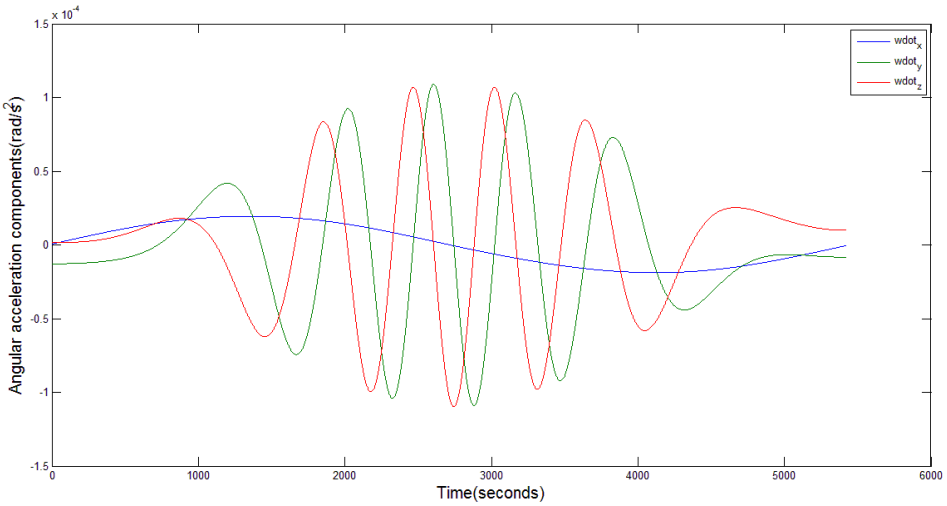

(b) $\tau = \tau_a + \tau_B$

Figure 91: Effect of τ_{ext} on angular acceleration

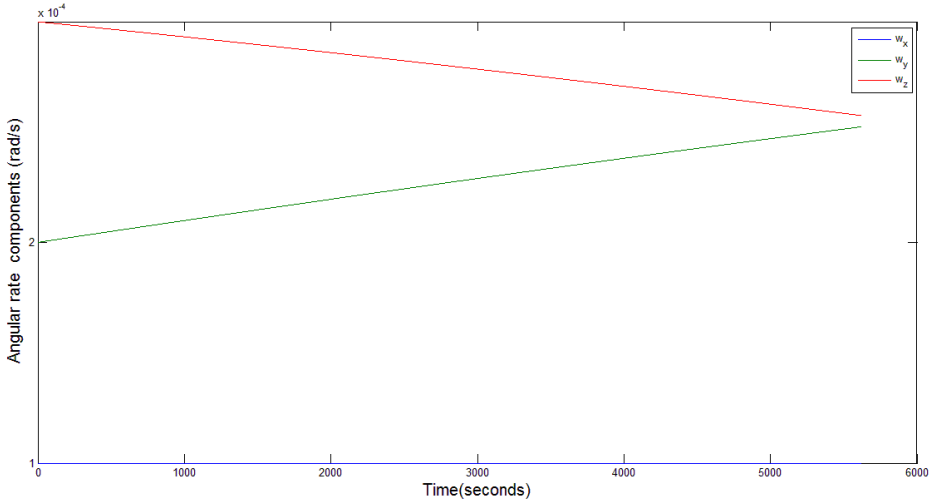

(a) $\tau = 0$

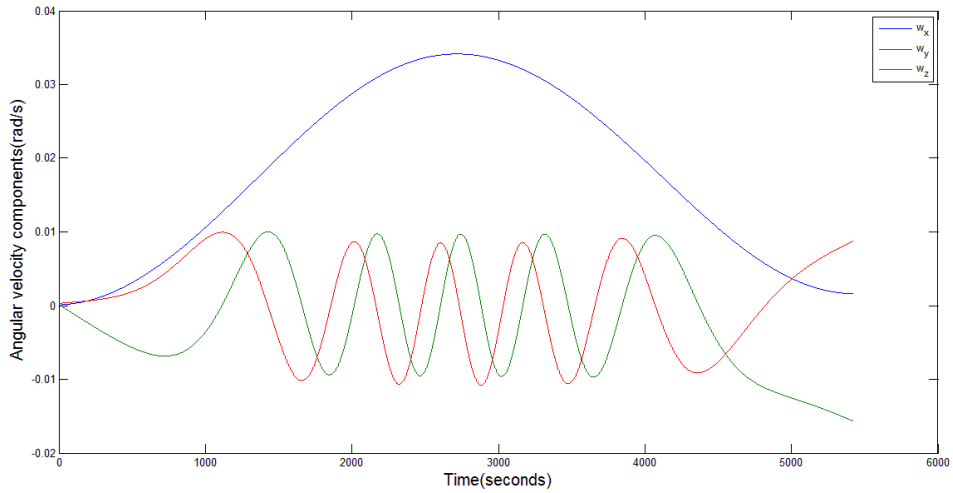

(b) $\tau = \tau_a + \tau_B$

Figure 92: Effect of τ_{ext}on angular rate

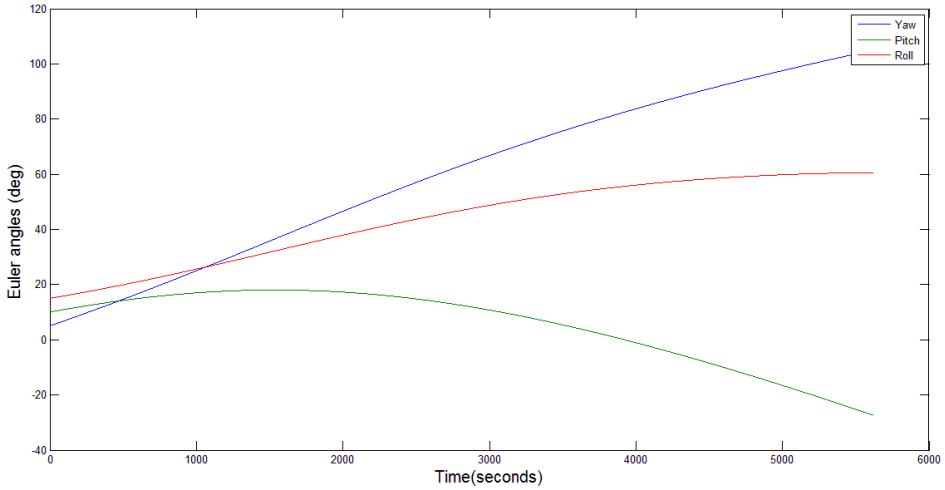

(a) $\tau = 0$

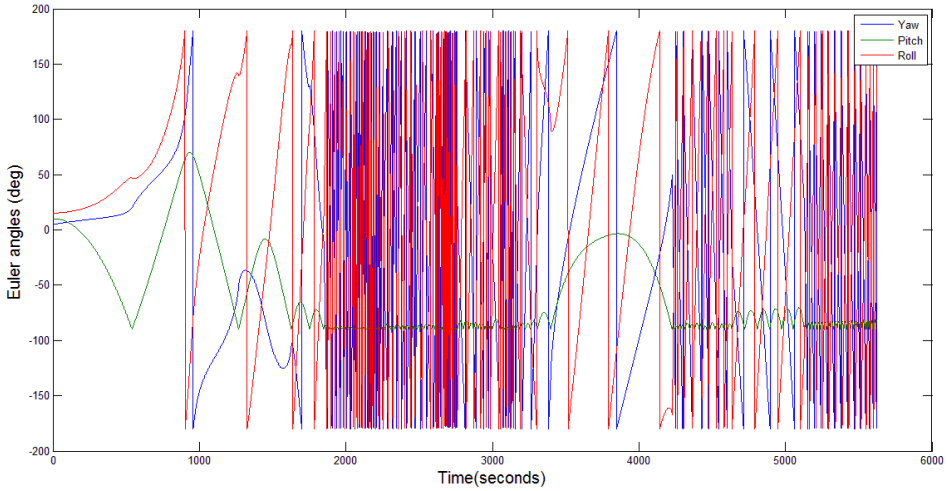

(b) $\tau = \tau_a + \tau_B$

Figure 93: Effect of τ_{ext} on Euler angles

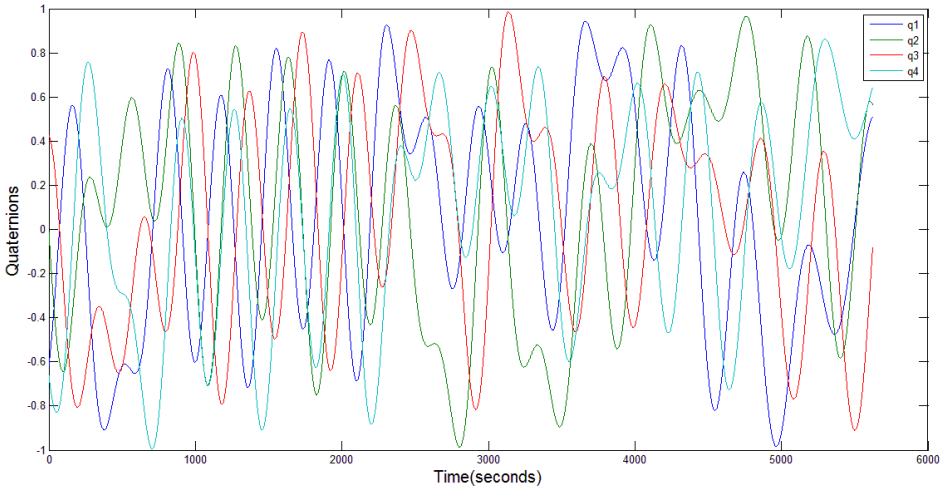

(a) $\tau = 0$

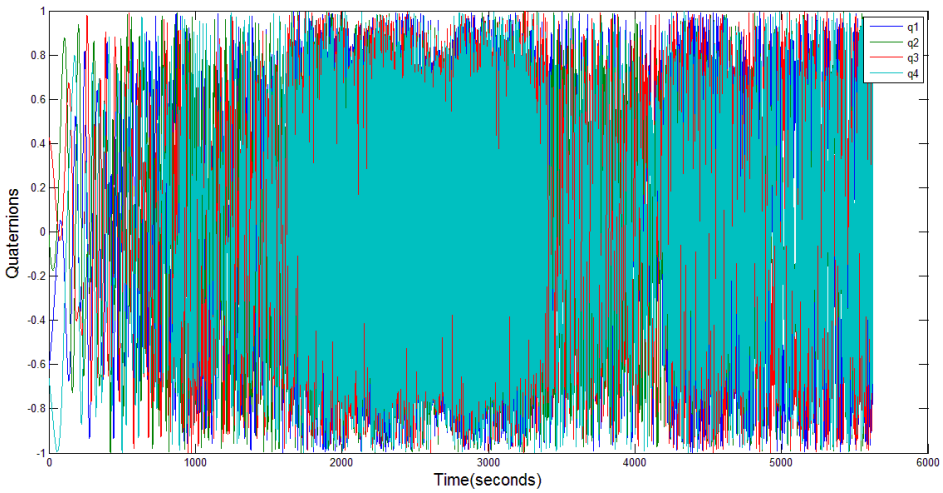

(b) $\tau = \tau_a + \tau_B$

Figure 94: Effect of τ_{ext} on quaternions

We can see what effect the external disturbance torques have on the attitude kinematics. The following section contains a brief introduction on how to implement the control torques necessary for attitude control .

8.2 Control theory

8.2.1 Modified Euler equations

Equations 8.1.1 to 8.1.3 are modified to include the reaction wheel terms and magnetorquer terms, adapted from [87] as:

$$I_{txx}\dot{\omega}_x + (I_{tzz} - I_{tyy})\omega_y\omega_z = \tau_x - I_{tyy}\omega_y\omega_{rwz} + I_{tzz}\omega_z\omega_{rwy} + \tau_{rwx} + \tau_{Cmx} \quad (8.2.1)$$

$$I_{tyy}\dot{\omega}_y + (I_{txx} - I_{tzz})\omega_z\omega_x = \tau_y + I_{txx}\omega_x\omega_{rwz} - I_{tzz}\omega_z\omega_{rwx} + \tau_{rwy} + \tau_{Cmy} \quad (8.2.2)$$

$$I_{tzz}\dot{\omega}_z + (I_{tyy} - I_{txx})\omega_x\omega_y = \tau_z - I_{txx}\omega_x\omega_y + I_{tyy}\omega_y\omega_{rwx} + \tau_{rwz} + \tau_{Cmz} \quad (8.2.3)$$

Where the moments of inertia of the reaction wheels have been added to the moments of inertia of the microsatellite.

$I_{txx} = I_{xx} + I_{rwx}, I_{tyy} = I_{yy} + I_{rwy}, I_{tzz} = I_{zz} + I_{rwz}$

Where $\tau_{Cmx}, \tau_{Cmy}, \tau_{Cmz}$ are the control torques applied by the magnetorquers, given in [88] as:

$$\begin{bmatrix} \tau_{Cmx} \\ \tau_{Cmy} \\ \tau_{Cmz} \end{bmatrix} = \begin{bmatrix} B_z D_y - B_y D_z \\ B_x D_z - B_z D_x \\ B_y D_z - B_x D_y \end{bmatrix} \quad (8.2.4)$$

Where $\vec{B} = \begin{bmatrix} B_x & B_y & B_z \end{bmatrix}$ is the geomagnetic field vector in the body frame and D_x, D_y, D_z are the magnetic dipole moments generated by the magnetorquer in the body frame.

$\boldsymbol{\tau_{rw}}$ are the control torques applied by the reaction wheels.

The equations 8.2.1 to 8.2.3 can be written (assuming $\boldsymbol{\tau_{cm} = 0}$) as:

$$\mathbf{I}\dot{\boldsymbol{\omega}} = \boldsymbol{\Omega}\mathbf{I}\boldsymbol{\omega} + \boldsymbol{\tau}_{\mathbf{rw}} \quad (8.2.5)$$

Where $\boldsymbol{\Omega} = \begin{bmatrix} 0 & -\omega_{rwz} & \omega_{rwy} \\ \omega_{rwz} & 0 & -\omega_{rwx} \\ -\omega_{rwy} & \omega_{rwx} & 0 \end{bmatrix}$

Using the assumption of rigid body dynamics, the mass moment of inertia of the system has a time rate of change of zero. It is standard to make this assumption

for satellites, and is a good approximation to first order. Of course, deployment of solar panels and rotation or translation of any components will shift the inertia. However, this motion is considered to be negligible .

8.2.2 Attitude error

Before implementing these control torques, it is necessary to study attitude error. Quaternions cannot simply be added or subtracted to find their sum or difference due to their unique definition, therefore quaternion multiplication is used. The difference in quaternion from the propagated estimate $\bar{\mathbf{q}}^{\ominus}$ to the measured quaternion $\bar{\mathbf{q}}_{\mathbf{m}}$ is the quaternion innovation, where quaternion multiplication of the inverse of the estimate represents a subtraction:

$$\delta\bar{\mathbf{q}} = \bar{\mathbf{q}}^{\ominus} \otimes \mathbf{q}_{\mathbf{m}}^{-\mathbf{1}}$$

Assuming that the estimated quaternion is very close to the measured quaternion, the following approximation can be made, where the scalar term is dropped and the vector terms of the innovation are doubled[89].

$$\delta\bar{\mathbf{q}} = \begin{bmatrix} 2q_1 \\ 2q_2 \\ 2q_3 \end{bmatrix}$$

After using an attitude estimation algorithm, the measured and filtered quaternion $\hat{\mathbf{q}}$ must be inverted and then quaternion multiplied by the commanded quaternion $\bar{\mathbf{q}}_{\mathbf{c}}$to get the innovation, as seen in the preceding equation. This gives the error $\bar{\mathbf{q}}_{\mathbf{e}} = \bar{\mathbf{q}}_{\mathbf{c}} \otimes \hat{\mathbf{q}}^{-\mathbf{1}}$.For small attitude changes, the error quaternion can be approximated as again as above. In fact, for small angles, this approximation of attitude error is equivalent to the traditional Euler angles:$2q_{e,1} = \phi$,$2q_{e,2} = \theta$,$2q_{e,3} = \phi$[89].

This approximation converts the calculated error in quaternion from a 4-dimensional term to a 3-dimensional term that can be used in a controller with a three-axis system.Referring to [90], the control torques are a combination of the non-linear dynamics of gyroscopic forces internal to the system introduced by spinning reaction wheels, a derivative feedback term, and a proportional feedback term:

$$\boldsymbol{\tau}_{\mathbf{rw}} = -\boldsymbol{\Omega}\mathbf{I}\omega - \mathbf{K}_{\mathbf{d}}\omega - \mathbf{K}_{\mathbf{p}}\bar{\mathbf{q}}_{\mathbf{e}}$$

where the torque due to gyroscopic forces is handled by $\boldsymbol{\Omega}$,the derivative term is simply a 3x3 constant gain matrix K_d multiplied by the measured angular rotation rate $\boldsymbol{\omega}$of the satellite. The proportional term is also a constant 3x3 gain matrix K_p multiplied by the measured attitude error $\bar{\mathbf{q}}_\mathbf{e}$.

As the angular rotation rates and the quaternion error, and inertia are all measured or fixed by the response of the system, the control gains K_d, $K_p$have to be defined to best perform the eigenaxis rotation and ensure stability. According to[90], and as confirmed by [91], the gain terms should be scalar multiples of the inertia matrix $\mathbf{I}$. This matter of control systems is out of the scope of this thesis, and is the next step for future work.

While this kind of control law can easily achieve closed loop stability, a straightforward analysis shows that the effect of a constant external disturbance torque, the compensation of which requires the application of a constant control torque, causes the wheels velocities to increase linearly, until saturation is eventually reached. To compensate for this effect, an additional control loop is introduced, to deal with wheel momentum management issues.

8.3 Momentum dumping

The idea is that the continuous compensation of the effect of (small) secular torques on the reaction wheels should lead to small side effects on the pointing and stability performance of the actual attitude control system.The momentum control loop and the attitude control loop can be treated independently. Such an engineering approximation is entirely justified by the wide frequency separation between the attitude control loop (time response of the order of seconds/minutes) and the momentum control loop (time response of the order of minutes, possibly hours)[92, 93].

We can write the time varying momentum of the reaction wheels as:

$$\mathbf{h_{rw}(t)} = \mathbf{I\Omega(t)}$$

The goal of the momentum control loop is to maintain such momentum near zero without interfering with the attitude control loop, that is, the momentum control loop must have a considerably slower response with respect to the attitude control loop. As a preliminary step, we first identify the basic problem, which

is to apply proportional momentum feedback using the torques generate by the magnetorquers.[94, 95]:

$$\boldsymbol{\tau}_{\mathbf{Cm}}(t) = -\mathbf{K}\mathbf{h}_{\mathbf{rw}}(t) \tag{8.3.1}$$

From equation 8.2.4, the torque generated by the magnetorquers can be written as:

$$\boldsymbol{\tau}_{\mathbf{Cm}}(t) = \mathbf{D}(t) \wedge \mathbf{B}(t) \tag{8.3.2}$$

Equating the equations 8.3.1 and 8.3.2 , we have:

$$-\mathbf{K}\mathbf{h}_{\mathbf{rw}}(t) = \mathbf{D}(t) \wedge \mathbf{B}(t) \tag{8.3.3}$$

As we can see, the control input is $\mathbf{D}(t)$, and in order to get a value for this, it is necessary to constrain the resulting torque to be normal to the magnetic field vector. Therefore, left multiplying both sides of the above equation by $\mathbf{B}(t)$[92], we get resulting magnetic dipole to be applied to the magnetorquer, and the resulting torque :

$$\mathbf{D}(t) = -\frac{\mathbf{K}}{\mathbf{B^2}}[\mathbf{B}(t) \wedge \mathbf{h}_{\mathbf{rw}}(t)] \tag{8.3.4}$$

$$\boldsymbol{\tau}_{\mathbf{cm}}(t) = -\frac{\mathbf{K}}{\mathbf{B^2}}[\mathbf{B^2}\mathbf{h}_{\mathbf{rw}}(t)] - \mathbf{B}(t)[\mathbf{B}(t) \cdot \mathbf{h}_{\mathbf{rw}}(t)] \tag{8.3.5}$$

The second term in the RHS of the equation 8.3.5 is the projection of vector $\mathbf{h}_{\mathbf{rw}}$ along the direction of $\mathbf{B}$.Therefore,for simplicity, the above equation can be rewritten as:

$$\boldsymbol{\tau}_{\mathbf{cm}}(t) = -\mathbf{K}\mathbf{h}_{\mathbf{rw}}(t) + \mathbf{K}\mathbf{h}_{\mathbf{rw/B}}(t) \tag{8.3.6}$$

Where the second term indicates the projection of reaction wheel vector along the direction of $\mathbf{B}$. Therefore, if $\mathbf{h}_{\mathbf{rw}} \not\perp \mathbf{B}$, there will always be some difference between the desired control torque and the applied control torque. In addition to this drawback , the choice of the gain $\mathbf{K}$ has to be largely based on trial and error through simulations. Therefore, there exist in literature, other optimal controllers which is out of the scope of this thesis. This is a recommendation for future work.

Chapter 9

Mode details

9.1 Detumbling

The angular rate can be reduced by either using the magnetorquers or by using the reaction wheels. The reaction wheels will of course, result in faster detumbling. However, we choose not to use the reaction wheels for this detumbling mode primarily due to two reasons:

1)When the satellite is released, the wheel is still at rest and must be brought to some initial speed in order to be able to create the necessary torques.

2)The power consumption by the reaction wheels can be an issue.

The use of magnetorquers for the detumbling phase prevents the above mentioned complications related to use of the reaction wheels.

The task is now to reduce this initial movement rapidly after the release in order that the satellite can begin to work. It's usually only needed in the first mission phase and deactivated afterwards. Then another control system part takes over to stabilize the orbit and orientate the satellite such that the instruments can work properly. This other control system part differs from the detumbling as it's aim is not to stop any movement but to make some controlled movements to set up the desired attitude. It may be necessary to reactivate the detumbling controller also in later parts of the satellite's life if the angular rates came to again be too high for the attitude controller. Before zeroing in on a detumbling method, we first study a few commonly used detumbling techniques, depending on the sensor used for feedback.

1)Magnetometer feedback

1.1)Bdot control

The idea is to use the magnetometer measurements of the earth's magnetic field as feedback source. If the measured magnetic flux density does not change with time any more, the satellite is not spinning around longer. The rate of change of the magnetic flux density, i.e. the time derivative, is notated $\dot{\mathbf{B}}$, hence the name. The control law for the magnetic dipole moment is very easy and straightforward.

$$\mathbf{D} = -k\dot{\mathbf{B}}$$

Observations of how the magnetic field changes as a function of time are used in a simple but powerful way to mitigate tumbling, called B-dot control. This consists of simply applying a torque in the opposing direction that matches the rate of change of the magnetic field. The rate of change of the magnetic field $\dot{\mathbf{B}}$(t)can be sensed by the angular rotation of the satellite $\omega(t)$ crossed with the instantaneous magnetic field vector $\mathbf{B}(t)$. The dipole that is desired to be applied by the torque rods in order to damp out this rotation is represented by **D**, where it is simply proportionally related by some selected gain k applied to that observed rate of change. Thus, the control torque that results is the cross product of that dipole with the magnetic field. This dipole that effects the torque is applied by magnetorquers.

$$\boldsymbol{\tau}_{\mathbf{cm}} = \mathbf{S}(\mathbf{D})\mathbf{B}$$

where **B** is the flux density vector of the earth's magnetic field and **D** is the magnetic dipole moment and in case of the magnetorquers, the control variable.

Sis the cross-product operator as defined in [96]to have an ordinary matrix multiplication.

$$\boldsymbol{\tau}_{\mathbf{cm}} = \mathbf{S}(-\mathbf{k}\dot{\mathbf{B}})\mathbf{B}$$

This torque will result in damping the angular velocity

1.2)Bang-bang control

This controller is a modification of the $\dot{\mathbf{B}}$ controller. Instead of calculating a dipole moment that is proportional to $\dot{\mathbf{B}}$, the maximum value acting against the rotation is always used, i.e. magnetorquers are always working at their maximum dipole moment.

$$\mathbf{D} = -D_{max} sgn(\dot{\mathbf{B}}) \tag{9.1.1}$$

According to [97]this bang-bang controller is theoretically able to perform detumbling operation much faster.

2)Gyroscope feedback

Another detumbling technique is to directly measure ω_{BF}^{RTN} with the gyroscopes and this measurement for reduction of angular velocity instead of $\dot{\mathbf{B}}$.

$$\boldsymbol{\tau}_{Cm} = \mathbf{S}(-k\omega_{BF}^{RTN})\mathbf{B}$$

However, as suggested by [98] ,this will not be a working detumbling controller.

3)Sun sensor feedback

The ability to reduce the tumbling based on information from the sun sensor is low because the satellite's motion may be too fast to detect the sun. This feedback method will also fail when the sun is hidden behind the earth. Another possible issue which can arise the intensity of mathematical computations required.

We see that the use of magnetometer for feedback will greatly simplify detumbling. No prior information is needed about the angular velocity of the microsatellite, since the instantaneous rate of change of the magnetic field $\dot{\mathbf{B}}$can be estimated by on-board measurements. This is a robust and fail-safe system which does not depend on operation of complex systems like attitude estimation filters.

A rough analysis of the time taken for detumbling is carried out from[99]:

The momentum dumped per orbit:

$$M_D = D_{available} \times B \times T$$

$D_{available}$= the maximum dipole strength of the selected magnetorquers

$$\therefore H = I\omega \text{ [N-m-s]}$$

$$\therefore \text{Time required for detumbling} = \frac{H}{M_D} \times T \text{ [sec]}$$

This above formula will give the approximate theoretical value required to get the final angular rate to 0. **B** field values are chosen as the lowest of the geomagnetic field vector values, because for a magnetorquers τ_{Cm} is given from equation 8.2.4,and therefore assuming that B is low, will mean that the produced torque will also be low and we can get worst-case idea for detumbling time.

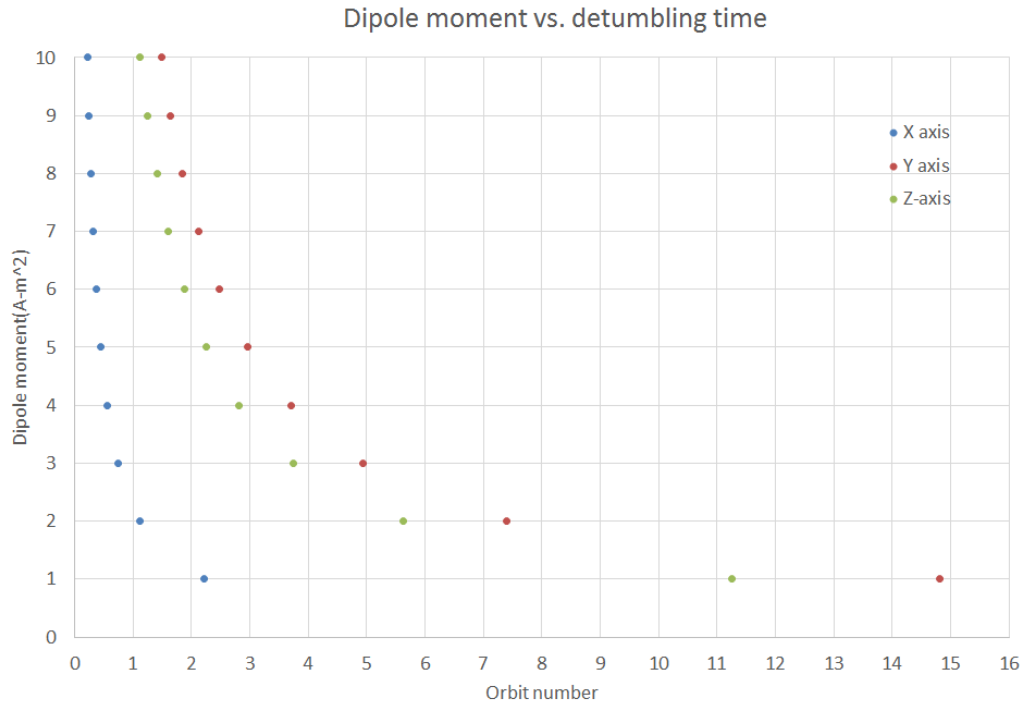

Figure 95: Detumbling time as a function of dipole moment

We see that for our chosen magnetorquer, detumbling will take almost 1 day along y-axis.Therefore to fulfill REQ A from table 17, we choose D=5 A-m^2.The earlier choice of magnetorquer is changed to MT5-2.

Mass(kg)	Power(W)	Dimensions
0.3	0.77	$Diameter = 18mm, Length = 240mm$

Figure 96: MT5-2 ,ZARM Technik specifications

The above detumbling has been calculated using lowest **B** all the time.Since this is not case ,we will use equation 9.1.1, and solve Euler's equations 8.1.1 to 8.1.4 with the magnetic field profile as calculated in figure83, with the initial conditions $\omega = \begin{bmatrix} 0.15 & 0.15 & 0.15 \end{bmatrix}^T$ (rad/s) and $\psi, \theta, \phi = 0$.

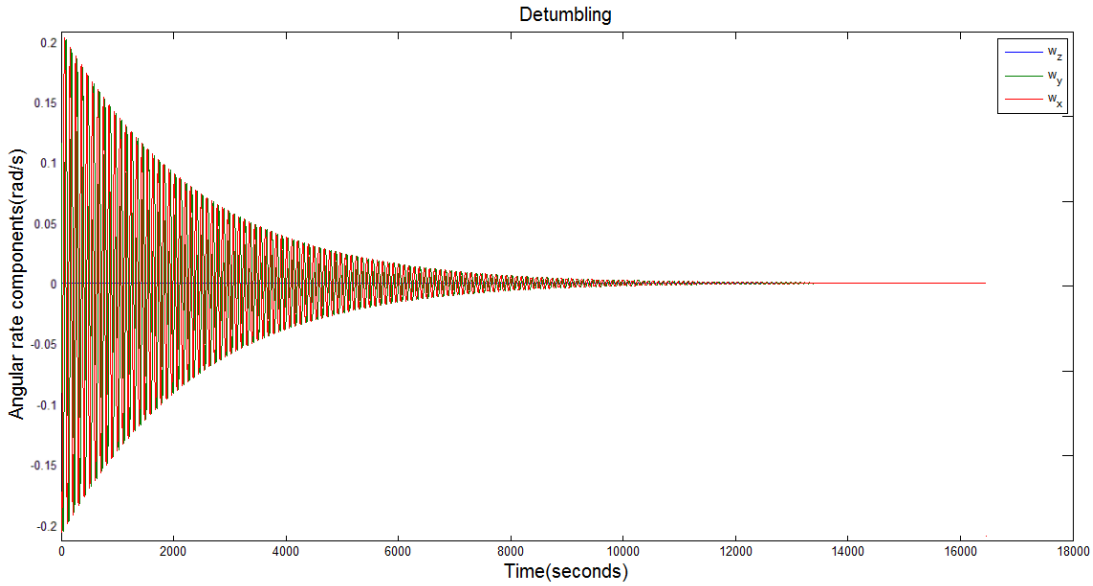

Figure 97: Detumbling using bang-bang control

We can see that detumbling will take place well within 3 orbits,that is, 3.47 hours, or, 2.3 orbits, therefore satisfying REQ A from table 17. The only disadvantage is that this control method will not work efficiently in equatorial or nearly-equatorial orbits, since the magnitude of $\dot{\mathbf{B}}$will be very small for most of the time.

9.2 Initial Attitude Acquisition

After detumbling, the sun sensors will be used to detect the sun vector, so that solar panels can be deployed. We have chose the BASS 17 from EADS Astrium for IAA (refer to section 6.2.4). The value of slope angle is 17°.

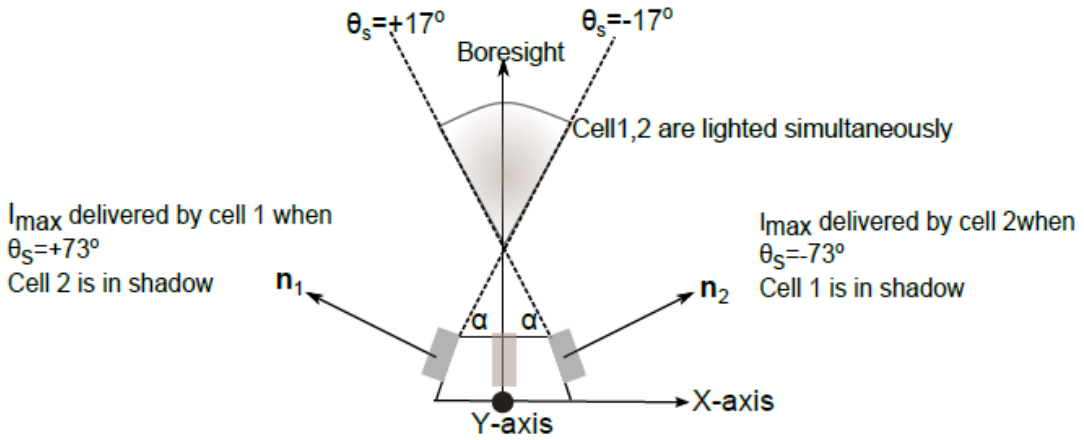

Figure 98: BASS 17,EADS Astrium

We have chosen to put on two faces Z+ and Y-. The sun vector will be determined according to the following algorithm:

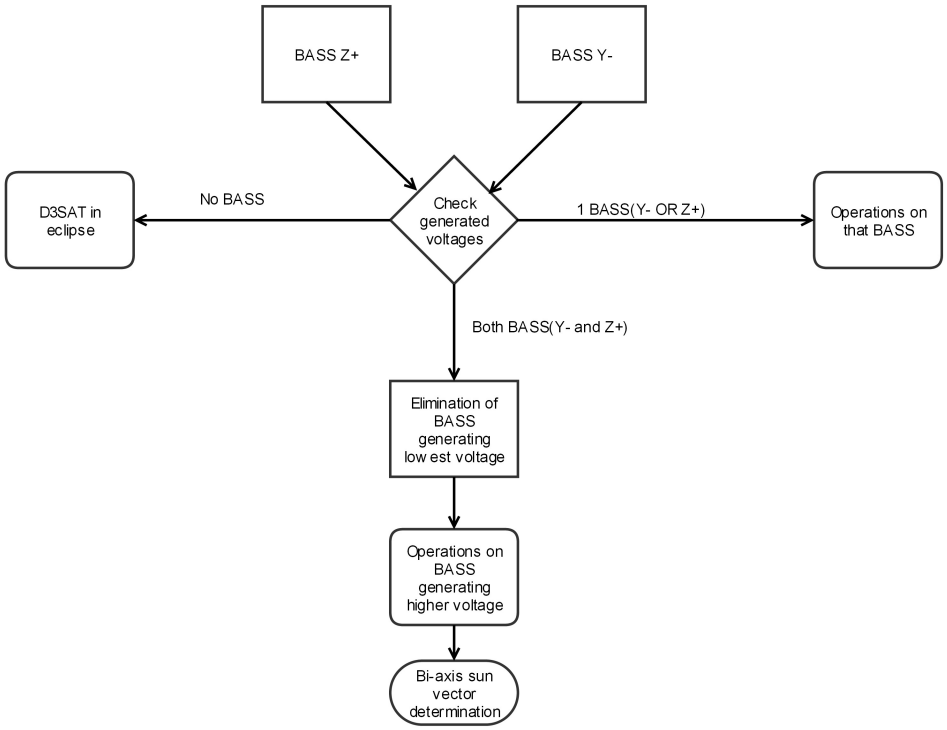

Figure 99: IAA algorithm

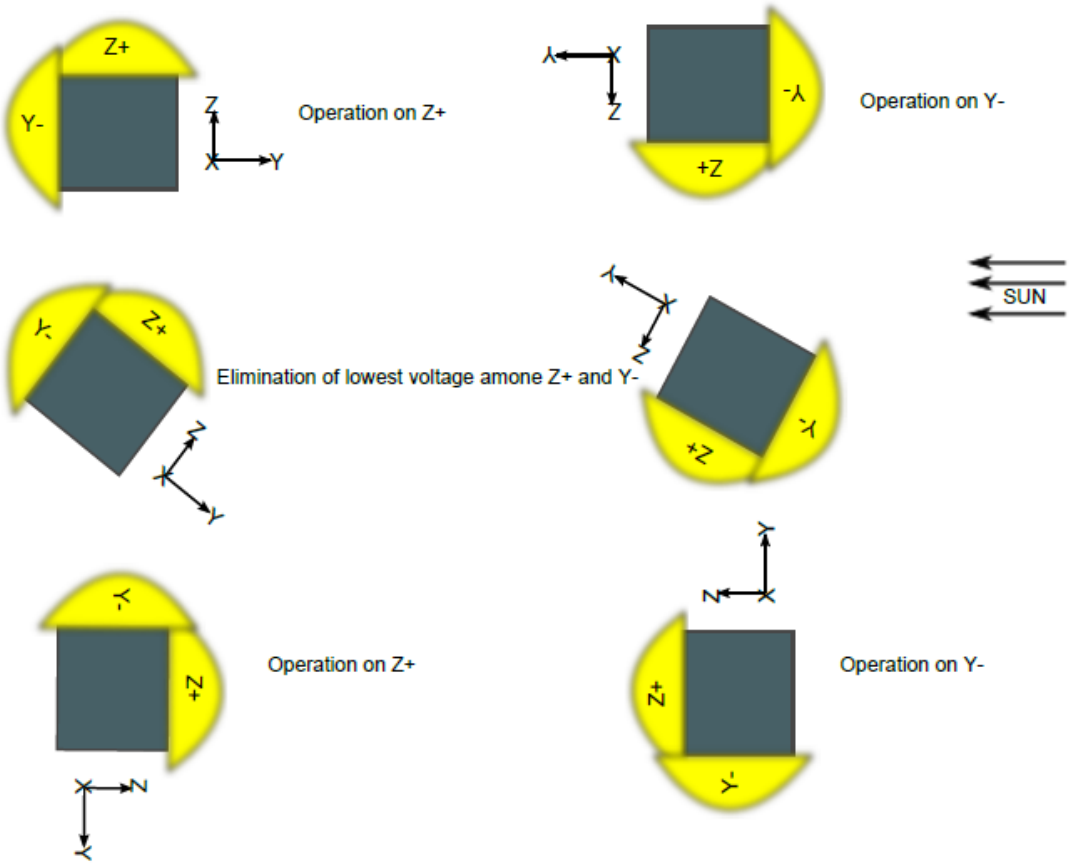

Figure 100: IAA algorithm diagram

At the end of this mode, the solar panel will be deployed, and the main mission mode will start. If the need arises this mode can also be used for coarse sun pointing, in order to point the solar array area towards the sun.

9.3 Normal

During this mode, the reaction wheels will reject external torques and desaturation of reaction wheels, if needed will be done by magnetotorquers. Extensive housekeeping data will be collected and stored on the OBC.

9.4 HT-firing

This mode occurs for drag compensation and at the end of the mission, for deorbiting. From section 4.2.4, to mantain the altitude within 150 meters of the

nominal value of 350 km, firing shall take place every 3rd orbit, just after coming out of the eclipse. For deorbiting, the microsatellite will have to yawed by 180 degrees so that retro-firing of the thruster can take place. The time taken for this maneuver depends on the operating point of the reaction wheels. This slew torque is given as[39]:

$$T_y = 4\theta I_y / t^2 \tag{9.4.1}$$

Where t is the maneuver time in seconds.

Assuming no resisting momentum, and maximum acceleration , the total momentum change for the wheel during the slew is given by[39] as:

$$M_y = T_y \frac{t}{2} \tag{9.4.2}$$

We plot the torque and angular momentum stored in the reaction wheel as a function of maneuver time:

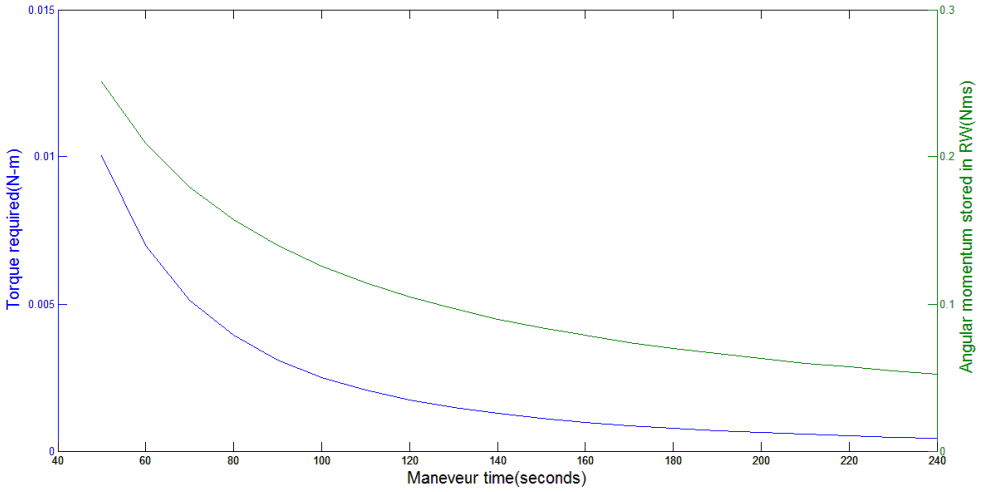

Figure 101: Yaw maneuver time for deorbiting

We need to choose a value such that the angular momentum storage of the reaction wheel is not exceeded, so that there is no need for momentum dumping. We can see that the maneuver time will be between 140 to 180 seconds for an operating torque level of about 0.001282 Nm. Therefore, if we operate at this constant torque, angular momentum built up in the reaction wheels will be 0.08976

Nms, which is below the maximum angular momentum storage capacity of the selected reaction wheels. Some margin also has to be considered since during this yaw maneuver, even the external disturbance torques will be acting on the D3SAT.

9.5 Slew

In section 5.2.5, the pointing rate of the satellite was derived for maximum time in view of the ground station. However, for a worst case analysis to verify if the ADCS can work effectively during the slew mode, we analyze the satellite visibility times per day using STK, and we use the mean value of visibility time to make a more detailed analysis.

We assume that data will be transmitted only once a day, since this will impose the most stringent requirements from the ADCS. We assume that the time available for the slew maneuver equals the ground station visibility time minus time required to transmit all the data i.e. slew and data transmission do not take place simultaneously. The data collected(data to be transmitted =136 MB at a transmission speed of 380 kbps, from [46]). To transmit the data, we assume that the D3SAT has to be slewed around the roll axis by 180°,since the antenna is placed on the X+ face. Fixing this data, we see that the mean visibility time per pass changes with altitude, and therefore the pointing rate to be provided by the ADCS will also change. The below figure shows the required performance of the ADCS as a function of altitude.

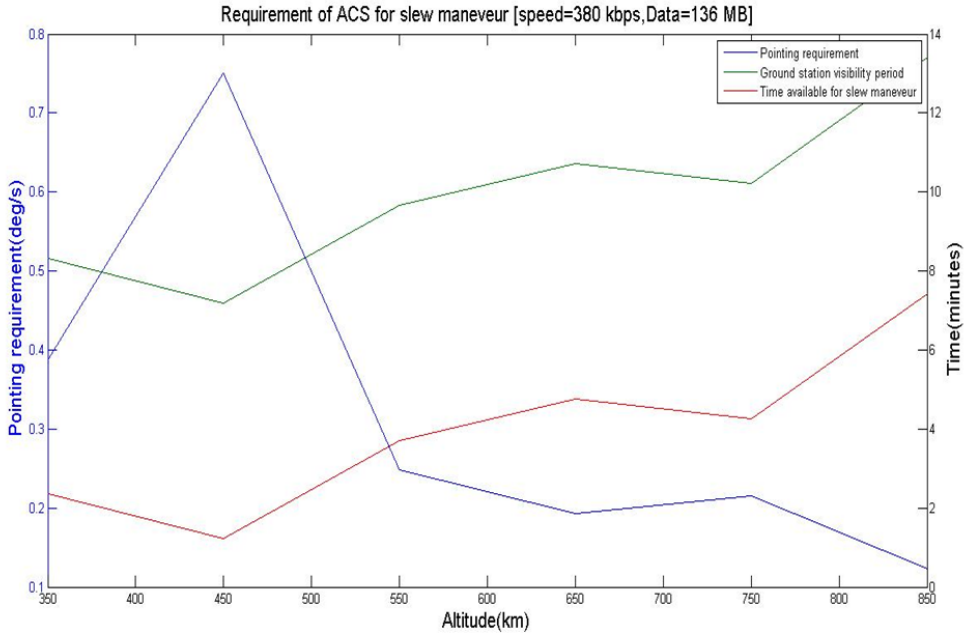

Figure 102: Pointing rate as a function of altitude

Based on the angular momentum storage of the reaction wheels, we can impose a limit on the maximum amount of data that can be transmitted during one ground station pass.

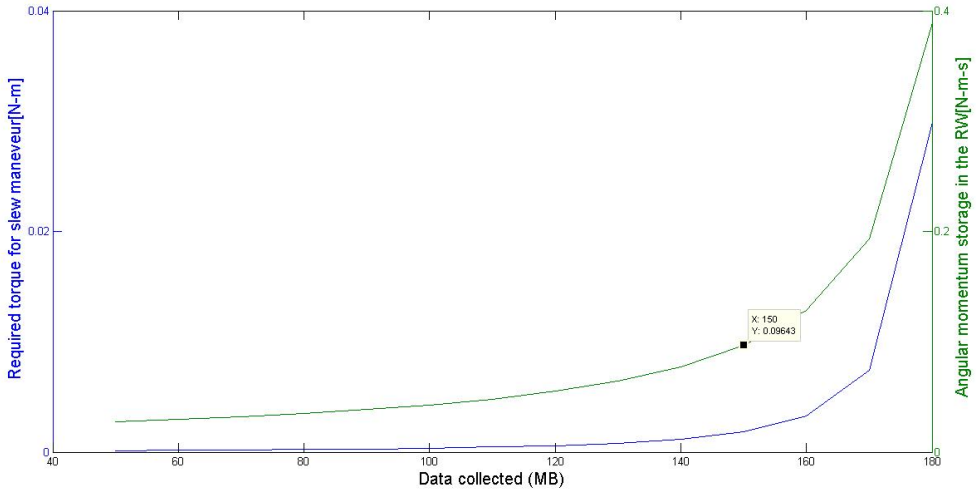

Figure 103: Transmitted data limit based on angular momentum capacity of RW's

From the above figure, we can see that if the data to be transmitted exceeds 150

MB, the momentum built up in the reaction wheel will approach the maximum angular momentum storage capacity of 0.1 N-m-s. Therefore to be on the safe side, we decide that the maximum data that can be transmitted during one downlink session is 150 MB.

Within Slew Mode, the satellite employs its reaction wheel set to apply the control torque, causing the bus of the satellite to rotate. The magnetorquers are also used throughout Slew Mode in order to help dump excess momentum that may be introduced to the system by disturbances. During this mode, information about the next ground pass is uploaded to the OBC from the ground station. For improved accuracy and also to reduce burden on the OBC, this information is not stored on the computer.

9.6 Mode transition scheme

After release from the launch vehicle, the Detumbling mode will be activated. At the end of Detumbling , the Initial Attitude Acquisition mode will commence, at the end of which the solar panel will be deployed. After acquiring attitude information, the Normal mode will start based on a command given by either the OBC or the ground station.HT-Firing will then automatically occur for drag compensation for the 6 months, and after, for the deorbiting phase. During each Slew mode, information about the next ground pass is uploaded to the OBC from the ground station, so the Slew mode is commanded either from the OBC or ground station, after which the Normal mode is again activated. The Detumbling mode acts as the emergency mode, and if the angular rate of the D3SAT becomes too high for the on-board controllers to handle, the Detumbling mode can again be activated.This transition scheme is shown below:

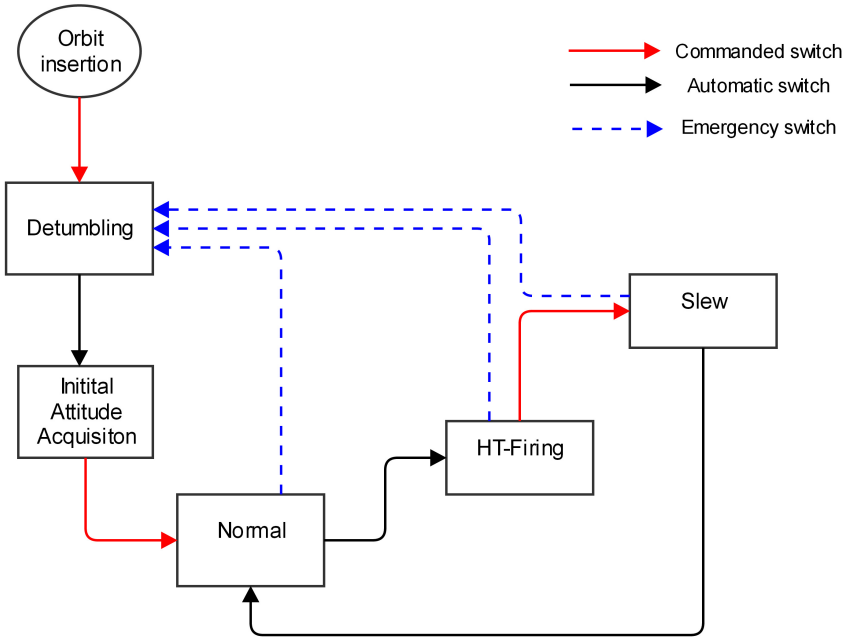

Figure 104: Mode transition scheme

Assuming an altitude of 350 km, and reference case 1 for drag compensation: the daily profile will look like this:thick white lines represent ground station visibility times. RED lines are the HT-firings pulses for drag compensation mode, which occurs when not in eclipse in, orbits 3, 6, 9, 12, 15. Data will be transmitted once a day in orbit 9, and so the purple PURPLE line represents Slew mode.

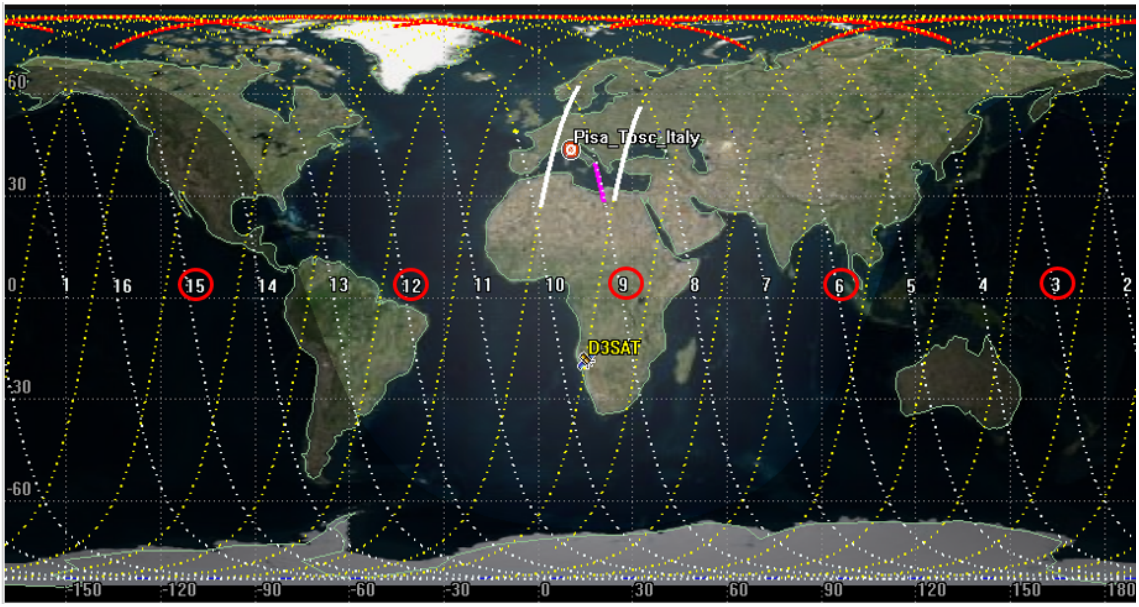

Figure 105: Daily mode transition scheme for drag compensation

Chapter 10

Conclusions and Future Work

The aim of this thesis was to design a mission for the in-orbit demonstration of the HT-100D.The important operations required to completely evaluate the performance of this low power, low mass thruster, namely drag compensation and end-of-life deorbiting, were analyzed. These operations were shortlisted to be executed, since they are important for small satellites in Low Earth orbit. It was found that a wide range of mission scenarios which can demonstrate the effective operation of the HT-100D can be accomplished with low propellant mass carried on-board, even if the launch vehicle releases the D3SAT at a high altitude. The HT-100D is found to be an effective propulsion system to broaden the range of missions capable of being carried out by small satellites. Due to the modular architecture of this propulsion system, it can be easily installed on small satellites and can respond rapidly to market needs.

The firing time and propellant requirements calculated during the period of solar maximum was compared to to the requirements calculated using the NRLMSISE-00 model (with high long term solar and geomagnetic activity). The requirements obtained using the NRLMSISE-00 model were 40 % lower than those obtained using the solar maximum density model. Therefore, the propellant carried on-board will be based on the worst-case scenario of solar maximum density, thereby ensuring sufficient propellant in case the drag compensation and deorbiting strategies are changed in the future. In case the D3SAT is released at a higher altitude, an extra 16 days and 0.7 kg of propellant is added to the mission to perform an orbit lowering maneveur to an altitude where the drag compensation mission can be meaningful. The mission analysis study which was carried out in this thesis will enable knowledge of propellant and transfer time requirements for any strategy that will be decided upon in the future. The reference cases that were

analyzed for drag compensation and deorbiting were extreme cases which will demand the maximum propellant and HT-100D firing time.

The required functions of the Attitude Determination and Control Subsystem in order to support the mission were analyzed, and phases of the ADCS were defined. The mode-specific requirements of the ADCS were derived, and the preliminary sizing and specification of the ADCS components were done to fulfill these requirements. The use of two pyramidal sun sensors for Initial Attitude Acquisition will ensure that the mission can commence less than an hour after the Detumbling mode is complete. The final selection of the magnetorquer was to fulfill the self-imposed requirement of detumbling within three orbits, and the magnetorquer can be changed in case this detumbling time requirement is decided to be relaxed. The use of reaction wheels over control moment gyros is justifiable, owing to the appreciable mass and power savings obtained by use of reaction wheels. All the sizing was done using worst-case conditions, which will ensure the adaptability of the ADCS to function at different orbital parameters (which will ultimately depend on the launch vehicle available for piggyback launch). Commercial-off-the-shelf components were chosen to reduce the overall mission cost and lead time, and as we can see from the table 24, the ADCS has a high performance at a low power consumption and with a low mass, which is the most important factor due to the limited on-board power and low volume available on small satellites. The interaction of the ADCS with other subsystems was studied, so that any possible future changes in this subsystem can be related to changes in the other subsystems of the D3SAT.

Component	Component name	Manufacturer	Number	Mass(kg)	Power(W)
Magnetometer	3-axis Fluxgate Magnetometer	Surrey Satellite Technology Ltd.	1	0.19	0.3
Inertial Measurement Unit	STIM300	Sensonor	1	0.05	1.5
GPS receiver +antenna	SGR-05P	Surrey Satellite Technology Ltd.	1	0.1	1
Pyramidal Sun Sensor	BASS17	EADS Astrium	2	0.65	-
Reaction wheel	RW 35	Astro- und Feinwerktechnik Adlershof GmbH	3	1.5	9
Magnetorquer	MT5-2	ZARM Technik AG	3	0.9	2.31
TOTAL				3.4 kg	13.8 W

Table 24: Final ADCS mass and power budget

The next step for future work is the platform design of the D3SAT, keeping in mind the mass should be 40 kg and the dimensions should be $40 \times 40 \times 40\, cm^3$. With respect to the components of the ADCS, some recommendations are given regarding their placement on the D3SAT platform: the magnetorquers must be located at a sufficient distance from high magnetic field components and must not be located very close to the magnetometer, since this might cause magnetic interference. The correct choice of attitude determination algorithms for the different ADCS modes must be studied and decided upon. The three reaction wheels in orthonormal axes must be located as close to the center of mass as possible. An interesting work to reduce the mass and power requirements of the reaction wheels would be to analyze pyramid-like configuration of the reaction wheels, so that the same performance can be obtained but by using smaller reaction wheels, thus optimizing mass and power consumption. The Inertial Measurement Unit must be safe from distortions like thermal effects and vibrations,which are most prominent during launch. The IMU can be placed on a bracket on the

side wall,however,mounting on the wall might lead to reduced accuracy and so placing on the base plate is a good idea. The residual dipole moment of the D3SAT can be approximated more accurately, by studying the magnetic interaction between the different components on-board, and more importantly, interaction of the components with the magnetic circuit of the HT-100D. The thermal interactions of the HT-100D with the main D3SAT subsystems is a recommendation for future work. Another recommendation is to analyze the prospect of manufacturing the pyramidal sun sensor in-house. The attitude control gains must also be analyzed and determined, and it is recommended that the first step for future work should be on the attitude control system.

In conclusion, the D3SAT technology demonstration mission is found to be feasible and the ADCS is found to be suitable for the low power and low mass requirements of small satellites. This mission can effectively qualify the HT-100D and can broaden the range of missions capable of being carried out by small satellites.

Bibliography

[1] M. E. Buchen and M. D. DePasquale, *Nano/Microsatellite Market Assessment*. Atlanta, GA: SpaceWorks Enterprises, Inc. (SEI), 2014.

[2] H. Klinkrad, *Space Debris Models and Risk Analysis*. Praxis Publishing Ltd., 2006.

[3] M. D. DePasquale, M. Charania, M. Seiji Matsuda, and M. Hideki Kanayama, *Analysis of the Earth-to-Orbit Launch Market for Nano and Microsatellites*. Anaheim, CA: AIAA Space 2010 Conference and Exposition, 2010.

[4] M. DePasquale and Dr. John Bradford, *Nano/Microsatellite Market Assessment*. SpaceWorks Enterprises Inc.(SEI): SpaceWorks, February 2013.

[5] A. Papa, *A Versatile Constellation of Microsatellites with Electric Propulsion for Earth Observation:Mission Analysis and Platform Design,Master thesis*. Pisa: University of Pisa, 2013-2014.

[6] D. C., Oslyak S., Dignani D., Albertoni R., and Andrenucci M., *HT-100D Performance Evaluation and Endurance Test Results*. The George Washington University, USA: The 33rd International Electric Propulsion Conference, 2013.

[7] K. G., Fritsche B., and Lips T., *Survivability and Ground-Risk Potential of Screws and Bolts of Disintegrating Spacecraft During Uncontrolled Re-Entry*. Darmstadt, Germany: Proceedings of the Third European Conference on Space Debris, 2001.

[8] accessed on :14/10/15, "http://www.geomag.bgs.ac.uk/,"

[9] M. M. Moe, Steven D. Wallace, and Kenneth Moe, *Improved Satellite Drag Coefficient Calculations from Orbital Measurements of Energy Accomodation*. Los Angeles,California: Journal of Spacecraft and Rockets(Vol. 35, No. 3, pp. 266-272).

[10] R. Vottel and Doug Sinclair, *A Comparision of CMGs and Reaction Wheels for Small Earth-observing Satellites*. 26th Annual AIAA/USU Conference on Small Satellites.

[11] I. Kosmotras, *Space Launch Systems :DNEPR User's Guide*.

[12] Mission Design Division Staff, *Small Spacecraft Technology State of Art*. Ames Research Center,Moffett Field,California: NASA/TP-2014-216648, February 2014.

[13] M.Rycroft and N.Crosby, *Smaller Satellites:Bigger Business?* International Space University: Kluwer Academic Publishers, 2002.

[14] H.Bonyan, *Systems Engineering Approach Toward the Problem of Required Level of In-orbit Autonomous Operation of a LEO Microsatellite Mission*. Quincy MA , USA: International Conference on Complex Systems (ICCS), 2007.

[15] Kevin Bullis, *Electric Propulsion Gives Small Satellites a Boost*. http://www.technologyreview.com/news/535561/electric-propulsion-gives-small-satellites-a-boost/:accessed on 25/3/2015, March 2015.

[16] Luca D'Agostino, *Rocket Propulsion lecture notes*. University of Pisa, 2013-2014.

[17] SITAEL S.p.A, *SATSLab Spacecraft Attitude, Trajectory and Subsystems Laboratory*. Mission analysis, Product Sheet, 2015.

[18] A. Ruggiero, P.Pergola, and S.Marcuccio, *Joint Trajectory and Energy Management Simulation of Low Thrust Missions*. The 32nd International Electric Propulsion Conference,Wiesbaden, Germany, September 2011.

[19] S. T. King, Mitchell L. R., and Craig A. Kluever, *Small Satellite LEO Maneuvers with Low-Power Electric Propulsion*. 44th AIAA/ASME/SAE/ASEE Joint Propulsion Conference and Exhibit: American Institute of Aeronautics and Astronautics.

[20] B. Chamot, *Mission and System Architecture Design for Active Removal of Rocket Bodies in Low Earth Orbit*. EPFL Microengineering Department,Massachusetts Institute of Technology, 2012.

[21] J. M. Andringa and Daniel E. Hastings, *A Systems Study on How to Dispose of Fleets of Small Satellites : Master thesis*. MIT Space Systems Laboratory, February 2001.

[22] D. A. Vallado and James Wertz, *Fundamentals of Astrodynamics and Applications. 4th Ed*. Space Technology Library, 2013.

[23] *Space Transportation Costs: Trends in Price Per Pound to Orbit 1990-2000*. Futron Corporation, September 2002.

[24] accessed on :23/9/15, "http://www.kosmotras.ru/en/launch18/,"

[25] Dan M. Goebel and Ira Katz, *Fundamentals of Electric Propulsion:Ion and Hall Thrusters*. Jet Propulsion Laboratory California Institute of Technology: WILEY, 2008.

[26] T. Misuri, Riccardo Albertoni, Cosimo Ducci, Mariano Andrenucci, Barak Waldvogel, Jacob Herscovitz, Adler Shimshon, and Davina Di Cara, *MEPS Programme - Development of a Low Power, Low Cost HET for Small Satellites*. Space Propulsion 2014, Cologne,Germany, 2014.

[27] B. Howley, *AA236: Overview of Spacecraft Attitude Determination and Control*. Lockheed Martin Space Systems Company.

[28] H. Alemi Ardakani and T. J. Bridges, *Review of the 3-2-1 Euler Angles:a yaw-pitch-roll sequence*. 2010.

[29] W. Hu, *Fundamental Spacecraft Dynamics and Control*. Wiley, 2015.

[30] J. Diebel, *Representing Attitude: Euler Angles,Unit Quaternions, and Rotation Vectors*. Stanford University, 2006.

[31] V. Chobotov, *Orbital Mechanics, 3rd edition*. AIAA, 1991.

[32] J. A. Kechichian, *The Reformulation of Edelbaum's Low Thrust Transfer Problem Using Optimal Control Theory*. American Institute of Aeronautics and Astronautics (Vol. 20, No. 5).

[33] T. Edelbaum, *Propulsion Requirements for Controllable Satellites*. ARS Journal,Vol 31, 1961.

[34] J. R. Wertz, . *Mission Geometry:Orbit and Constellation Design and Management*. El Segundo, California: Microcosm Press, 2001.

[35] G. Mengali and Alessandro A. Quarta, *Fondamenti di Meccanica del Volo Spaziale*. Pisa University Press, 2006.

[36] H. Schaub and J. L. Junkins, *Analytical Mechanics of Space Systems, AIAA*. Reston,VA: Education Series, 2003.

[37] J. R. Wertz, John T. Collins, Simon Dawson, Hans J. Koenigsmann, and Curtis W. Potterveld, *Autonomous Constellation Maintenance*. Torrance,CA: Microcosm,Inc., 1997.

[38] S. Marcuccio, Stefano Giannelli, and Mariano Andrenucci, *Attitude and Orbit Control of Small Satellites and Constellations with FEEP Thrusters*.

[39] J. Wertz, D.F.Everett, and J. Puschell, *Space Mission Engineering:The New SMAD*. Space Technology Library: Microcosm Press, 2011.

[40] D. A. Vallado and David Finkleman, *A Critical Assessment of Satellite Drag and Atmospheric Density Modeling*. Center for Space Standards and Innovation, Colorado Springs, Colorado: American Institute of Aeronautics and Astronautics.

[41] J. Picone, A. Hedin, D. P. Drob, and A. C. Aikin, *NRLMSISE-00 Empirical Model of the Atmosphere: Statistical comparisons and scientific issues*. Journal of Geophysical Research: Space Physics, 2002.

[42] J. L. Young, *Determination of Atmospheric Density in Low-Earth Orbit Using GPS Data (Trident scholar project rept. no. 287)*. 2001.

[43] OHB-System AG, HTG, and DLR, *End-of-Life De-orbit Strategies Executive Summary*. 2002.

[44] H. Klinkrad, P. Beltrami, S. Hauptmann, C. Martin, H. Sdunnus, H. Stokes, R. Walker, and J. Wilkinson, *The ESA Space Debris Mitigation Handbook*. 2002.

[45] M. Baldwin, *Autonomous Optimal Deorbit Guidance*. Iowa State University: Graduate Theses and Dissertations, Paper 11218, 2010.

[46] A. Parihar, *Preliminary Assessment of Power Subsystem and Communication Subsystem for D3SAT mission:Master thesis*. University of Pisa, 2015.

[47] Y. Chan, Byung-Hoon Lee, Jung-Won Choi, Mi-Yeon Yun, and Seok-Jin Kang, *Rapid Initial Detumbling Strategy for Micro/Nanosatellites Using a Pitch Bias Momentum System*. Transactions of The Japan Society for Aeronautical and Space Sciences, May 2007.

[48] W. H. Steyn, Yoshikazu Hashida, and Vaios Lappas, *An Attitude Control System and Commissioning Results of the SNAP-1 Nanosatellite*.

[49] F. Deleflie, P. Exertier, and G. Metris, *Near -Circular Orbits : A SemiI-Analytical Method Which Permits to Calculate Orbits Over Several Years*. CERGA.

[50] T. Bak, *Spacecraft Attitude Determination: A Magnetometer Approach*. Aalborg Universitetsforlag, 1999.

[51] J. R. Dutia, *Magnetic Attitude Control of Microsatellites in Geocentric Orbits: Master Thesis*. University of Toronto, Institute for Aerospace Studies: Faculty of Applied Science and Engineering, 2013.

[52] accessed on:14/10/15, "http://www.ngdc.noaa.gov/iaga/vmod/igrf.html,"

[53] SSTL, *Magnetometer Datasheet*. UK: http://www.sstl.co.uk/Products/Subsystems /Actuators-Sensors/Sensors : accessed on 25/8/15, 2015.

[54] O. Montenbruck, Markus Markgraf, Miquel Garcia Fernandez, and Achim Helm, *GPS for Microsatellites: Status and Perspectives*. Berlin: 6th IAA Symposium on Small Satellites for Earth Observation, 2007.

[55] P. B. W. and Spilker J.J., *Global Positioning System : Theory and Applications, vols. 1 and 2*. Washington DC,U.S.A: , American Institute of Aeronautics, 1996.

[56] K. W.J., *GPS for precise time and interval measurements in Global Positioning System: Theory and Applications, vol. 1*. Washington DC: American Institute of Aeronautics and Astronautics, 1996.

[57] P. Gustavsson, "Development of a Matlab-based GPS constellation Simulation for Navigation Algorithm Developments," 2005.

[58] N. Zhou, *Onboard Orbit Determination using GPS Measurements for Low Earth Orbit Satellites*. 2004.

[59] SSTL, *Space GPS Receiver - SGR-05P (Navigation and Timing) datasheet*. UK: http://www.sstl.co.uk/Products/Subsystems/Navigation/SGR-05P-Space-GPS-Receiver:accessed on1/9/15, 2015.

[60] R. Langel, *The Main Geomagnetic Field in Geomagnetism,Volume 1*. Academic Press:New York, 1987.

[61] Sensonor, *STIM300 Inertial Measurement Unit datasheet*. Norway: http://www.sensonor.com/gyro-products/inertial-measurement-units/stim300.aspx :accessed on 4/9/15.

[62] MicroStrain, *3DM-GX1:Gyro Enhanced Orientation Sensor Datasheet*. http://www.microstrain.com/inertial/3DM-GX1 : accessed on 11/9/15.

[63] J. C. Springman, *Satellite Attitude Determination with Low-Cost Sensors,Ph.D thesis*. University of Michigan, 2013.

[64] J. Bentons, *Pyramid Coarse Sun Sensing for NASA SSTI 'CLARK' Safe-Hold Mode*.

[65] AIRBUS Defense and Space, *BASS17 Datasheet*. http://www.space-airbusds.com/en/equipment/bass.htm :accessed on 2/10/15.

[66] J. L. Farrell, J. Stuelpnagel, R. Wessner, J. Velman, and J. Brook, *A Least Squares Estimate of Satellite Attitude (Grace Wahba)*. SIAM review, 2006.

[67] J. Martin Benet, *SwissCube Attitude Determination Algorithm Design and Validation, Masters Project*. École Polytechnique Fédérale de Lausanne, 2007.

[68] M. Isabel Ribeiro, *Kalman and Extended Kalman Filters: Concept, Derivation and Properties*. Institute for systems and Robotics,Instituto Superior Tecnico Portugal, 2004.

[69] D. N. J. du Toit, *Low Earth Orbit Satellite Constellation Control Using Atmospheric Drag*. University of Stellenbosch, Jaunary 1997.

[70] W. C. Stone and Christoph Witzgall, *Evaluation of Aerodynamic Drag and Torque for External Tanks in Low Earth Orbit*. Journal of Research of the National Institute of Standards and Technology,Volume 111, March-April 2006.

[71] NASA Space Vehicle Design Criteria,Guidance and Control, *Spacecraft Aerodynamic Torques*. NASA,SP-8058.

[72] B. Lut Yin Wong, *The Enhancement of Atmospheric Drag Prediction Using Space-Tracking Data for Accurate Debris Surveillance and Collision Warning*. RMIT University, May 2012.

[73] M. M. Moe, Steven D. Wallace, and Kenneth Moe, *Recommended Drag Coefficients for Aeronomic Satellites*. Los Angeles,California: American Geophysical Union.

[74] NASA Space Vehicle Design Criteria,Guidance and Control, *Spacecraft Magnetic Torques*. NASA,SP-8018.

[75] M. Ruiz Delgado, *Radiation Pressure:Modeling the Space Environment*. Universidad Politecnica de Madrid: European Masters in Aeronautics and Space, 2008.

[76] T. Kubo-oka and Arata Sengoku, *Solar radiation pressure model for the relay satellite of SELENE*. Earth Planets and Space 51,: 979-986, 1999.

[77] de Marchi, E., et al. , *Optimal Magnetic Momentum Control for Inertially Pointing Spacecraft*. Spacecraft Guidance, Navigation and Control Systems. Vol. 425, 2000.

[78] Jean-Francois Tregouet and Denis Arzelie and Dimitri Peaucelle and Christelle Pittet and Luca Zaccarian, *Reaction wheels desaturation using magnetorquers and static input allocation*. Control Systems Technology, IEEE Transactions on (Volume:23 , Issue: 2), 2014.

[79] P. Camillo and F. Markley, *Orbit-Averaged Behavior of Magnetic Control Laws for Momentum Unloading*. Journal of Guidance and Control (Vol. 3, No. 6 , pp. 563-568), 1980.

[80] R. McElvain, *Satellite angular momentum removal using the Earth's magnetic field*. Academic Press, 1964.

[81] D. Eagle, *Cowell's Method for Earth Satellites*. The MathWorks Inc., 2013.

[82] *http://it.mathworks.com/matlabcentral/fileexchange/39703-cowell-s-method-for-earth-satellites*.

[83] Astro- und Feinwerktechnik Adlershof GmbH, *Reaction Wheel RW 35 for Nano and Micro Satellites Data sheet*. http://www.astrofein.com/astro-und-feinwerktechnik-adlershof/products/raumfahrt/75/rw-35-eng/:accessed on 28/9/15.

[84] *Improve Your Attitude!Magnetic Torquers for Micro-Satellites*. ZARM Technik AG, 2015.

[85] *Intelligent Solutions to Reduce Space Mission Costs: Magnetic Torquers for Spacecraft Attitude Control*. Bremen Germany: ZARM Technik AG, 2015.

[86] A. H. Ruiter, Christopher Damaren, and James R. Forbes, *Spacecraft Dynamics and Control: An Introduction*. Wiley, 2012.

[87] I. Stroe and D. Dumitriu, *Minisatellite Attitude Guidance Using Reaction Wheels*. 3rd International Workshop on Numerical Modelling in Aerospace Sciences(Volume 7, Issue 2), 2015.

[88] S. Karataş, *LEO Satellites:Dynamic Modelling,Simulations and Some Nonlinear Attitude Control Techniques:Master thesis*. Middle East Technical University, 2006.

[89] J. L.Crassidis and John L. Junkins, *Optimal Estimation of Dynamic Systems, Second Edition*. London: Chapman and Hall/CRC, 2011.

[90] B. Wie, H. Weiss, and A. Arapostathis, *Quarternion Feedback Regulator for Spacecraft Eigenaxis Rotations*. Journal of Guidance, Control and Dynamics, Vol. 12, 1989.

[91] M. Kathleen Quadrino, Prof David Miller, and Prof Kerri Cahoy, *Testing the Attitude Determination and Control of a CubeSat with Hardware-in-the-Loop*. Massachusetts Institute of Technology, 2014.

[92] M. Lovera, *Optimal Magnetic Momentum Control for Inertially Pointing Spacecraft*. European Journal of Control (Vol.7, No 1), 2001.

[93] B. TF and Flashner H., *Adaptive control applied to momentum unloading using the low Earth orbit environment*. J Guidance, Control and Dynamics (Vol. 15, No. 2), 1999.

[94] S. M., *Spacecraft Dynamics and Control*. Cambridge University Press, 1997.

[95] B. P. Arduini C, *Active Magnetic Damping: Attitude Control for Gravity Gradient Stabilised Spacecraft*. Journal of Guidance and Control (Vol. 20, No. 1), 1997.

[96] T. I. Fossen., *Handbook of Marine Craft Hydrodynamics and Motion Control,1st edition*. John Wiley, 2011.

[97] F. Reichel, *Attitude Control System of UWE-3 - Design, Testing and Verification.: Master thesis*. Julius-Maximilians-University Würzburg, October 2012.

[98] A. Pignede, *Detumbling of the NTNU Test Satellite:project thesis*. Norwegian University of Science and Technology, 2014.

[99] A. Pietruszewski and David Spencer, *Prox-1 Attitude Determination and Control*. Georgia Institute of Technology.